

PHYSICAL PROPERTIES OF NANOSTRUCTURES INDUCED BY IRRADIATION IN DIAMOND



Thuto Nelson Makgato

School of Physics

University of the Witwatersrand

Johannesburg, South Africa

A Thesis submitted to the Faculty of Science, University of the
Witwatersrand, Johannesburg, in fulfillment of the requirements for the
degree of Doctor of Philosophy in Physics.

Signed, 10 August 2017 in Johannesburg

Declaration

I declare that this Thesis is my own, unaided work. It is being submitted for the Degree of Doctor of Philosophy at the University of the Witwatersrand, Johannesburg. It has not been submitted before any degree or examination at any other University.

A handwritten signature in black ink, consisting of several overlapping loops and lines, positioned above a horizontal line.

(Signature of candidate)

10th day of AUGUST 2017

in JOHANNESBURG

Abstract

We investigate the interaction of slow highly charged ions (SHCIs) with insulating type-Ib diamond (111) surfaces. Bismuth and Xenon SHCI beams produced using an Electron Beam Ion Trap (EBIT) and an Electron Cyclotron Resonance source (ECR) respectively, are accelerated onto type Ib diamond (111) surfaces with impact velocities up to $\approx 0.4\mu_{Bohr}$. SHCIs with charge states corresponding to potential energies between 4.5 keV and 110 keV are produced for this purpose. Atomic Force Microscopy analysis (AFM) of the diamond surfaces following SHCI impact reveals surface morphological modifications characterized as nanoscale craters (nano-craters). To interpret the results from Tapping Mode AFM analysis of the irradiated diamond surfaces we discuss the interplay between kinetic and potential energy in nanocrater formation using empirical data together with Stopping and Range of Ions in Matter (SRIM) Monte Carlo Simulations.

In the case of irradiation induced magnetic effects in diamond, we investigate the magnetic properties of ultra-pure type-IIa diamond following irradiation with proton beams of $\approx 1-2$ MeV energy. SQUID magnetometry of proton irradiated non-annealed diamond indicates formation of Curie type paramagnetism according to the Curie law. Raman and Photoluminescence spectroscopy measurements show that the primary structural features created by proton irradiation are the centers: GR1, ND1, TR12 and 3H. The Stopping and Range of Ions in Matter (SRIM) Monte Carlo simulations together with

SQUID observations show a strong correlation between vacancy production, proton fluence and the paramagnetic factor. At an average surface vacancy spacing of $\approx 1-1.6$ nm and bulk (peak) vacancy spacing of $\approx 0.3-0.5$ nm Curie paramagnetism is induced by formation of ND1 centres with an effective magnetic moment $\mu_{eff} \sim (0.1-0.2)\mu_B$. Post annealing SQUID analysis of proton irradiated diamond shows formation temperature independent magnetism with magnetic moment $\approx 6-7 \mu\text{emu}$ superimposed to Curie-type paramagnetism.

The response of ultra-pure type-IIa single crystal CVD diamond following 2.2 MeV proton micro-irradiation is further investigated using Atomic Force, Magnetic Force and Electrostatic Force Microscopy (AFM, MFM and EFM) under ambient conditions. Analysis of the phase shift signals using probe polarization dependent magnetization measurements and comparison of the MFM and EFM signals at zero electrical bias, show that measured force gradients originate from a radiation induced magnetic response in the micro-irradiated regions in diamond.

Dedication

To my family

Acknowledgements

I wish to thank the following people for their continued support and guidance without which, progress and success in this work would not have been possible:

- **My Project Supervisor: Prof. Elias Sideras-Haddad**

Your leadership, guidance and support have been invaluable in my journey through this research, I'm truly grateful.

- **My family**

Your support and presence has kept me strong through difficult times, ke leboga lerato, thekgo le dithapelo tša lena.

- **School of Physics, University of the Witwatersrand**

For the financial support you have granted us in support of this project.

- **Madrid Collaborators**

To Sandro, Miguel and Mar, your guidance and assistance with the experiments and analysis at CMAM and CSIC has been valuable, thank you.

- **Max-Planck Institute for Nuclear Physics**

To José, thank you for your efforts in facilitating and assisting with the

EBIT experiments in Heidelberg.

- **TU-Wien Group**

Robber Ritter, for your assistance through those long demanding experiments with the EBIT, thank you for the support.

- **iThemba LABS Group**

Dr. Madhuku, Kamela, Tsepo, Carlos at Faure, thank you for assistance in the irradiation facilities and sample preparation lab at iThemba LABS.

- **Dr. Sanjiv Shrivastava**

For the AFM work we embarked on under your guidance, we have come a long way since then, thank you.

- **Dr. Rudolf Erasmus**

Thank you for your unwavering commitment with the Raman and PL data.

Contents

Declaration	i
Abstract	iii
Dedication	iv
Acknowledgements	vi
1 Introduction	19
1.1 Literature Background	19
1.2 Outline of Thesis	23
2 Diamond	27
2.1 Structure and Properties	28
2.2 Classification of Diamond	29
2.3 Defects in Diamond	33
2.3.1 Vacancy Defects	33
2.3.2 Nitrogen-Vacancy Defects	36
2.3.3 Hydrogen Mediated Defects	40
3 Highly Charged Ions	44
3.1 Overview	44
3.2 Fundamental Aspects	45
3.2.1 Interactions of HCIs with matter	50

3.3	Interactions of HCIs with Matter	56
3.3.1	The Coulomb Explosion Model	56
3.3.2	The Inelastic Thermal Spike Model	60
3.3.3	The Analytical Thermal Spike Model	63
3.3.4	The Defect Mediated Desorption Model	68
4	Magnetism and Magnetic Materials	71
4.1	Atomic Magnetism	71
4.2	Magnetic Interactions	75
4.2.1	Magnetic Dipole Interaction	75
4.2.2	Exchange Interactions	76
4.3	Classification of Magnetic Materials	81
4.4	Magnetism in Carbon Systems	85
5	Experimental Techniques	101
5.1	Sample Preparation	102
5.2	Ion Sources	105
5.2.1	Electron Beam Ion Trap (EBIT)	105
5.2.2	Electron Cyclotron Resonance Ion Source (ECRIS)	108
5.2.3	Duoplasmatron Ion Source	110
5.2.4	Source of Negative Ions by Cesium Sputtering	111
5.3	Particle Accelerator Techniques	113
5.4	Irradiation Parameters	129
5.5	Scanning Probe Microscopy Techniques	132
5.5.1	Atomic Force Microscopy (AFM)	132
5.5.2	Magnetic Force Microscopy (MFM)	135
5.5.3	Electric Force Microscopy (EFM)	138
5.6	Optical Spectroscopy	139
5.6.1	Raman Scattering Theory	139
5.6.2	Photoluminescence Spectroscopy	143

5.7	The Superconducting Quantum Interference Device (SQUID) . .	145
6	Results and Discussions	149
6.1	SHCI Impact on Diamond Surfaces	149
6.1.1	Experimental Results	150
6.2	Proton Induced Evolution of Magnetic and Optical Properties .	158
6.2.1	Monte Carlo Simulation	158
6.2.2	Macro-irradiation Investigations	161
6.2.3	Micro-irradiation Investigations	170
7	Conclusions and Outlook	183
A	Published Manuscripts	188
	References	189

List of Figures

2.1	<i>The Crystal structure of cubic diamond showing the tetrahedral bonding arrangement, the lattice spacing, a, and the nearest neighbour distance, d [41].</i>	29
2.2	<i>Calculated electron density contours of the sp^3 hybrid orbital [42].</i>	29
2.3	<i>Schematic presentation of diamond classification based on nitrogen concentration and distribution.</i>	32
2.4	<i>Schematic presentation of the H3 centre in diamond showing substitutional nitrogen defects (N) as well as the single vacancy defect (V^0) [45].</i>	37
2.5	<i>Schematic presentation of the NV centre energy level system in diamond. The grey line corresponds to the $m_s \pm 1$ excited energy sub-levels [60]. MW represents micro-wave excitation.</i>	38
2.6	<i>Optimized structure of the N-H-N defect consisting of the hydrogen defect located between two adjacent A centres with $d=2.20 \text{ \AA}$, $\alpha=117.0^\circ$ and $\beta=100.0^\circ$. Reproduced from Miyazaki et al. [87].</i>	42
3.1	<i>Top image: Electron binding energy (ionization potential) of xenon HClIs. Bottom image: Potential energy of xenon HClIs. The data is calculated using MCDF methods (triangles) employed in the Grasp code and SCF methods (circles) used in the spherical shell model.</i>	48

3.2	<i>Top image: Electron binding energy (ionization potential) of bismuth HClIs. Bottom image: Potential energy of bismuth HClIs. The data is calculated using MCDF methods (triangles) employed in the Grasp code and SCF methods (circles) used in the spherical shell model.</i>	49
3.3	<i>Schematic summary of SHCI interaction with a surface. The terms $\Delta E_{q,im}$ and R_c represent the image charge energy gain and the critical distance, respectively. Ultimate neutralization of the hollow atom can take place several monolayers beneath the surface.</i>	53
3.4	<i>Electron emission yields as a function of ion charge state, q following impact of xenon SHCI on type IIa diamond (square symbols), type IIb diamond (circles) and a reference Aluminum target (triangles) [110].</i>	55
3.5	<i>Non-contact mode AFM topography image of nano-scale defects on HOPG bombarded with Sb^{18+} SHClIs [111].</i>	56
3.6	<i>Electronic transitions between surface and projectile HCI leading to formation of holes (via resonant neutralization) as well as electron-hole pairs (via Auger neutralization [103]</i>	69
4.1	<i>Graphical representation of the function $F(x)$ defined in Eq.4.31 using $x=2k_{Fr}$. Positive values lead to a ferromagnetic coupling whereas negative values lead to an anti-ferromagnetic arrangement [157].</i>	80
4.2	<i>Temperature dependence of the magnetic susceptibility χ and inverse magnetic susceptibility χ^{-1} in the case of (a) diamagnetism and Pauli paramagnetism, (b) Langevin paramagnetism, (c) ferromagnetism, antiferromagnetism and ferrimagnetism with T^* being the critical temperature and θ the paramagnetic Curie temperature</i>	84
4.3	<i>(a) Structure, charge density ($e/\text{\AA}^3$), and (b) spin density ($e/\text{\AA}^3$) of the graphite vacancy. Density plots are slices in the graphene plane [37].</i>	87

- 4.4 Net magnetic moment following irradiation of HOPG (on Si substrate) at a constant applied magnetic field of 1 T using a broad proton beam (total accumulated charge 450 μC at 100 nA) of 2 MeV energy. (a) Net magnetic moment vs temperature at 1 T. The continuous line is the function $3 \times 10^{-5}[\text{emu K}]/T + 3 \times 10^{-6}[\text{emu}]$. (b) Hysteresis loop; net magnetic moment of the irradiated HOPG sample as a function of the applied magnetic field cycled between [-1, 1] T at 5 K and 300 K. The inset shows the hysteresis loop in a narrow range [-0.15, 0.15] T for clarity [26]. 91
- 4.5 Net magnetic moment of HOPG following two sets of irradiations using a proton micro beam of 2 μm diameter and energy 2.25 MeV at 100 K and an applied magnetic field of 1T. First with 10^4 spots with a total charge 11.6 μC at 700 pA and the second adding similar 2×10^4 spots with total charge 34.8 μC at 700 pA. (a) M vsT curves showing the net magnetic moment after 10^4 and 2×10^4 irradiated spots. The continuous lines are fits to the function $m_0+m_1 \exp(-T/T_0)$ with parameters $m_0=2.2(5.6) \times 10^{-6}$ emu, $m_1=1.9(5.07) \times 10^{-6}$ emu and $T_0=116(140)$ K for the first(second) irradiated sample. (b) The hysteresis loops corresponding to data the in (a). The inset shows the hysteresis loops in a broader field range for the first (dotted line) and second irradiation (continuous line) [26]. 94
- 4.6 (a) Magnetic force gradient images (20×20) μm^2 of a spot and its surroundings irradiated with 0.115 nC μm^{-2} (current I=171 pA). The images were taken, from top to bottom, before field application, after applying a field of ~ 0.1 T in the +z direction (normal to the surface), and in the -z direction. The tip-sample distance was 50 nm; (b) the corresponding height (top) and phase shift (bottom) obtained at the linescans (black line (a)) [17]. 95

4.7	(a) Structure and (b) spin density ($\mu_B/\text{\AA}^2$) of a vacancy surrounded by two hydrogen atoms in graphite (graphene). (c) Structure and (d) spin density ($\mu_B/\text{\AA}^2$) of a C-H group adsorbed between two layers of graphene [37].	97
5.1	Target preparation and experimental end station of the EBIT at Max Planck Institute in Heidelberg	103
5.2	Target chamber with golden quartz sample holders at the 5 MV Tandem Accelerator in CMAM.	104
5.3	Diagram showing the Heidelberg EBIT used for the production of Bismuth HCIs used in the present study.	107
5.4	Schematic diagram showing the ECR 4 Lead Source used for ion production including HCIs at GANIL in France.	109
5.5	Top: Schematic diagram of a duoplasmatron ion source [176].	111
5.6	Top: Source of Negative Ions by Cesium Sputtering (SNICP) at iThemba LABS.	112
5.7	Top: Schematic diagram of the pelletron and ladderton high voltage generator [182]. Bottom: Pelletron charging system at iThemba LABS in Gauteng during a maintenance operation.	115
5.8	The 6 MV Tandem accelerator at iThemba LABS in Gauteng, South Africa.	116
5.9	5 MV Tandem Accelerator (left) with schematic diagram showing ion/particle beam lines (right) at CMAM.	117
5.10	Schematic diagram for determination of the ion mass resolution of analyzing section magnets [176]	118

5.11	<i>Scheme of the basic sector magnet for mass analyzing. (a). The higher masses are less deflected and the lower masses more. Co-linearity (Barber's rule) of sector magnet object (source), image, and magnet apex (b). Due to the extended magnetic field the pole faces can be shifted relative to the dotted line by a distance in the order of gap width of the exit slit [176].</i>	119
5.12	<i>Analyzing 90° sector magnet at iThemba LABS in Gauteng.</i>	120
5.13	<i>Bismuth charge to mass selection through the 90° analyzing magnet at Heidelberg EBIT.</i>	121
5.14	<i>Top: Schematic diagram showing the magnetic and electrostatic quadrupole [176], Bottom: Nuclear microprobe at iThemba LABS Faure.</i>	122
5.15	<i>Schematic diagram showing the PIXE experiment for a proton beam incident on a diamond sample of thickness d.</i>	124
5.16	<i>PIXE spectrum acquired during irradiation of type-IIa diamond using a 2.2 MeV proton micro beam at iThemba LABS Faure.</i>	126
5.17	<i>RBS spectrum acquired during irradiation of type-IIa diamond using a 2.2 MeV proton beam at iThemba LABS Faure.</i>	128
5.18	<i>Qualitative representation of the van der Waals interaction force dependence on the tip-sample spacing, x(nm).</i>	133
5.19	<i>Veeco Dimension 3100 AFM with Nanoscope IIIa Controller.</i>	135
5.20	<i>Schematic diagram representing the basic MFM principle of operation.</i>	136
5.21	<i>MFM image of magnetic domains on a standard computer hard disk drive platter with corresponding line profiles showing polarization dependence of the domains.</i>	137
5.22	<i>Energy level diagram showing Rayleigh (a), Stokes Raman (b) and anti-Stokes Raman scattering (c).</i>	141
5.23	<i>Simplified energy level scheme showing excitation of vibronic centres.</i>	144

5.24	<i>Schematic diagram of a low-T_c dc SQUID with integrated input coil [195].</i>	147
6.1	<i>TM-AFM topography image showing the pristine atomically flat diamond (111) surface together with a line profile extracted from the image data represented by the dotted lines.</i>	151
6.2	<i>Examples of TM-AFM topography images showing diamond (111) surfaces after irradiation with Bi^{59+} and Xe^{31+} SHCIs.</i>	152
6.3	<i>Topography line profiles extracted from the Bi^{59+} topography image in Fig 6.2 showing crater-like morphology of the induced nanoscale defects.</i>	154
6.4	<i>Potential energy dependence of Bismuth and Xenon SHCI induced nano-crater diameter in insulating type Ib diamond (111) crystal planes.</i>	155
6.5	<i>SRIM Monte Carlo simulations showing the stopping of Xenon and Bismuth ions in diamond as a function of the ion kinetic energy.</i>	156
6.6	<i>SRIM ion range estimates for 2.2 MeV protons in diamond.</i>	159
6.7	<i>SRIM Collision Events for 2.2 MeV protons in diamond.</i>	160
6.8	<i>Linear diamagnetic background of pristine diamond samples A and B acquired at 4.2 K and 300 K.</i>	162
6.9	<i>Magnetic moments of diamond samples A and B acquired at different irradiation and annealing stages as function of the applied field at 300 K.</i>	163
6.10	<i>Magnetic moments of diamond samples A and B acquired at different irradiation and annealing stages (see Table.1) as function of the applied magnetic field at 4.2 K</i>	164

6.11	<i>Net magnetic moment of diamond samples A and B at different irradiation (and annealing) stages acquired as a function of temperature at 2 kOe. The inset showing the net magnetic moment as a function of the inverse temperature at 2 kOe indicates that at all irradiation (and annealing) stages, the system obeys the Curie law and exhibits Curie-type paramagnetism</i>	165
6.12	<i>Raman spectroscopy of diamond sample A acquired at room temperature showing pristine, A: I4 and A: I4+Anneal spectra.</i>	168
6.13	<i>Depth resolved photoluminescence spectroscopy of diamond sample A acquired at room temperature following irradiation stage A: I4. . .</i>	169
6.14	<i>Optical images of micro-irradiations on type IIa diamond (100) surfaces by 2.2 MeV Proton micro-beams.</i>	171
6.15	<i>Example of a Tapping Mode AFM topography image acquired over region-A of Sample-1 together with a line profile extracted across a region represented by the dashed lines.</i>	172
6.16	<i>Example of a Tapping Mode AFM topography image acquired over region-E of Sample-2 together with a line profile extracted across a region represented by the dashed lines. The dotted lines represent the irradiated region.</i>	172
6.17	<i>Example of a MFM Phase image (deg.) of region-A sample-1 acquired 50 nm above the diamond (100) surface together with the corresponding line profile (deg.) extracted from a region represented by the dashed lines.</i>	173
6.18	<i>Example of a MFM Phase image (deg.) of region-E sample-2 acquired 50 nm above the diamond (100) surface together with the corresponding line profile (deg.) extracted from a region represented by the dashed lines.</i>	174

- 6.19 *Phase shift (deg.) versus Position (μm) of the magnetic probe over region-A Sample-1 at several lift scan heights (nm) with the probe polarized in the '+1' polarization direction. 175*
- 6.20 *Phase shift (deg.) versus Position (μm) of the magnetic probe over region-A of sample-1 under different probe magnetization directions. 176*
- 6.21 *Example of an EFM image acquired over region-A of Sample-1 using a SCM-PIT type probe electrically biased at 4V together with the corresponding line profile (deg.) extracted across the region represented by the dashed lines. 177*
- 6.22 *Example of an EFM image acquired over region-A of Sample-1 using a SCM-PIT type probe under zero electrical bias (0V) together with the corresponding line profile (deg.) extracted across the region indicated by the dashed lines. 179*
- 6.23 *Electrostatic response measured as a phase shift (deg.) from the piezo drive at 50 nm above region-A of Sample 1 using MESP-HM (square symbols) and SCM-PIT (circular symbols) probes types as a function of the applied electrical bias voltage (V). The insert shows an example of EFM profiles acquired using SCM-PIT probes illustrating the deviation from normal quadratic behaviour at higher bias voltages. 181*

List of Tables

2.1	<i>Selected Physical Properties of Diamond and Silicon at room temperature (300 K)</i>	30
2.2	<i>Summary of common nitrogen and vacancy related defects centres in diamond.</i>	39
5.1	<i>Table showing Bismuth Highly Charged Ions produced using the Heidelberg EBIT for surface nanostructuring experiments.</i>	129
5.2	<i>Table showing Xenon Highly Charged Ions produced using the GANIL ECR for surface nanostructuring experiments.</i>	130
5.3	<i>Summary of irradiation parameters used at the CMAM tandem for proton macro irradiation of type-IIa diamond</i>	130
5.4	<i>Summary of irradiation parameters used at iThemba LABS for proton micro irradiation of type-IIa diamond</i>	131
6.1	<i>SRIM based calculation of irradiation parameters, where P, M and S represents the vacancies/ion-nm at the peak, middle and ‘surface’ of the calculated SRIM vacancy distribution</i>	160
6.2	<i>Irradiation parameters deduced from laboratory and SRIM-based estimates.</i>	161

Chapter 1

Introduction

1.1 Literature Background

From its first discovery to the first systematic synthesis, diamond has intrigued scientists for a plethora of reasons. Diamond is a material with extreme physical properties including best thermal conductor, wide band gap semiconductor, widest range of optical transition frequencies, radiation hardness and high charge carrier mobility. Some applications of diamond-based materials include radiation and particle detectors, optical windows and solid state electronic devices including recently engineered diamond based spintronic devices [1]. By tailoring and promoting such unique properties of diamond, the modification of diamond for specialised uses can be successfully achieved. The successful doping and manufacturing of the first man made p-type semiconducting diamond was based on ion beam modification techniques [2].

Conventional doping mechanisms have been largely based on exploiting the kinetic energy related properties of accelerated ions using particle accelerators such Van der Graaf generators and Tandem accelerators. However, advances in ion source techniques have opened a window for experimental physics using exotic ions in highly charged states which are ordinarily found in outer

space. Recent studies have shown that interaction of *slow* highly charged ions (SHCIs) with material surfaces results in a range of inelastic physical phenomena including *hollow atom* formation, x-ray emission, sputtering of surface atoms, molecules and clusters into vacuum and eventually projectile neutralization. Upon interaction with a target material, the impinging SHCI imparts energy of power density $\sim 10^{14} \text{ Wcm}^{-2}$ to the electronic and atomic systems of the surface in a nanoscale region within extremely short time scales of a few femtoseconds [3].

In this sense, the interaction is analogous to femtosecond pulsed lasers. However, the interaction of SHCIs with surfaces are of higher spatial localization rather than femtosecond lasers where the diffraction limit to the localization depends on the wavelength of the laser-light and is usually $\sim 100 \text{ nm}$ compared to $\sim 10 \text{ nm}$ for SHCIs [4]. In femtosecond laser excitations the dissipation of energy by the surface, usually results in lattice heating via electron-phonon coupling within picosecond to nanosecond timescales within which electrons can travel relatively large distances and in this manner enlarge the affected region. In contrast, during SHCI relaxation over a few femtoseconds, hot electrons can leave the initially excited volume before they thermalize and transfer excess energy to the lattice.

This rapid *cooling* allows femtosecond non-thermal phase transitions to *freeze* into metastable geometric structures rather than being followed by thermal melting [5]. Numerous studies involving the interaction of SHCIs with metals, semiconductors and insulators have shown that SHCIs can be useful for technological applications such as surface nanostructuring [4] or soft cleaning of materials due to this high spatial and temporal localization of radiation damage induced on the respective target [6, 7]. SHCIs are distinguished from neutral and singly charged ions by additional interaction mechanisms with surfaces. Their interaction is influenced primarily by their large potential energy

which is equivalent to the sum of the ionization potentials and increases rapidly with respect to the SHCI charge state.

In addition to the surface nanostructuring prospects in diamond, the modification of diamond physical properties (in particular magnetic and optical properties) for novel applications as well as for fundamental research remains invaluable. The realization of room temperature magnetic ordering in carbon materials such as diamond, which consist purely of *sp* molecular orbitals, promises leaps in science and could play a pivotal role in emerging technologies. However, in contrast to *d* and *f* electron materials from which standard magnetic devices are produced, magnetic ordering in these materials hardly occurs naturally and despite numerous studies carried out to date, their fabrication by laboratory methods is not entirely understood and remains a field of intensive research.

Earlier investigations on polymerized fullerenes [8, 9] inspired more recent investigations [10–17] that indicate the presence of magnetically ordered states in purely *sp* electron based materials at room temperature. Of all *sp*-electron based materials, carbon materials are highly sought after due to the prospect of low cost fabrication of ultra-light weight, stable, durable and bio-compatible devices. In addition, carbon allotropes, such as diamond feature a substantially low spin-orbit coupling permitting long spin coherence times at room temperature (up to \sim ms for diamond [18]), an imperative for ultra-fast resonant spin manipulation.

Diamond exhibits a wide band gap (\approx 5.5 eV) which allows localized spins to be probed using microwave and optical frequencies for read-write applications of single photon sources [1]. For example, Dutt et al. [19] demonstrated that the ^{13}C nucleus can be used as a quantum register by coupling to individual electron spins associated with the NV colour centres which can be coherently manipulated using optical and microwave frequencies. These properties among

several others, demonstrate the suitability of diamond as a host material for fabricating scalable qubits as building blocks for quantum computing [20, 21]. Since pure insulating diamond can be efficiently doped into a semiconducting state, the ability to induce magnetic ordering in diamond could present the opportunity to create a controllable localized magnetic environment for electron and nuclear spins associated with the NV colour centres to achieve practical spintronics and advanced quantum information devices.

To achieve these specialized applications material properties have to be tailored by modifying their physical properties. Ion implantation techniques have been instrumental in solid state material modifications e.g. in the electronic doping of semiconducting materials [2, 22, 23] as it offers control in the introduction of point defects by means of defect concentration and implantation range. Using known simulation packages such as the Stopping and Range of Ions in Matter (SRIM) [24], estimates of radiation damage by vacancy production can be provided using readily available inputs such as ion energy, ion species, material composition and thickness. In this way, the inter-vacancy spacing can be effectively controlled which is reported to be a critical parameter in triggering various forms of magnetism e.g. paramagnetism [25] and ferro (ferri) magnetism [26–28] in carbon systems. In addition X-ray circular magnetic dichroism (XMCD) studies have shown that magnetic ordering in proton micro-irradiated HOPG films is related to spin correlation in the π -electronic systems and is sensitive to various experimental parameters such as the ion fluence and charge density [29].

The observed low signal strength of magnetic signatures characteristic of irradiated carbon systems has often created much skepticism in the scientific community. Sepioni et al. [30] showed that agglomeration of ferromagnetic impurities in typical HOPG samples can trigger ferromagnetic ordering of several μ emu in magnitude, comparable to signals observed from various irradiated

samples [10, 17, 31]. However, since background measurements using SQUID prior irradiation are routinely carried out and subtracted from results, in addition to other *in-situ* quantitative techniques such as Particle Induced X-ray Emission (PIXE) and Rutherford Backscattering Spectroscopy (RBS), it is unlikely that these observations are attributed to magnetic impurities, instead, it is the effects of irradiation that are quantified with $< \mu\text{emu}$ sensitivity [31].

Nonetheless, the origin of irradiation induced magnetic ordering is still a subject of extensive investigation. Various structures attributed to the origin of organic-carbon based magnetism include; carbon interstitials [32], zigzag edges [33, 34], negative Gaussian curvature [14] and vacancies [28, 35, 36]. Using spin polarized DFT studies Zhang et al. [28] showed that when a single vacancy is introduced into the diamond lattice, the structure undergoes a Jahn-Teller distortion resulting in a stable magnetic moment of $2 \mu_B$ at room temperature, compared to $1.4 \mu_B$ in the case of graphene [37]. The existence of various impurities such as N in close proximity to a single vacancy in diamond can result in a higher magnetic moment at room temperature. Nonetheless, apart from irradiation experiments of nanodiamonds using nitrogen beams [38], few reports of irradiation induced magnetism studies in diamond systems are reported in literature.

1.2 Outline of Thesis

The scientific work addressed in this thesis can be divided into three sections as follows:

- **Interaction between diamond and Highly Charged Ions (HCIs):**

In this section we focus on the nanoscale interactions between HCIs with type Ib diamond. We consider both effects of potential and kinetic energy of HCIs leading to nanoscale surface modification of diamond. Surface

morphological modifications are analyzed using Atomic Force Microscopy (AFM) Techniques. In the analysis and interpretation of nanoscale structures we employ both empirical observations as well as Monte Carlo Simulations of the kinetic energy effects in diamond.

- **Evolution of Magnetic and Optical Properties of Diamond by Proton Macro Irradiation:**

This section focuses primarily on the magnetic properties of ultra-pure type IIa-diamond and the evolution thereof induced by energetic proton *macro*-beam irradiation. Characterization of magnetic properties is carried out using the Superconducting Quantum Interference Device (SQUID). In addition to assessment of the evolution of magnetic properties, we also investigate the corresponding changes in the optical properties of diamond by means of Raman and Photoluminescence spectroscopy spanning the ultra-violet (UV) to near-infra red (NIR) frequencies. Empirical data is analyzed in conjunction with SRIM Monte Carlo simulation to investigate the magnetic effects of proton macro-irradiation in diamond.

- **Scanning Probe Microscopy analysis of proton micro-irradiated diamond:**

In the last section of this work we focus on the irradiation of ultra-pure type IIa diamonds using energetic proton *micro*-beams. Analysis of the micro irradiated diamonds is carried out using SPM techniques, *viz.*, AFM, Magnetic Force Microscopy (MFM) and Electric Force Microscopy (EFM).

Overview of the thesis chapters:

- **Chapter 1: Introduction:**

As an introduction, this chapter provides a historical context of the liter-

ature relevant to the current study. An outline of the thesis is presented together with an overview of each chapter of the thesis.

- **Chapter 2: Diamond:**

In this section, the structure, properties and various features of diamond relevant to the present study are presented. These include, vacancy defects, colour centres, physical properties and effect of impurities

- **Chapter 3: Highly Charged Ions:**

In this chapter, HCIs are introduced. Properties of HCIs and their interaction with matter is discussed. The basis of hollow atom formation is described and potential energy of HCI species used in the present study is calculated. The different models proposed in literature for the governing interaction mechanism such as the coulomb explosion model and the inelastic thermal spike model are discussed.

- **Chapter 4: Magnetism and Magnetic Materials:**

In this chapter we discuss the theory of magnetism, magnetic interactions and classification of magnetic materials. We pay particular focus to various theoretical and experimental of reports magnetism in carbon.

- **Chapter 5: Experimental Details:**

In this section we discuss all the relevant experimental details used in our investigations.

- **Chapter 6: Results and Discussions:**

In this section, results from our investigations are presented and discussed.

- **Chapter 7: Conclusions and Outlook:**

In this section we present the outcomes of investigations carried out in

this thesis. In view of the thesis conclusions, future perspectives are also proposed.

Chapter 2

Diamond

Dating as far back as 1866, the year that marks the discovery of diamonds in Kimberly, South Africa [39], the global popularity and quest for diamonds has been attributed to its extraordinary qualities as a durable gem stone. The characteristic brilliance of diamond gemstones is due to high its dispersive power (which is responsible for the change in colour in the reflected light) as well as multiple internal reflections of light from different facets owing to its high reflective index (2.42 at 589 nm) that leads to a low angle $\approx 24^\circ$ of total internal reflection [40]. Nonetheless, it is particularly remarkable that diamond also features some of the most extraordinary physical and chemical properties of all investigated materials across the periodic chart. The macroscopic and microscopic properties of diamond are extraordinary and render diamond a special material "in a class of its own". In this section we discuss, the physical and chemical properties of diamond, common diamond synthesis methods and techniques as well as defects both intrinsic and extrinsic that are relevant to studies of radiation induced nano-scale and micro-scale structuring of diamond in light of emerging applications such as quantum information and spintronics.

2.1 Structure and Properties

Diamond is a crystalline form of carbon ($\approx 99\%^{12}\text{C}$ and $1\%^{13}\text{C}$) in which each carbon atom is covalently bonded by sp^3 hybrid orbitals to four other carbon atoms in a tetrahedral arrangement with an angle of $\approx 109.5^\circ$ between nearest neighbour atoms. The sp^3 bond (or hybrid orbital) is due to hybridization of one s and three p orbitals (Fig. 2.2). Diamond crystals exist primarily in cubic and hexagonal structures with a lattice spacing $a = 3.567 \text{ \AA}$ and nearest neighbour distance $d = 1.554 \text{ \AA}$ [40]. The space lattice of the cubic diamond structure is face centered cubic (fcc) and the primitive basis consists of two spatially identical carbon atoms located at positions $(0,0,0)$ and $(\frac{1}{4}a, \frac{1}{4}a, \frac{1}{4}a)$ associated with each point of the fcc lattice [41].

The cubic structure is more prevalent and belongs to the space group symmetry known as O_h^7 . The cubic diamond structure is shown in Fig. 2.1. The crystal structure as well as the nature of chemical bonds in determine the mechanical strength of any material. Although diamond is the hardest naturally occurring material according to *Mohr's* hardness scale, it is found that the hardness of diamond varies significantly with respect to the crystallographic axis of reference. Diamond crystallizes primarily in an octahedral geometry along $\langle 111 \rangle$ axes or dodecahedra along (110) and very rarely in cubic geometry along $\langle 100 \rangle$ [40]. For these reasons, the mechanical strength of diamond along these axes is greatly reduced and hence diamonds are preferentially cleaved along the $\langle 111 \rangle$ axes. A summary of selected physical properties of diamond are shown in Table 2.1 and are compared with a common competitor material, namely Silicon to highlight some extraordinary properties of diamond.

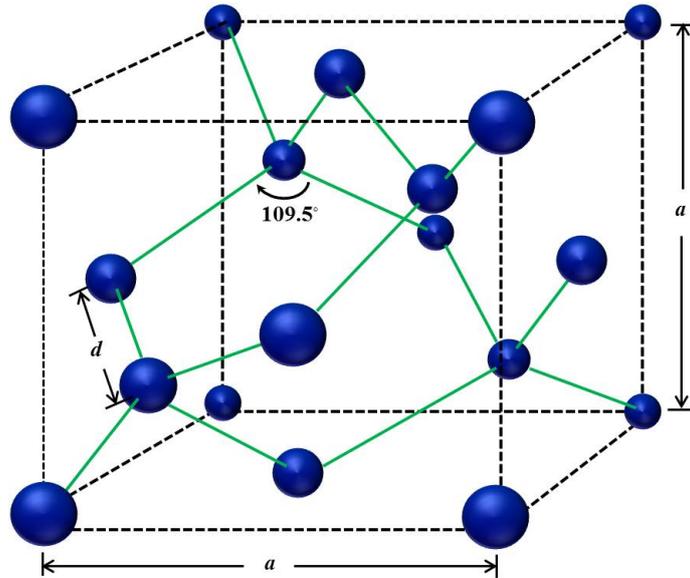


Figure 2.1: The Crystal structure of cubic diamond showing the tetrahedral bonding arrangement, the lattice spacing, a , and the nearest neighbour distance, d [41].

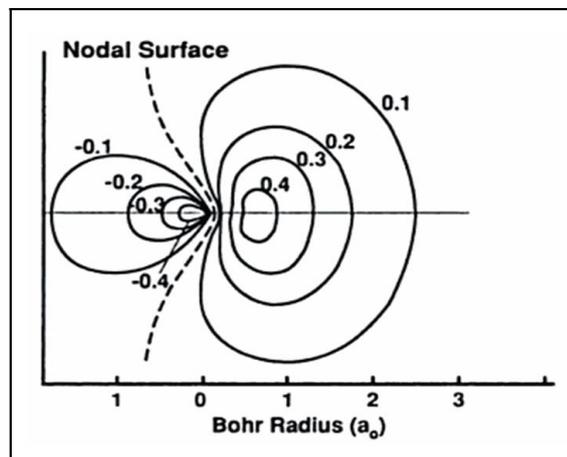


Figure 2.2: Calculated electron density contours of the sp^3 hybrid orbital [42].

2.2 Classification of Diamond

In addition to the various forms in which diamond exists in nature, progress in diamond synthesis techniques has resulted in diamonds that are specifically

Table 2.1: *Selected Physical Properties of Diamond and Silicon at room temperature (300 K)*

Physical Property (300 K)	Units	Diamond	Silicon
Energy Band Gap	[eV]	5.5	1.12
Solid State Density	[gcm ⁻³]	3.52	2.328
Electron Mobility	[cm ² /Vs]	1800-4500 (CVD)	90-1500
Hole Mobility	[cm ² /Vs]	1200-3800 (CVD)	50-450
Electrical Resistivity	[Ωm]	>10 ¹⁴ (Ia; IIa)	6.4 x10 ²
Breakdown Voltage	[V/cm]	>10 kV	600 V
Thermal Conductivity	[W/mK]	2300 (IIa)	149
Melting Point	[K]	3750-3850	1687
Young's Modulus	[GPa]	1223	130-188
Bulk Modulus	[GPa]	442.3	97.6
Shear Modulus	[GPa]	478	51-80
Mohs Hardness	[-]	10	7

designed or tailor made for different applications including radiation detectors, abrasives and biomedical applications. Nonetheless, one common feature that all diamonds share is that they all contain at least one form of defects present in the lattice. These can vary from simple point defects to lattice dislocations, impurities or a combination of different types of defects. Although defects can also be introduced into the diamond lattice (*doping*) to achieve special functionality, in general, the quality of diamonds particularly with regards to gem quality is determined by the fraction (and distribution) of impurities present in the lattice. Optical absorption measurements have shown that the most common impurity in all types of diamond is nitrogen. As a result, the fraction of nitrogen impurities as well as their distribution in the lattice is often used as method of diamond classification.

There are generally four classes of diamonds, namely Ia, Ib, IIa and IIb diamonds. Type Ib diamonds are more commonly known as natural diamonds, a relatively small fraction type Ib diamonds are of chemical vapour deposition (CVD) synthetic origin. In Ib diamond, nitrogen exists as a substitutional defect that can be either neutral or positively charged. The substitutional nitrogen defect occurs when a nitrogen atom replaces a carbon atom in its respective lattice site. The migration barrier by exchange with a carbon neighbour has been calculated to 6.3 eV [43]. Type Ib diamonds are normally yellow/brown in colour as a result of optical absorption introduced by the nitrogen defects. Two neighboring nitrogen atoms at adjacent lattice sites form a complex known as the A-centre. The A centre was initially identified from the 3.8 eV absorption line and its behaviour in diamonds containing ^{15}N by Davies *et al.* [44].

When four substitutional nitrogen atoms aggregate around a vacancy in a lattice site, the B-centre is formed (also referred to as the NV_4 centre). Diamond which contain primarily aggregated nitrogen in the form of A centres, B centres or combinations of A and B centres are classified as type Ia diamonds. With regards to the mechanism B-centre formation, it is not clear whether A-centres migrate as a unit under sufficient energy to form B-centres or whether A-centres dissociate to individual nitrogen defect that aggregate directly into VN_4 defects forming B-centres. In addition, the aggregation of four nitrogen atoms is presumed to reduce the formation energy of a vacancy-interstitial pair which results in the formation of a B-centre and a self-interstitial. The aggregation of these defects lead to the formation of *platelets* oriented along (100) crystallographic planes [45]. Diamonds that contain very low concentration substitutional nitrogen typically below ≈ 500 ppm are very rare and are referred to as type II diamonds. The substitutional nitrogen acts as a deep electron donor with an ionization energy of 1.7 eV [45]. Type II diamonds are further distinguished into types IIa and IIb, where type IIa diamonds are elec-

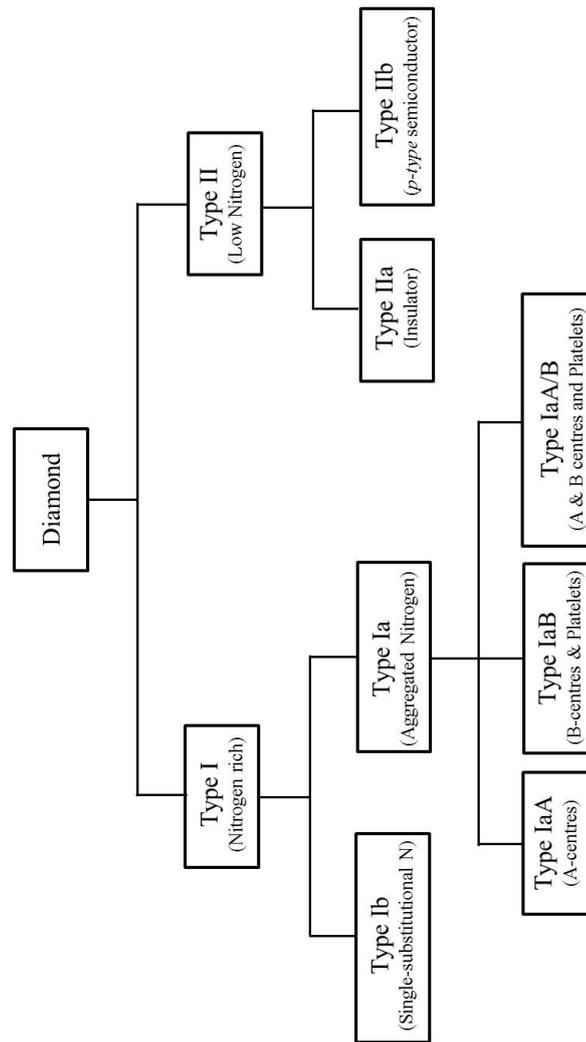


Figure 2.3: Schematic presentation of diamond classification based on nitrogen concentration and distribution.

trically insulating with resistivities above $10^{18}\Omega\text{cm}$, while type IIb diamonds are semiconducting (*p-type*) with relatively low resistivities ($5\text{-}10^5\Omega\text{cm}$) [45]. The transition into a semiconducting state is enabled by boron impurities with a concentration of less than 1 ppm that act as acceptors. A summary of the classification of different types of diamonds is shown in Fig. 2.3.

2.3 Defects in Diamond

The study of defects is of fundamental importance to the solid state physics of diamond and also provides insight to the origin of the observed physical properties of diamond. Defects or more specifically, lattice defects refer to a range of crystallographic imperfections or elemental and molecular impurities present in the lattice system. These can be intrinsic defects which are introduced into the lattice system during the growth process either naturally or by synthesis techniques such as chemical vapour deposition (CVD) or high pressure high temperature (HPHT). Alternatively, defects can be extrinsic where they are introduced into the lattice system post-synthesis e.g. by ion beam irradiation or pulsed laser irradiation.

Common crystallographic defects, include point defects (such as vacancies and interstitials) and lattice (or planar) dislocations. Although nitrogen is the most common impurity in all type of diamonds and is used a reference for diamond classification, several other impurity defects are important in diamond including hydrogen, boron and magnetic/transition metal based impurities (Fe, Mn, Cr, Ni). The presence of defects in a lattice can significantly alter the electronic band structure of the material even at very low concentrations. Therefore, defects can be either useful or retarding to the performance of materials. The careful and systemic introduction of defects into materials has been, and remains pivotal in the advancement of modern electronics and semiconductor industry and as well as in emerging fields such quantum computing and organic biomaterials.

2.3.1 Vacancy Defects

The vacancy defect in diamond is any lattice site where a carbon atom is either missing or has been removed by a physical or chemical process. Such

defects together with interstitial defects can be introduced into the lattice during the diamond growth process but are characteristic of samples that have been irradiated with high energy ion, electron or neutron beams. The vacancy defect system exhibits tetrahedral symmetry in its neutral state in the diamond crystal lattice. The system is non-paramagnetic and is commonly referred to as the V^0 defect while its optical absorption/luminescence band is known as the **GR1** band with a characteristic zero phonon line (ZPL) at 1.673 eV [45] where photon absorption occurs without any phonon intervention. At energies above the ZPL, phonon vibrations contribute in the photon absorption process resulting in vibronic side bands in the absorption spectrum.

Photo-Hall measurements suggest that the ground state energy of the V^0 defect is close to the center of diamond energy band gap ($E_g \approx 5.5$ eV) [46]. In the limit of low temperature, the radiative decay time of GR1 band is 2.55 ± 0.1 ns and is inversely proportional to temperature suggesting competing non-radiative deexcitation channels [47]. The GR1 band is associated with background absorption known as the UV-continuum which is typically observed at energies above 2.5 eV up to the fundamental absorption edge of diamond (*the energy band gap*). High resolution measurements at liquid helium temperatures revealed the existence of sharp absorption peaks in the UV-continuum that are now known as GR2-GR8 as well as the TR12 bands [48]. The GR notation which stands for *general radiation* is adopted owing to the fact that these defects are observed in all types of diamonds after radiation [49]. The generally accepted view is that the GR1 band together with the spectral features of the UV-continuum are characteristic signatures of the neutral single vacancy defect.

The negatively charged vacancy is denoted V^- while its optical absorption/luminescence band is commonly known as **ND1** band. Its negatively charged state causes a charge imbalance in its electronic system which allows

it to be effectively probed via techniques such as electron paramagnetic resonance (EPR). However, optical absorption measurements show that the ND1 band has a characteristic ZPL at 3.150 eV and have instead been used to obtain significant information regarding the N^- defect. In contrast to the GR1 band, the ND1 band has no characteristic photoluminescence band. When the ND1 band is subject to intense illumination, it deexcites by charge exchange resulting in the production of the ND1 photoconduction spectrum [50] as well an increase in the GR1 band [51]. However, the process is reversible when the material is heated in the dark (e.g. using a mercury lamp).

The substitutional nitrogen defect acts as shallow donor in diamond with an ionization energy of 1.9 eV [52]. As a result, owing to the abundance of nitrogen in natural type Ib diamonds, the ratio of the GR1 to the ND1 absorption band may approach zero in extreme cases due to dominance of V^- defects while relative pure type IIa diamonds are expected to have a neutral equilibrium charge due to the dominance of the ND1 band over the GR1 band. The overall concentration of nitrogen thus significantly affects the equilibrium charge of the material and therefore type Ib diamonds grown by synthetic means may have different equilibrium charge to natural diamonds which are expected to have negative equilibrium charge. In type Ia diamonds, the V^0 and V^- coexist with similar strengths in the GR1 and ND1 absorption bands.

Annealing effects on vacancy defects in diamond have been investigated by several authors and although much information has been achieved, numerous grey areas exist that continue to drive active research in this field. Earlier annealing studies of diamonds subjected to energetic electron beams [49, 53–55] showed that vacancy diffusion dominates from temperatures close to 600°C with an activation energy of 1.7 eV while interstitials diffuse between 275 and 600° with an activation energy of 1.3 eV. Vacancy annealing above 600°C results in the destruction of the GR1 band of V^0 defects and is correlated with

the growth of new absorption features called the **TH5** absorption which occur at GR1 pairs or divacancies which are also removed at elevated temperatures [49].

2.3.2 Nitrogen-Vacancy Defects

At temperatures from 600°C and above, vacancies carry sufficient energy allowing them to diffuse in the diamond lattice. In nitrogen rich type Ia diamonds, vacancies can be trapped at A or B nitrogen aggregates. When a vacancy is trapped at an A aggregate, it produces the VN_2 defect with an optical absorption signature known as the H3 band (Fig. 2.4) which has a characteristic ZPL at 2.463 eV. Similarly, when a vacancy is trapped at a nitrogen B aggregate it produces the V_2N_4 defect which also exhibits an optical signature known as the H4 band with a characteristic ZPL at 2.498 eV. In type Ia diamonds, the production of H3 and H4 centres is proportional to the concentration of A and B aggregates. The corresponding radiative decay times of the H3 and H4 centres are 16.7 ± 0.5 ns and 19.1 ± 0.1 ns respectively [56]. The neutral single substitutional nitrogen defect undergoes a trigonal distortion along the (111) with a carbon atom. As result, the defect does not possess tetrahedral symmetry in the diamond crystal lattice [43].

Other significant nitrogen vacancy defects in diamond are the VN_3 defect formed by trapping of a vacancy at three adjacent substitutional nitrogen atoms as well as the VN defect formed by trapping of a single vacancy at a substitutional nitrogen atom. The VN_3 defects exhibits an optical absorption signature known as the N3 centre with the most intense optical transition observed at 2.985 eV [57]. The single substitutional nitrogen defects is known as the *C* centre. The N-V defect of neutral charge (or NV^0) exhibits an optical absorption signature with a characteristic ZPL at 2.156 eV while the negatively charged N-V centre (NV^-) absorbs optical radiation with characteristic a ZPL

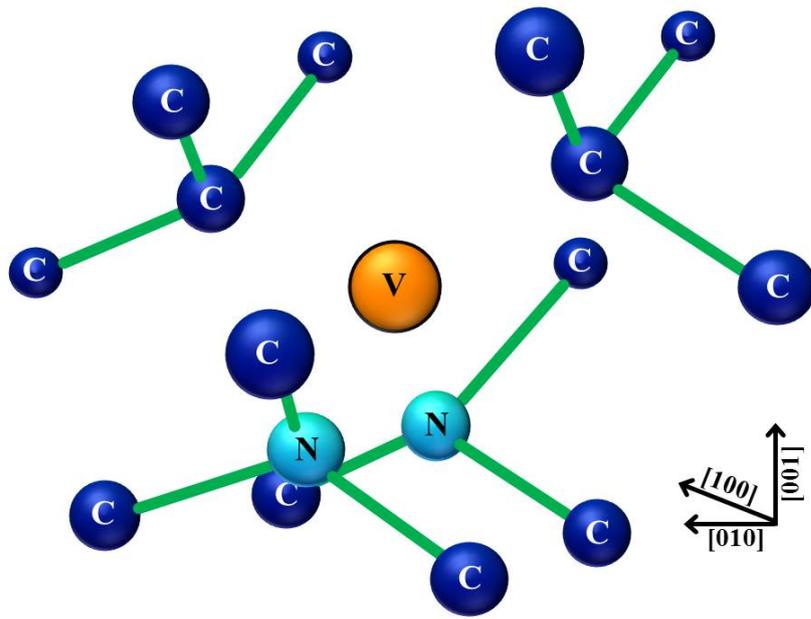


Figure 2.4: Schematic presentation of the $H3$ centre in diamond showing substitutional nitrogen defects (N) as well as the single vacancy defect (V^0) [45].

at 1.945 eV. N-V defect centres are most common in diamonds containing nitrogen in single substitutional sites.

Amongst various defects centre investigated in diamond, both experiments and calculations performed on the NV defect centre have demonstrated its exceptional properties and potential as a candidate for emerging applications in quantum information processing, spintronics and quantum cryptography. Such applications are motivated by the fact that the electron spin of the NV centre exhibits long spin coherence times that persist up to *milli-seconds* at room temperature [18]. In addition, the NV centre has been shown to be an efficient single photon source generator, a requirement for optical quantum information and quantum cryptography [19, 58, 59].

The $(NV)^-$ defect centre is a spin triplet in its ground state with a zero-field splitting of $D= 2.88$ GHz (micro-wave) between energy sublevels with spin z component $m_s = 0$ and $m_s \pm 1$ [61]. The spin system is quantized

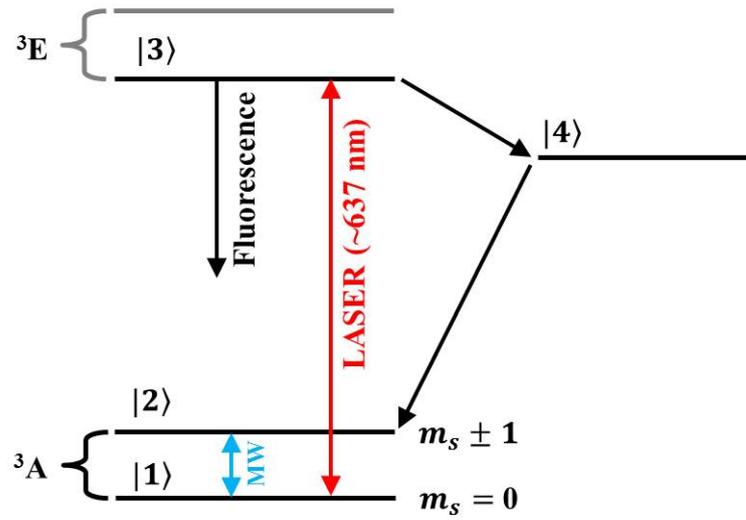


Figure 2.5: Schematic presentation of the NV centre energy level system in diamond. The grey line corresponds to the $m_s \pm 1$ excited energy sub-levels [60]. MW represents micro-wave excitation.

along the N-V symmetry axis which is the $\langle 111 \rangle$ crystal axis [63]. The defect centre can be excited optically at resonance using a excitation source of 637 nm (which corresponds to its ZPL) without associated phonon generation to a level 1.945 eV above its ground state energy (Fig.2.5). Linearly polarized optical excitation can be used to polarize the spin system from the $m_s \pm 1$ into the $m_s = 0$ state [62] through a spin dependent intersystem-crossing decay mechanism to a singlet 1A level [63]. Read-out of the spin system is enabled by the fact that the de-excitation photoluminescence intensity involving the $m_s \pm 1$ transitions is substantially lower than for the $m_s = 0$ level [64]. Although these dynamics allow individual NV centres to be optically addressed, the corresponding spin projection measurements destroy (alter) the measured quantum state [65].

Previous attempts to measure coupling of NV centre spins to e.g. light or neighboring nuclei has been associated with destruction of the measured quantum state. However, recent advances in experimental measurement techniques

Table 2.2: *Summary of common nitrogen and vacancy related defects centres in diamond.*

Defect Centre	Structural Composition	Absorption			Spectral Region
		[eV]	[nm]	[cm ⁻¹]	
A	2 adjacent N	0.159	7800	1282	Infra-Red
B	V + 4 adjacent N	0.147	8439	1185	Infra-Red
C (or P1)	N	0.140	8850	1130	Infra-Red
Platelet	B + self-interstitial	0.170	7299	1370	Infra-Red
P2 (or N3)	V + 3 adjacent N	2.985	415	24076	Visible (Blue)
H3	A centre + V	2.463	503	19880	Visible (Green)
H2	(H3) ⁻	1.256	987	10131	Infra-Red
H4	B centre + V	2.498	496	20148	Visible (Blue)
GR1	V ⁰	1.673	741	13494	Near Infra-Red
ND1	V ⁻	3.150	394	25406	Ultra-Violet
[NV] ⁰	N + V	2.156	575	17389	Visible (Green)
[NV] ⁻	(N + V) ⁻	1.945	637	15687	Visible (Red)

have resulted in successful demonstration of nondestructive measurement of single NV centre electron spins coupled to light through the Faraday effect as well as unitary single-spin manipulation of their coupled state via the optical Stark effect using a near-resonant laser field coupled to an NV-centre [65]. These measurements thus enable efficient characterization of quantum information exchange between NV centres and light. The NV centre has also been successfully coupled to neighboring electronic [66] and nuclear spins [59] thus allowing the possibility of fabricating basic building blocks (quantum bits or qubits) for performing simple algorithms and quantum memory for quantum computers.

2.3.3 Hydrogen Mediated Defects

Although nitrogen mediated defects are by far the most common elemental and molecular impurities in most types of diamonds, hydrogen impurities are prevalent in almost all diamond types either in the bulk, the surface or both. Diamonds grown under natural high pressure high temperature conditions contain a significant fraction of hydrogen and hydrogen mediated impurities introduced during the growth process. However most good quality single crystal synthetic diamonds either grown by CVD processes contain negligible hydrogen in the bulk but hydrogen is found almost exclusively confined to the surface since a hydrogen atmosphere is necessary to promote and catalyze metastable growth of diamond from low pressure carbonaceous phases [67].

Surface hydrogen is typically a monolayer in thickness and is chemically bonded to the carbon atoms on the diamond surface as observed in the Doppler spreading of the nuclear resonance width [68]. Nonetheless, several other experimental techniques such as electron spin resonance (ESR), nuclear magnetic resonance (NMR), optical spectroscopy and nuclear techniques have been successfully utilized to probe the presence, location and dynamics of hydrogen in diamond. The study of hydrogen in diamond is of interest in numerous emerging applications such as nanoelectronics and spintronics due to possible hydrogen assisted variation of the Fermi level and control of bulk or surface magnetic phenomena respectively.

Typical concentrations of hydrogen in diamond vary depending on the growth conditions and hence our type of diamonds. Natural type I diamonds contain the highest concentration of hydrogen in the range ≈ 500 - 3600 ppm while HPHT diamonds contain ≈ 200 - 900 ppm [69]. Polycrystalline CVD diamond can contain hydrogen at concentrations up to 2000 ppm [70]. Apart from chemically bonded surface hydrogen, studies have shown that hydrogen can also be trapped at defect sites such as grain boundaries, voids and dan-

gling bonds at vacancies in synthetic diamonds [69, 70]. Optical spectroscopy have also shown that polycrystalline diamond contains higher concentrations of hydrogen than high quality CVD diamonds in which the concentration of bulk hydrogen is almost zero [71].

Hydrogen can exist in different charge states in diamond in the form: H^0 , H^+ and H^- . These different possibilities together with the common diamagnetic behaviour of hydrogen in diamond pose several experimental challenges in studying isolated hydrogen in diamond amongst other reasons [72]. As result, its chemical analog or pseudo-isotope *muonium* has been used to provide useful information regarding the behaviour and response of hydrogen in diamond. However, *muonium* is much lighter than hydrogen ($m_\mu \approx \frac{1}{9}m_H$) and has a short life time [73]. The corresponding implications are that *muonium* can be useful to study isolated hydrogen lattice sites in diamond since *muonium* can form similar charge states as hydrogen and thus occupy the same lattice sites as hydrogen. However, due to its short life time and lighter mass, it cannot be incorporated into molecules or be used to accurately predict hydrogen-related molecular dynamics in the crystal lattice.

Both theoretical [74–77] and experimental [78] studies of muon implantation experiments indicate that H^0 is metastable at a tetrahedral interstitial site. Its lowest energy configuration consists of Hydrogen at or close to the bond centre. Theoretically investigations [79] have shown that the lowest energy configuration of the H^+ impurity in diamond is in the puckered bond centre site with a C-H-C bond angle of 100° while the lowest energy configuration for the H^- defect is found to be in the bond centre site. The H_2^* complex (one H atom at the bond centre site (H_{BC}) coupled to a H atom at a neighboring antibonding site) is found to be stable in the diamond crystal lattice [80]. It has also been shown that hydrogen located at the tetrahedral interstitial site (H_T) can migrate to other tetrahedral sites with a migration barrier of 0.37

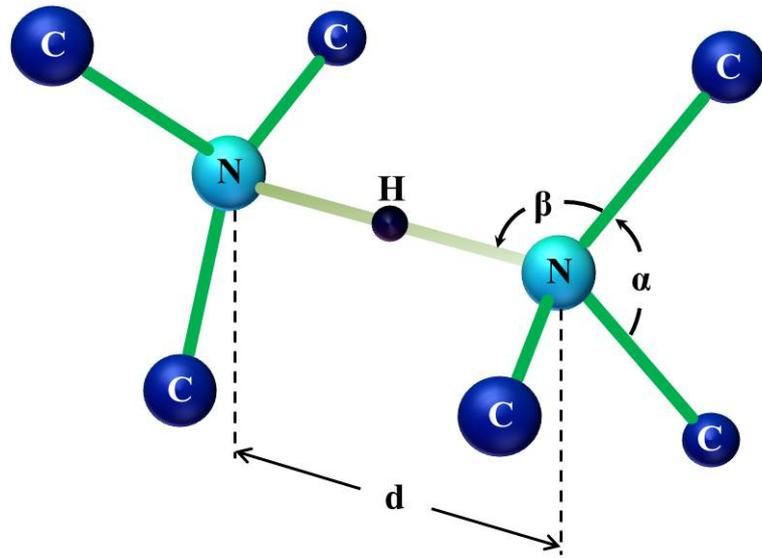


Figure 2.6: *Optimized structure of the N-H-N defect consisting of the hydrogen defect located between two adjacent A centres with $d=2.20 \text{ \AA}$, $\alpha=117.0^\circ$ and $\beta=100.0^\circ$. Reproduced from Miyazaki et al. [87].*

eV [81].

In general, hydrogen is very stable in the diamond lattice. Amongst several studies this stability has also been evidenced by micro-scanned Heavy Ion Elastic Recoil Detection Analysis (HI-ERDA) and Nuclear Reaction Resonance Analysis (NRRA) experiments on well characterized H^+ implanted diamond samples at temperatures up to 1470 K [82–84]. It has been proposed that such stability could be related to H_{BC} and H_2^* hydrogen configurations [72]. Hydrogen either in intrinsic form or introduced into the crystal lattice by simple irradiation and co-doping is known to form several complexes in different type of diamonds. These include hydrogen-nitrogen, hydrogen-boron, hydrogen-phosphorus and hydrogen-sulphur complexes. Co-doping has been studied as a possible method to tailor variations in the electronic properties of diamond for novel high end applications. Due to its relevance in the present study we discuss only the hydrogen-nitrogen complex briefly as numerous studies have

been conducted on various hydrogen complexes in diamond [79, 85–91].

The structure of the hydrogen-nitrogen complex is arranged such that the hydrogen defect is located at the bond center site. More specifically, the hydrogen defect lies $\approx 1.06 \text{ \AA}$ from the neighboring carbon atom and $\approx 1.20 \text{ \AA}$ from the adjacent substitutional nitrogen defect with an overall binding energy of 1.49 eV [89]. Miyakazi *et al.* [87] proposed a hydrogen-nitrogen complex model a structure consisting of an A centre and a hydrogen impurity located in the bond centre between two substitutional nitrogen defects that has an overall formation energy of $\approx 4\text{-}5$ eV and produces a shallow donor level in diamond (Fig.2.6).

Although phosphorus can act as a representative candidate for a shallow dopant in diamond with a donor level $E_d \approx 0.5$ eV [92], the high formation energy (for the substitutional site) causes low solubility [93] and results in an inefficient incorporation into the diamond lattice [94] thus reducing the hole mobility to $\sim 200 \text{ cm}^2/\text{Vs}$ [95] compared to $\sim 2000 \text{ cm}^2/\text{Vs}$ in the case Boron-doped diamond [96]. The idea of proposing such N-H-N defects centre in diamond challenges the conventional conception of nitrogen acting as a deep donor in diamond. The N-H-N complex may make the nitrogen donor in diamond much shallower than an isolated substitutional nitrogen donor ($E_d \approx 1.7$ eV) [87] and this effect may be useful for producing (*n-type*) semiconducting diamond for specialized applications.

Chapter 3

Highly Charged Ions

3.1 Overview

The phrase highly charged ion (HCI) is generally used to refer to a range of ions in different energy regimes. This includes *multiply charged ions* (MCIs) at the lower end of the HCI spectrum, *very* highly charged ions at the higher end of the HCI spectrum and an intermediate potential energy regime. MCIs are ions that have several electrons removed from their neutral state, typically $Q \approx 2-9$ with neutralization energies $E_0 < 1$ keV. In contrast to MCIs, *very* highly charged ions have a relatively large number of electrons removed from their neutral state e.g. $Q = 92$ with $E_0 \sim 750$ keV [6]. In addition to their potential energy, the velocity (kinetic energy) of HCIs is also used as a property that further classify HCIs. We refer to *slow* highly charged ions (SHCIs) as HCIs with velocity $\nu < \nu_{Bohr}$ where ν_{Bohr} is the Bohr velocity and represent the orbital velocity of the outermost electrons in neutral atoms, $\nu_{Bohr} \approx 2.19 \times 10^6$ ms⁻¹ [97].

The SHCI nuclear system is therefore slower than the electron motion around the respective nuclei. The ratio of the Bohr velocity to the speed of light is equivalent to the *fine structure constant* (1/137) which also repre-

sents the coupling constant between electrons and photons. Therefore beyond the Bohr velocity, physical processes (e.g. electron capture) involved in the interaction between HCIs and matter as well as their characteristic scales may vary significantly. Primary questions that HCI related research aims to address include [97]:

- mechanisms of energy exchange during HCI interaction with condensed matter
- potential applications of the surface response

Multi-charged ions considered in the present study have charge states $Q \gg 1$, neutralization energies $E_0 \gg 10$ eV and velocities $\nu < \nu_{Bohr}$ and are therefore regarded as *Slow Highly Charged Ions* (SHCIs).

3.2 Fundamental Aspects

The nuclear and electronic charge phase space (Z, Q) of all HCIs can be described by either an *isonuclear* sequence or an *isoelectronic* sequence. In the former, a nucleus of charge Z is fixed while the electron charge is varied beginning at $Q=1$. The latter case considers a fixed electronic charge Q while the nuclear charge Z is varied from $Z=N+1$ for $N=Z-Q$. All positive ions that can be produced in this manner across the periodic chart are predicted to be stable within the framework of elementary quantum mechanics. However, in practice isonuclear sequences are more relevant from an experimental perspective. Along any isonuclear sequence, an increase in the HCI charge state results in compression of the spatial wavefunction due to decreasing distance from the nuclear core to the outermost electrons which increases the nuclear attraction. Consequently, the size of HCIs differs largely with that of neutral atoms.

For *very* highly charged ions as in hydrogen-like ions (HCIs with a single

electron) with large nuclear charge the physics can differ drastically to the case of MCIs and HCIs of intermediated neutralization energies e.g. U_{238}^{91+} which has an electron density $\approx 78 \times 10^4$ times higher than that of hydrogen. In such systems, the Bohr radius ($R \sim 50/Z$ pm) falls below the fundamental length scale at which the electron ceases to behave as point particle with finite charge (i.e. the Compton wavelength, $\lambda_c \approx 2$ pm). Single particle quantum mechanics and the classical concept of a central Coulomb potential begin to break down and description of the system thus requires Quantum field theory (QFT) which also has to consider the structure of the vacuum itself [6]. A simple scaling law for hydrogen-like ions predicts $R \sim 1/Q$ where $Q \gg 1$ for the size of the HCI system [6].

For most purposes in ion-solid interaction studies, HCIs are characterized by their kinetic and potential energy. In ion-beam applications, the HCIs are extracted at a tunable voltage, V_{ext} . This voltage determines the kinetic energy of the HCIs such that $E_{kin} \approx V_{ext} \times Q$. In conventional ion-beam applications, the typical potential energy is equivalent to the single charge ionization potential ≈ 10 eV which is sufficiently low to be neglected. However, in the case of HCI and SHCIs the potential is substantially higher and plays a significant role in the mechanisms of HCI interaction with surfaces.

The potential energy of any highly charged ion is equivalent to sum of its individual ionization potentials. Different methods have been employed in the approximation of ionization potentials for all atomic structures across the period chart. Carlson *et al.* [98] performed calculations for elements up to $Z=103$ for ionization states using a simple spherical shell solution for neutral atoms. In this approach, the atom is simplified to a set of concentric spheres where the binding energy of an electronic shell nlj in the ground state of an ion with charge N , $\varepsilon_{nlj}(N)$, can be obtained from binding energies $\varepsilon_{nlj}(0)$ and

mean radii \bar{r}_{nlj} of the neutral atom by the relationship:

$$\varepsilon_{nlj}^*(N) = \begin{cases} \varepsilon_{nlj}^*(0) + \sum_{nlj} \frac{q_{nlj}(N)}{\bar{r}_{nlj}} & \text{if } [\bar{r}_{nlj} \geq \bar{r}_{nlj}^*] \\ \varepsilon_{nlj}^*(0) + \sum_{nlj} \frac{q_{nlj}(N)}{\bar{r}_{nlj}^*} & \text{if } [\bar{r}_{nlj} < \bar{r}_{nlj}^*] \end{cases} \quad (3.1)$$

where $q_{nlj}(N)$ is the number of electrons removed from shell (nlj) for an ion of charge (N). The asterisk is used to indicate the orbital whose energy is being calculated. When computing the ionization potentials of a given element, ε_{nlj} and \bar{r}_{nlj} are obtained from eigenenergies and mean radii in SCF (i.e. self-consistent field methods of Hartree and Fock) solutions for neutral atoms [98]. The calculated ionization potentials showed up to 5% deviation on average from available experimental data. Recent calculations of ionization potentials and potential energy (neutralization energy) of HCIs have been performed based on multiconfigurational Dirac-Fock (MCDF) methods using the general relativistic atomic structure package (Grasp) [99]. Figures 3.1 & 3.2 and show ionization potentials and potential energies calculated for xenon and bismuth HCIs based on MCDF and SCF methods.

The approximations are very similar for low nuclear charge HCIs (Fig. 3.1) while the differences are more pronounced with increasing nuclear charge (Fig. 3.2). The ionization potential of HCIs increases rapidly with charge state. For one-electron ions (hydrogen-like HCIs), simple Coulomb potential scaling predicts that this rapid increase is due to two fundamental factors [6]:

- increased magnitude of nuclear charge
- reduction of the distance from the nuclear centre of mass to the single electron.

This gives the simple relation: $U(Z) \sim Z/R \sim Z/(1/Z) = Z^2$. For multi-electron systems, the increase in the ionization potential with charge along an isonuclear system will be reduced compared to hydrogen-like HCIs and also less smooth, reflecting the atomic shell structure and the variation in elec-

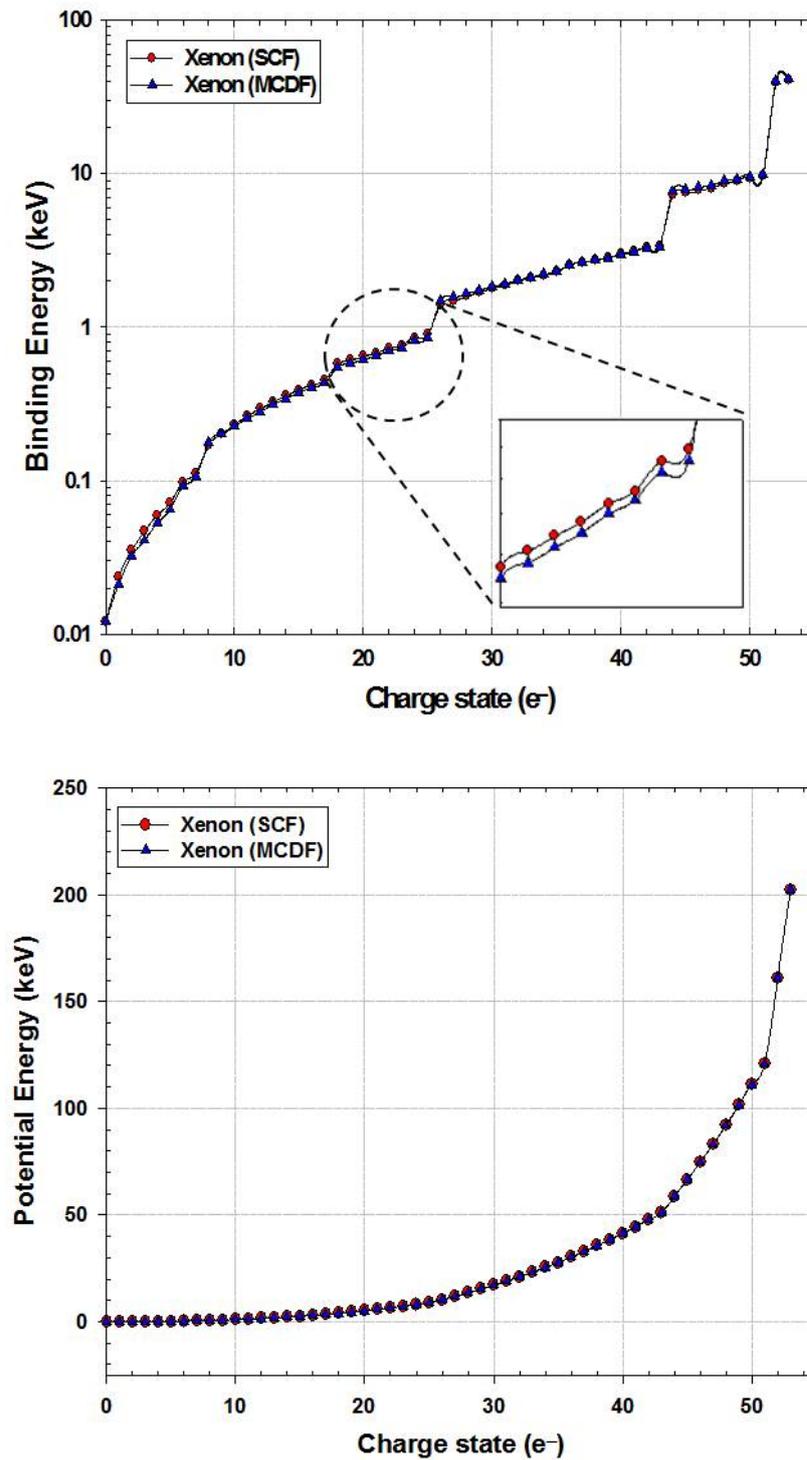


Figure 3.1: *Top image: Electron binding energy (ionization potential) of xenon HCIs. Bottom image: Potential energy of xenon HCIs. The data is calculated using MCDF methods (triangles) employed in the Grasp code and SCF methods (circles) used in the spherical shell model.*

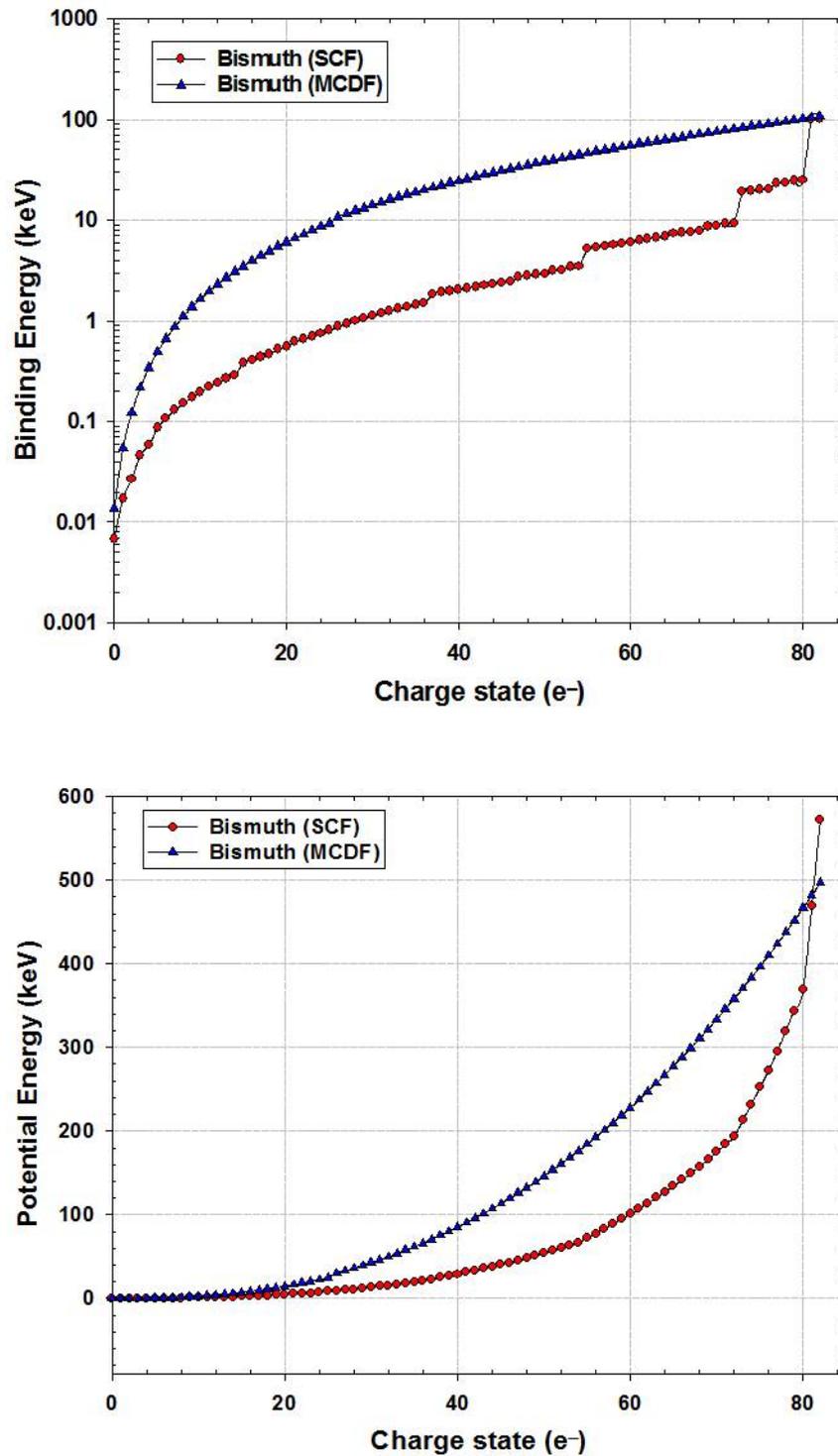


Figure 3.2: *Top image: Electron binding energy (ionization potential) of bismuth HClIs. Bottom image: Potential energy of bismuth HClIs. The data is calculated using MCDF methods (triangles) employed in the Grasp code and SCF methods (circles) used in the spherical shell model.*

tronic screening. However, in the high charge limit i.e. ($Q \rightarrow Z$) all HCIs will approach a Q^2 enhancement of ionization potential [6]. Therefore since the potential energy of any HCI is defined as the sum of all its ionization potentials, it will also be enhanced by the discussed enhancement in the ionization potentials of the HCIs in the summation.

3.2.1 Interactions of HCIs with matter

Experimental studies of interactions between accelerated ions and matter, in particular solid state materials, has been limited to accelerated singly charged ions for many years. This limitation has been primarily due to the lack of highly charged ion sources of sufficiently high brightness and charge state. In addition, due to the lack of adequate and effective high resolutions surface imaging techniques such as scanning probe microscopy (SPM), these investigations have been primarily focused on bulk effects $z > 1 \mu\text{m}$ that are observable by techniques such as Raman and X-ray spectroscopies and Nuclear microscopies. Transmission electron microscopy (TEM) has been useful in characterizing defects created along the ion path of fast singly charged heavy ions (i.e. ion tracks). However, TEM imaging requires samples that are transparent to $\sim 1 - 10^2$ keV electrons, therefore, the nominal sample preparation requirement has placed further limitations in the scope of feasible experimental investigations. On the hand, although theoretical investigations of ion-solid interactions have proved useful, results could not be verified by observations.

The development of highly charged ion sources with controllable ionization states even up to *very* high charged states e.g. U_{238}^{92+} as well as high resolution surface imaging techniques in the 1980s has been pivotal in the progress of HCI-solid interaction studies. HCIs in particular SHCIs carry large potential energy relative to conventional singly charge ions. The potential energy of SHCIs can be comparable to its kinetic energy and even significantly exceed

the kinetic energy in highly charged states. A schematic summary of SHCI interaction with surfaces including hollow atom formation and decay is shown in Fig. 3.3. When a SHCI approaches a surface, the charged particle induces a charge distribution in the surface known as the *image charge* which is related to the dielectric response of the surface resulting in a localized electric field. The field produced by the image charge is sufficient to accelerate the approaching SHCI towards the surface and thus sets a lower limit to the impact velocity of the SHCI. The energy gain due to the image charge of a HCI of charge state q is given by [100]:

$$\Delta E_{q,im} \approx 1.2q^{3/2} (eV) \quad (3.2)$$

The SHCI therefore approaches the surface with a velocity resulting from the image charge acceleration and the extraction potential of the SHCIs from the ion source. The SHCIs' screened Coulomb potential and the image potential of both the electron and the SHCIs form a potential barrier for electrons between the surface and the approaching SHCI. This potential barrier is inversely proportional to the inter projectile-surface distance and will drop below the Fermi level at a critical distance R_c for $q \gg 1$ according to the classical-over-the-barrier model (COB) [101]. Interaction of the SHCIs with the surface begins before contact with the surface from a distance R_c above the surface. From this distance towards the surface, electronic emission of surface valence band begins under influence of the SHCI potential field. The emitted electrons are resonantly captured by the approaching SHCIs into high lying quasi-stationary Rydberg states which overlap with filled surface valence band states (i.e. resonant neutralization). This then creates an unusual transient atom with unoccupied core states state which is referred to as a *hollow atom* [102]. The onset of hollow atom formation is therefore given by [101]:

$$R_c(q) = \frac{1}{2W_\phi} \sqrt{8q + 2} \approx \frac{\sqrt{2q}}{W_\phi} \quad (3.3)$$

where W_ϕ is the work function of the target material. In the transient

formation of the hollow atom, electrons are resonantly captured into excited projectile states with hydrogenic principal quantum numbers given by:

$$n_c \approx \frac{q^{3/4}}{W_\phi^{1/2}} \text{ (a.u.)} \quad (3.4)$$

The multiply excited neutral hollow atom is short-lived and can last for typically 100 *fs* during its approach to the surface [103]. In their approach to the surface, hollow atoms decay via auto-ionization and other Auger related processes. Electrons in higher atomic orbitals can collapse into deeper atomic orbitals with simultaneous emission of low energy (~ 10 eV) Auger electrons by virtue of the Auger effect. Resonant ionization can also take place where electrons of the multiply excited hollow atom high lying Rydberg levels are resonantly transferred to occupied surface state with binding energy less than the surface work function W_ϕ . Auger neutralization (or *Auger capture*) can also take place where electrons are ejected from surface valence band states and captured into high lying Rydberg states provided that the SHCI potential energy exceeds W_ϕ . The capture of one valence band electron is associated ejection of another electron with kinetic energy $E_e \leq W'_i - 2W_\phi$ from the hollow atom [104]. Neutralization of the hollow atom by auto-ionization occurs after multiple resonant neutralization processes. At close proximity to the surface the image potential will accelerate the decaying hollow atom towards the surface. Complete neutralization of the hollow atom before impact with the surface is therefore prohibited by the limitation in the available interaction (neutralization) time as a result of the image potential (particularly for the case $q \gg 1$).

Upon impact with the surface, the high lying Rydberg states of the decaying hollow atom are 'peeled off' and deeper shells with higher binding energies (e.g. M, L, K) are occupied through Auger neutralization from valence and or conduction band electrons [105–107]. Depending on the velocity, ionization state of the SHCIs and properties of the target material, the hollow atom can

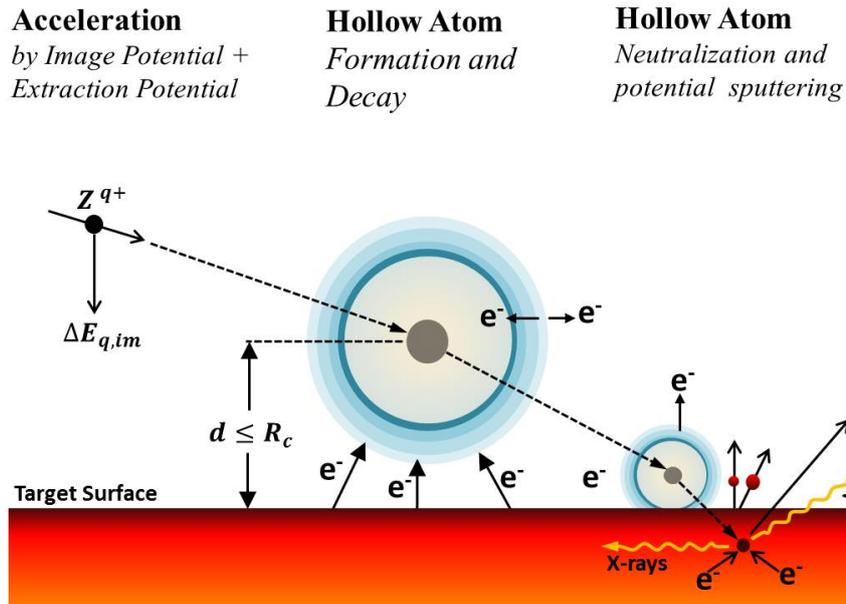


Figure 3.3: Schematic summary of SHCI interaction with a surface. The terms $\Delta E_{q,im}$ and R_c represent the image charge energy gain and the critical distance, respectively. Ultimate neutralization of the hollow atom can take place several monolayers beneath the surface.

neutralize completely at close proximity to the surface or at several monolayers beneath the surface. In latter case, the hollow atom can further decay via emission of fast Auger electrons and/or soft x-rays, depending on the projectile fluorescence yield [104] and side feeding with neighboring atoms in the surface region. In this manner, a fraction of the initial potential energy stored in the SHCI is converted into kinetic energy of the target electrons and electronic excitation of a localized surface region. This electronic excitation consists of electron-hole pairs, 'hot holes' in the conduction and or valence band of the target as well as inner-shell holes of target atoms [103]. The latest stages of hollow atom neutralization which involve the recombination of inner shell vacancies may also occur via soft x-ray emission [104].

In metals, the distortion in the electronic structure can be restored in a reasonable time due to the typically high electron mobility and the density of

electron states. In the case of insulators and materials of low conductivity, the interaction process can be dramatically different. The SHCI induced electron emission can create a charged region on the surface resulting in an electric field with a resultant vector that is anti-parallel to the SHCI motion (space charge). This can create a so called *trampoline effect* in which the approaching SHCI can be repelled from the surface. However, experimental reports on such an effect have not been conclusive [108, 109]. In most experimental studies, the trampoline effect is not observed instead, sudden modification of the near-surface electronic structure resulting from the significant fraction emitted surface electrons cannot be replenished within a time frame less than the neutralization time of the SHCIs and hollow atoms.

The ultimate result is the formation permanent surface modifications such as nanoscale defect formation, desorption and sputtering. This process is the basis of *potential sputtering* in contrast to *kinetic sputtering* encountered in interactions between fast heavy ions of negligible potential energy with materials. Numerous experimental studies involving the interaction between SHCI with different materials have been conducted to date. This achievement has been partly enabled by the almost parallel improvement in resolution and versatility in surface imaging instruments such as SPM techniques. The large electron emission associated with SHCI-surface interactions has been particularly useful in gaining insight into SHCI-surface interaction processes.

In diamond studies, electron emission has attracted much interest as a mechanism for single SHCI impact detection for single implantation used in the fabrication of qubits for quantum computing. Figure 3.4 shows a plot of electron emission yield as a function of charge state following impact of Xe SHCIs with insulating type IIa and semiconducting type IIb diamonds and also Aluminium [110]. These results show that in addition to numerous extraordinary properties of diamond earlier discussed, diamond materials also exhibit

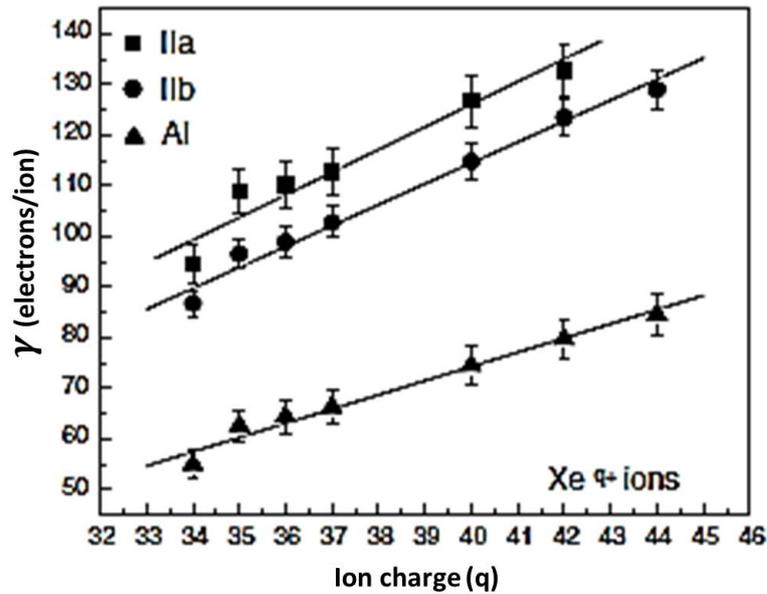


Figure 3.4: *Electron emission yields as a function of ion charge state, q following impact of xenon SHCI on type IIa diamond (square symbols), type IIb diamond (circles) and a reference Aluminum target (triangles) [110].*

supreme electron emission yields. In addition to the large emission yields, studies have shown that impact of SHCI with clean atomically flat surfaces can form highly localized permanent surface modification in certain materials including diamond, the hardest naturally occurring material on the Mohr scale. These post impact surface effects can be useful from the prospect of conducting controlled surface nanostructuring of materials and also in monitoring radiation effects in particle accelerators and nuclear fusion reactors.

An example of morphological surface modifications following SHCI impact is shown in Fig. 3.5 [111]. Although experimental investigations have revealed much information regarding the surface morphological changes following SHCI impact in most materials, the theoretical understanding of the mechanisms responsible is not completely understood and very few reliable models are available for quantitative analysis of the interactions. Nonetheless, several models in literature have been proposed for the interaction mechanism. In

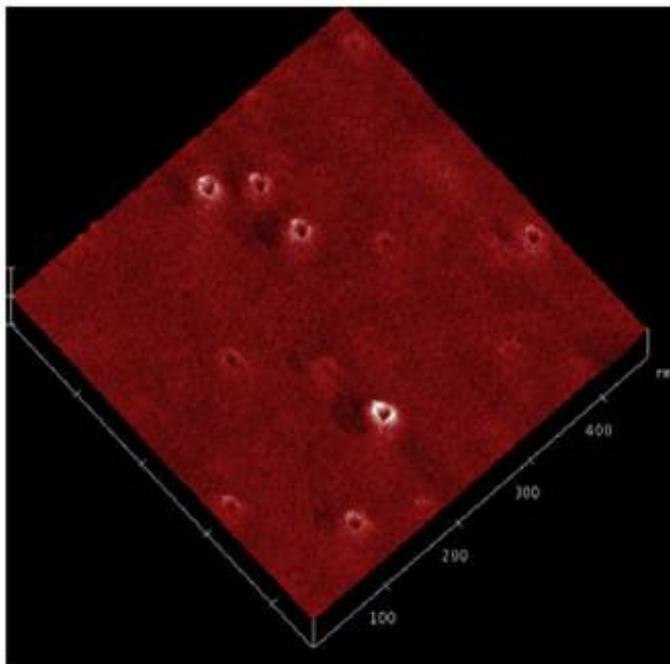


Figure 3.5: *Non-contact mode AFM topography image of nano-scale defects on HOPG bombarded with Sb^{18+} SHCIs [111].*

the present study, we consider the Coulomb explosion model (CE) [112–116], the inelastic thermal spike model (iTS) [117–121], the analytical thermal spike model (aTS) [122–124] and the defect mediated sputtering (or desorption) model (DS) [125–129].

3.3 Interactions of HCIs with Matter

3.3.1 The Coulomb Explosion Model

Initially proposed by Parilis and co-workers [112–114], the Coulomb explosion model (CE) proposes that during interaction between HCIs and solid surfaces, the large number of electrons emitted from the surface creates accumulation of positively charged ions in the near surface region. In insulating materials, the low electron mobility prohibits the restoration of the surface electronic

structure within the interaction time. As a result, mutual Coulomb repulsion of positive ion cores in the surface results in the ejection (explosion) of secondary ions from localized positively charged surface domains. Subsequent shock waves generated by this CE then further ablates the target material by emission of neutral surface atoms and clusters.

The main argument against the CE model is that even in insulators, hole lifetimes are short enough to facilitate re-neutralization before the lattice can respond [127]. However, it has been argued that hole lifetimes might become considerably longer when many holes are generated in close vicinity [97, 130]. Nonetheless, it is generally accepted that the CE model may be feasible only for interactions between *very* highly charged ions with insulating surfaces [97]. Several studies of CE models in insulators include qualitative interpretation of empirical data and also simulations based on molecular dynamics (MD).

In the present study we consider the analytic model given by Parilis [131]. It has been supposed that the charged domain formed under SHCI impact is a hemisphere with radius R_0 , and it could be calculated from an energy balance equation. The total neutralization energy W_q of a q -charged projectile is shared between the Coulomb repulsion energy E_c and the kinetic energy E_k of the $(N_q - q)$ Auger electrons where N_q is the number of ions which are created at the Auger neutralization of the q -charged ion. Following Arifov *et al.* [132], it was assumed that $N_q \approx q^2$, however, this assumption is only justified provided q is not very large. The number of the ions created per unit time in the charged domain equals N_q/τ_i where τ_i is the effective time of total Auger neutralization of a q -charged ion. Simultaneously, during the time τ_e they are neutralized by the electrons of the solid. For an insulator, $\tau_e \gg \tau_i$ and for a metal $\tau_e \ll \tau_i$. As a result, the charged domain at the moment τ_i consists of $N(\tau_i)$ ions.

$$N(\tau_i) = N_q(\tau_e/\tau_i)[1 - \exp(-\tau_i/\tau_e)] \quad (3.5)$$

The electrostatic energy of a uniformly charged hemisphere is given by $E_c = 0.32\pi^2 n^2 e^2 R_0^5 / \varepsilon$, which enters into the energy balance equation that can be used to determine N and therefore R_o since $N = (2/3) n\pi R_o^3$,

$$W_q - qe\varphi = 0.55 (n\pi)^{1/3} e^2 N^{5/3} / \varepsilon + (N_q - q) E_e \quad (3.6)$$

where n is the number of atoms per unit volume, e is the electron charge, φ is the work function of the target surface, ε is the absolute dielectric constant and E_e is the mean energy of the Auger electrons. For metals $N=0$, but in non-metals, the Coulomb energy of the charged domain has to be taken into account for both secondary ion and electron emission. If the hollow atom (HA) penetrates the solid, then the HA is neutralized on a path $h = \nu_i \tau_i$ where ν_i is the ion velocity. The region in which the surface ions are produced can be regarded as a uniformly charged cylinder of length h and radius R with a hemisphere at its end. Under Coulomb repulsion the atom ionized by the SHCIs acquire kinetic energy that can be determined by solving the equation of motion. At a given point, the velocity component normal to the surface of the solid, $\nu(x, y, z)$ is determined by the equation

$$d\nu_n(x, y, z) / dt = eE'_n(x, y, z) / M \quad (3.7)$$

where E'_n is the normal component of the electrical field, and M is the atomic mass. The normal component of the electrical field can be derived to a first order approximation (relevant for low to intermediate q) as,

$$E'_n(r, h) = \pi n e (R - 0.49r) (R - 2.7h) / R\varepsilon \quad (3.8)$$

where r and h are the distance and depth from the center of the hemisphere respectively [116]. During the time of neutralization, τ_e , the force eE'_n can be regarded as constant. Then solving eq. (3.7), one obtains an equation for the kinetic energy of the motion normal to the surface,

$$E_{kin} = M\nu_n^2 / 2 = E_n'^2 e^2 \tau_e^2 / 2M \quad (3.9)$$

A particle can escape the surface if its normal energy exceeds the surface binding energy, $E_n > E_b$, i.e.

$$E_n > (2ME_b)^{1/2} / (e\tau_e) \quad (3.10)$$

The total kinetic energy of the ions then obtained in the Coulomb explosion process is equal to the deposited energy,

$$E_d = \int_v \frac{E_n'^2 e^2 \tau^2}{2M} n dV \quad (3.11)$$

where V is the volume of the charged region. The neutralization time is related to the conductivity of the target material by,

$$\tau = 1.54M^{1/2}\varepsilon^{1/2}/en^{1/2} \quad (3.12)$$

The dynamics process of target atoms is followed by a high temperature and high pressure impulse in the plasma region. For the multi-ion system, the temperature is given by,

$$T(\tau) = \sum_i (M_i \nu_i^2 / 3k_B N) = E_{kin}(\tau) / 3k_B N, \quad (3.13)$$

where k_B, M_i and ν_i refer to the Boltzmann's constant, the mass and velocity of the i^{th} ion respectively. The corresponding pressure of the system is given by [116],

$$P = nk_B T(\tau) \quad (3.14)$$

However, In the case of very highly charged ions, i.e. $q \rightarrow Z$, the normal component of the electric field can be derived to a second order approximation where $z/R \ll 1$ as,

$$E_n(r, z) = \pi neR [1 - 0.49(r/R) - 0.25(r/R)^2 - 2.7(z/R)] / \varepsilon. \quad (3.15)$$

and ion velocity after passing the surface barrier equals

$$\nu_n(r) = \left[(E'_n(r, z) e\tau/M)^2 - 2E_b/M \right]^{1/2} \quad (3.16)$$

The above model is constructed on the basis of hemispherical charge accumulation. It is therefore expected that it can be useful for modelling surface features of similar geometries. Since ion induced surface damage can vary significantly in geometry (e.g. tracks, hillocks, craters), empirical studies are therefore necessary to refine the application of the model to different scenarios in practice.

3.3.2 The Inelastic Thermal Spike Model

The iTS model [133–135] was initially developed to explain the appearance of ion tracks in matter induced by the slowing down of energetic particles. In the iTS model energy imparted by energetic particles (typically swift heavy ions) is first deposited and shared in the electronic system of the target material. Energy is then transferred to the atoms via electron-phonon coupling resulting in a temperature increase along the ion path. Several experiments have shown that the iTS model can quantitatively describe various physical effects of swift heavy ion irradiation in metals [134, 136, 137].

The electron mobility of any material investigated using the iTS model is therefore a critical parameter in the modelling and can vary to a significant extent from metals to insulators. In insulators, the electron-lattice coupling is stronger than in metals therefore a larger increase in temperature is expected along the ion trajectory [138]. Therefore the iTS model is commonly modified when applied to insulators [121, 138]. In iTS mathematical description, two coupled differential equations govern the energy diffusion into the electron subsystem and into the atomic subsystem [118]. A time-dependent transient

thermal process coupling these two systems can be expressed in cylindrical geometry whose axis is the ion path:

$$C_e \frac{\partial T_e}{\partial t} = \nabla (K_e \nabla T_e) - g(T_e - T_a) + U(r, t) \quad (3.17)$$

$$C_a(T_a) \frac{\partial T_a}{\partial t} = \nabla (K_a(T_a) \nabla T_a) + g(T_e - T_a) \quad (3.18)$$

where $T_e, T_a, C_e, C_a(T_a)$ and $K_e, K_a(T_a)$ are the temperature, the specific heat and thermal conductivity of the electronic and atomic systems respectively, g is the electron-phonon coupling constant [118]. $U(r, t)$ is the energy density supplied by the incident ions to electronic system at radius r and time t such that integration of $U(r, t)$ over time and space gives the total electronic stopping power ($S_e = dE_e/dx$). According to the delta-ray theory in energetic ion irradiation [139], the radial energy deposition may be described as:

$$U(r, t) = bS_e \exp(-(t - t_0)^2 / 2\sigma_t^2) F(r) \quad (3.19)$$

t_0 is the mean free flight time of the delta ray electrons [140] and is of the order of 10^{-15} seconds. The half width of the Gaussian distribution σ_t is assumed to be equal to t_0 . $F(r)$ is a spatial distribution function of delta-electron energy deposition in matter, which has been given by Waligorski *et al* [141], and b is a normalization constant such that:

$$\int_{r=0}^{r_m} \int_{t=0}^{\infty} bS_e \exp(-(t - t_0)^2 / 2\sigma_t^2) F(r) 2\pi r dr dt = S_e \quad (3.20)$$

where r_m is the maximum range of electrons projected perpendicular to the ion path. Since these parameters are temperature dependent, the coupled differential equations are non-linear and can only be numerically solved. Taking into account the latent heat of fusion when the lattice temperature reaches

the melting point, the radii of molten regions induced by energetic ions can be deduced [134].

In the case of insulators and other band gap materials, only electrons excited to the conduction band, and the corresponding holes in the valence band carry energy. In addition, the number of excited electrons and holes varies over space and time [121]. To ensure that the number of free electrons and holes (carriers pairs) are properly accounted for Daraszemics and Duffy [121] introduced a further conservation to the above model following studies of semiconductors [142],

$$\frac{\partial N}{\partial t} + \nabla J = G_e - R_e \quad (3.21)$$

where N represents the concentration of electron-hole pairs (carriers), G_e and R_e are the source and sink terms respectively and J is the carrier current density, which is related to the concentration, electronic temperature (T_e) and band gap (E_g) by:

$$J = -D(T_a) \left(\nabla N + \frac{2N}{k_B T} \nabla E_g + \frac{N}{2T_e} \nabla T_e \right) \quad (3.22)$$

where $D(T_a)$ is the ambipolar diffusivity. The carrier density, U , is a combination of the band gap (E_g), and the electronic temperature, such that $U = NE_g + 3Nk_B T_e$. In the extended model [121], the conservation equation relates the carrier concentration and the electronic energy balance by:

$$\frac{\partial U}{\partial t} + \nabla W = U_{so} - U_{si} \quad (3.23)$$

where U_{so} and U_{si} are the source and sink terms and W is the energy current density given by:

$$W = (E_g + 2k_B T_e)J + (\kappa_e + \kappa_h)\nabla T_e \quad (3.24)$$

where κ_e and κ_h are the electron and hole thermal conductivities. In band gap materials, N varies in space and time therefore the electronic temperature diffusion of the two-temperature model Eq.(3.17), must be replaced by Eqs.(3.23) and (3.25). In the lattice or atomic thermal diffusion equation, Eq.(3.18), the energy exchange term is replaced by U_a . Following Mao *et al.* [143], we have:

$$U_a = C_e \frac{T_e - T_a}{\tau_e} \quad (3.25)$$

where τ_e is the electron-lattice relaxation time. The electronic heat capacity (C_e) is proportional to N since ($C_e = 3Nk_B$) because only the carriers are able to exchange energy with the lattice. The extra complexity introduced by the third conservation equation offers the possibility of including a rich variety of mechanisms into the model such as Auger recombination and impact ionization in addition to energy exchange between the lattice and the carriers [121].

Although the iTS model has been primarily used for analysis ion tracks induced by swift heavy ion (SHI) irradiation in different materials, recent studies of SHCI impacts on CaF₂, have shown that iTS model can be used to interpret the observed morphology of surface nanodefects and the ion energy dependence thereof particularly in relation to material thermal parameters [120].

3.3.3 The Analytical Thermal Spike Model

The primary difference between defects induced by *SHIs* and *SHCIs* is that in the case of SHIs the ion penetrates $\sim 1 - 10^2 \mu\text{m}$ into the bulk of the material. The resulting defects are essentially cylindrical in geometry. However, near

the end of the ions' trajectory, stopping or energy loss of ions is dominated by elastic collisions with atomic nuclei in the target material resulting in enhanced lattice damage near the end of range.

On the other hand, impact of SHCIs with solid surfaces generally creates surface damage within $\sim 1 - 10$ nm. For this reason, SHCIs are more attractive from the perspective of conducting surface nanostructuring and material modification with minimal damage to the target material. The main similarity between SHI and SHCI irradiation studies is that in both cases, irradiation induces intense electronic excitation within a very short time frame. Such short time scales enable the use of thermal spike models for the analysis of HCI irradiation induced defects [4].

The ATSM described by Szenes [123,144–147] considers the atomic subsystem where the ion-induced temperature increase $\Delta T(r, t)$ is approximated by a Gaussian distribution in two dimensional (2D) cylindrical geometry

$$\Delta T(r, t) = \frac{gS_e}{\pi\rho ca^2(t)} e^{-(r^2/a^2(t))} \quad (3.26)$$

where ρ and c are the density and the specific heat given by the Neumann-Kopp's rule. In the ATSM, $t = 0$ is defined to be the instant when system attains maximum (peak) temperature, $\Delta T_p(r, 0)$ typically within ~ 1 ps after passage of the projectile [123, 138]. After the instant $t = 0$, the system temperature decreases while the spike width increases as a result of heat conduction [123].

The two parameters of the model are the efficiency g and the initial Gaussian width $a^2(0)$ which describes the temporal evolution of the system and is closely related to the full width at half maximum (FWHM) of the thermal spike. Experimental studies have been used to show that within the ion energy range 0.02-20 MeV/nucleon, the characteristic width of the thermal spike in

crystalline insulators is $a(0) = 4.5$ nm irrespective of the ion energy within the stipulated limits [144].

The amplitude of the thermal spike, Q is determined from the conservation of energy:

$$gS_e = \rho cQ + \rho\pi R^2 L \simeq \rho cQ \quad (3.27)$$

where c, L and ρ are the specific heat capacity calculated using the Dulong-Petit formula, the latent heat of fusion and the density of the material respectively. The analysis of ion tracks in TeO_2 , a material with a low melting temperature but large value of latent heat of fusion, provided evidence that L is considerably reduced under conditions of the thermal spike [124] hence the approximation in Eq.(3.33). One possibility of this observation is that the atomic structure is altered and deformed by electronic excitation even before formation of the amorphous phase [146, 148].

The g parameter in Eq.(3.33) is dimensionless and represents the fraction of the ion's initial energy which is deposited into the atomic subsystem and used to initiate the thermal spike. The ion velocity affects the size of induced tracks sizes such that the track size is generally inversely proportional to the ion velocity. This relation forms the basis of the *velocity effect*. Experimental studies have shown that g is sensitive to the velocity effect such that in the low velocity regime, i.e. when $E \leq 2.2$ MeV/amu then $g=0.4$ while in the high velocity regime i.e. when $E \geq 8$ MeV/amu then $g=0.17$ [124].

The effective radius of the ion tracks, R_e is the largest radius of the molten phase determined from the condition:

$$\Delta T(R_e, 0) = \Delta T_m = T_m - T_{irr} \quad (3.28)$$

where T_m and T_{irr} are the melting and irradiation temperatures respectively

[148]. Under these conditions and assumptions, three simple equations can be derived from Eq.(3.26)

$$R_e^2 = a^2(0) \ln \left(\frac{S_e}{S_{et}} \right); \quad \text{for } S_e < eS_{et}, \quad (3.29)$$

$$R_e^2 = \frac{a^2(0)S_e}{eS_{et}}; \quad \text{for } S_e > S_{et}, \quad (3.30)$$

$$S_{et} = \frac{\pi \rho c a^2(0) \Delta T_m}{g} \quad (3.31)$$

where S_{et} is the threshold value of S_e for track formation and e is Euler's number [124, 148].

In an attempt to address the analysis of defects induced by SHCIs in materials, Karlušić and Jakšić [124] provided an extension or alternative of the ATMS of Szenes. Contrary to SHIs, SHCIs deposit energy potential energy in a highly confined region of the surface. For this reason, their model proposed a semi-spherical thermal spike (TS) from a point-like source of excitation. In this model, the description of the TS is given by

$$\Delta T(r, t) = \frac{Q}{(a(t) \sqrt{\pi})^3} e^{-(r^2/a(t)^2)} \quad (3.32)$$

The conservation of energy (Eq.(3.33)) can be evaluated as

$$gE_p = \rho c \int_0^\infty \Delta T \cdot 4r^2 \pi dr = \rho c \int_0^\infty \frac{Q}{(a(t) \sqrt{\pi})^3} e^{-(r^2/a(t)^2)} \cdot 4\pi r^2 dr = \rho c Q \quad (3.33)$$

where E_p is the potential energy of the HCI and gE_p is the fraction of the initial HCI potential energy that forms the spherical thermal spike. As before three equations can be derived using Eqs.(3.32) and (3.33)

$$R_e^2 = a^2(0) \ln \left(\frac{E_p}{E_{pt}} \right); \quad \text{for } 1 \leq \frac{E_p}{E_{pt}} \leq e^{3/2} \quad (3.34)$$

$$R_e^2 = \frac{3a^2(0)}{2e} \left(\frac{E_p}{E_{pt}} \right)^{2/3}; \quad \text{for } \frac{E_p}{E_{pt}} \geq e^{3/2} \quad (3.35)$$

$$E_{pt} = \frac{\rho c (a(0) \sqrt{\pi})^3 \Delta T_m}{2g}. \quad (3.36)$$

Dividing the melting temperature by a factor of 2 in Eq.(3.36) incorporates the effect of the surface as a heat flux reflector included with the image source formalism [149]. In principle the ATSM parameters $a(0)$ and g can be determined analytically using Eqs.(3.34)-(3.36) in the same manner as in the cylindrical model, however, the main challenge in practice is that imaging techniques and conditions introduce systematic errors in the observed effective radius, R_e . The primary difference the energy transfer mechanisms arise from the fact that SHIs transfers all or most of its energy into the material whereas HCIs energy dissipation begins above the surface and can thus dissipated energy via various channels. For this reason, the efficiency factor is the main parameter that highlights the difference between SHI and HCI energy transfer mechanisms [124]. The definition of g in the case of HCI investigation is therefore modified such that:

$$g = g_1 \cdot g_2 \quad (3.37)$$

where g_1 represents the fraction of the initial HCI potential energy (or energy loss in the case of SHI) deposited in the material and g_2 represents the fraction of the deposited energy transformed into the energy of the thermal spike. For SHI, $g_1=1$ and $g=g_2$ while for HCIs, $g_1 \leq 1$ and g_2 is usually unknown [124].

3.3.4 The Defect Mediated Desorption Model

In the DMe model, localized surface defects are created from sputtering and desorption of surface atoms facilitated by the creation of self-trapped excitons (STEs) or self-trapped holes (STHs) in response to valence band electronic excitation [126–128, 150]. STEs are electron-hole pairs bound by the coulomb field within their own lattice distortion field. Electronic excitation of valence band electrons leading to sputtering has been observed mainly in insulators such as SiO_2 and Alkali halides and can be induced by different means including high energy electron irradiation in which case the mechanism is known as electron stimulated desorption, ESD, by ultraviolet photons i.e. photon stimulated desorption, PSD [151–153] and also by ion irradiation [129].

The interaction of HCIs with surfaces produces intense electronic excitation from above the surface and depending on the ion energy and surface properties also several monolayers beneath surface (see introduction to section 3.2.1). The electron emission associated with the transfer of potential energy upon SHCI impacts implies that corresponding holes are created in the valence band at or close to the Fermi edge (*cold holes*) and also deep in the valence band (*hot holes*) which subsequently trap electrons from the decaying HA and surrounding atoms leading to the formation of electron-hole pairs (see Fig. 3.6). Defect creation is enhanced by collisional damage emerging the kinetic energy of the HCIs. In addition, high energy Auger electrons produced from decay of inner-shells can produce defects in the lattice in a similar manner to the case of ESD [129]. Therefore in contrast to ESD by energetic electrons, defects created in insulating materials by HCI impacts are more spatially confined and are of number density. STEs and STHs decay into different colour centres.

For alkali halides, decay of STEs and STHs results in the production of H (an interstitial molecular halide ion) and F (an electron at an anion site) centres. Both centres diffuse independently towards the surface and subsequently

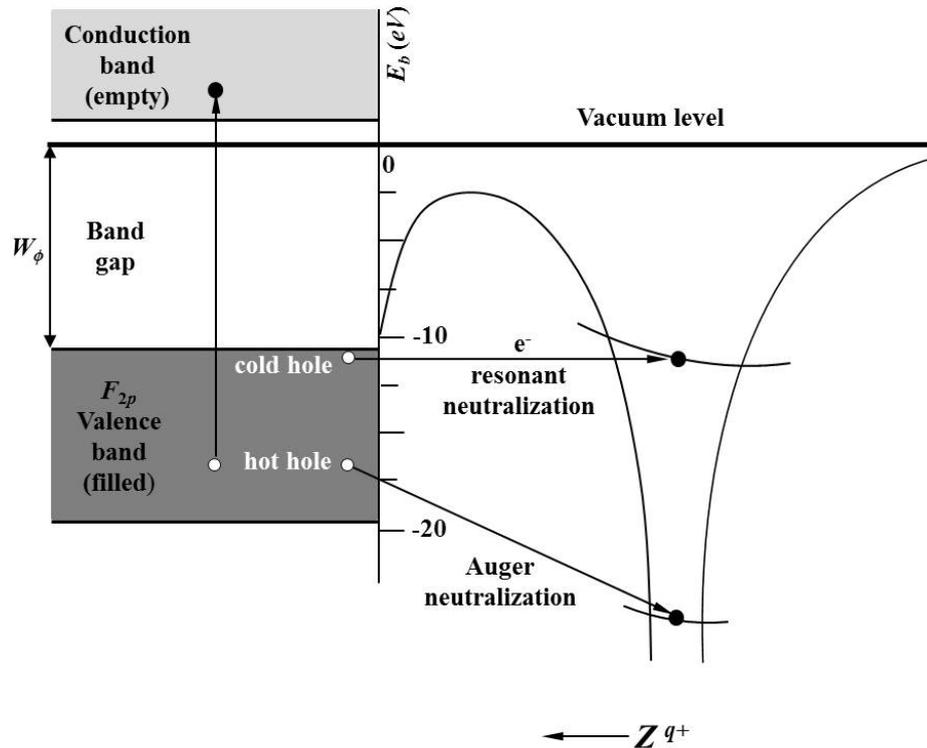


Figure 3.6: *Electronic transitions between surface and projectile HCI leading to formation of holes (via resonant neutralization) as well as electron-hole pairs (via Auger neutralization) [103]*

recombine with the surface. Recombination of an H centre with the surface results in the creation of a loosely bound halogen ad-atom which is desorbed via thermal evaporation. On the other hand, an F centre can recombine with the surface by neutralizing an alkali ion leading to its desorption. However, it has been shown [154] that the desorption process of a neutral alkali atom is energetically more feasible by recombination of $2p$ -excited F^* centre with the surface than with the F centre with low coordinated surface site e.g. terraces and edges being the preferential point for the desorption process.

In the case of HCIs, desorption and surface defect (pits) creation in KBr has been shown to be a consequence of a dense agglomeration of numerous F/F^*

centres within a localized region of several nm³ which is proportional to the ion charged state and the ion fluence [129]. However, in addition to the insulating property materials, within the DMe model, the enhancement of sputter yields with increasing charge state of the projectile HCI is only possible for materials with strong electron-phonon coupling which promotes localization of electronic excitation i.e. self-trapping and formation of STEs and/or STHs [103].

Chapter 4

Magnetism and Magnetic Materials

The phenomenon of magnetism has been observed mainly in naturally occurring solid state materials for a few thousand years. However, it was only until the formulation and development of quantum mechanics that magnetism could be adequately described and understood particularly for temperatures above 0 K for which classical mechanical descriptions are inadequate. The behaviour of electrons, atoms, ions, molecules and their interactions gives fundamental insights into the theory of magnetism. Magnetism is in general a vast field and for this reason, the present discussion is limited to topics relevant to the current investigation.

4.1 Atomic Magnetism

Consider an electron in orbit at radial distance r and angular velocity ω around an atomic nucleus of charge Z , e.g. as in the hydrogen atom. In Bohr's quantum theory, the orbital angular momentum P_l , is quantized in units of \hbar (which is related to Planck's constant h by $\hbar = h/2\pi$) and is described

using the *orbital* angular momentum quantum number l such that $P_l = \hbar l$. Therefore, the magnetic moment of the electron by orbital motion μ_l is given by [155]

$$\mu_l = - \left(\frac{\mu_0 e}{2m_e} \right) \hbar l = \mu_B l \quad (4.1)$$

where e, m_e are the charge and mass of the electron respectively. The Bohr magneton $\mu_B \approx 9.274 \times 10^{-24}$ [J·T⁻¹]. In addition to the orbital angular momentum, the *spin* angular momentum contributes to the magnetic moment of an electron in orbit around an atomic nucleus and is described using the spin angular momentum quantum number s

$$\mu_s = - \left(\frac{\mu_0 e}{m_e} \right) \hbar s = -2\mu_B s \quad (4.2)$$

where $s = \pm 1/2$. Therefore, the total magnetic moment by an electron in orbit around an atomic nucleus is given by [155]:

$$\mu = \mu_l + \mu_s = - (l + 2s) \mu_B = -g\mathbf{j}\mu_B \quad (4.3)$$

where the total angular momentum $\mathbf{j} = \mathbf{l} + \mathbf{s}$ and the g is the g-factor where $g=2$ for $l=0$. In the case of hydrogen, the nuclear charge is Ze and in this case, the non-relativistic Hamiltonian operator H of an electron in orbit around the nucleus in the absence of external fields is given by:

$$H_0 = \frac{\hat{\mathbf{p}}^2}{2m_e} - \frac{Ze^2}{r} \quad (4.4)$$

where the first and second terms are the kinetic and potential energy terms respectively. The eigen states are labelled with the integer quantum numbers n, l and m such that

$$\psi_{nlm}(r, \vartheta, \varphi) = R_{nl}(r) Y_l^m(\vartheta, \varphi) \quad (4.5)$$

where $n = 1, 2, 3, \dots$; for a given n , $l = 0, 1, 2, \dots, n - 1$ and for a given l , $m = -l, -l + 1, \dots, l - 1, l$. However, the energy depends only on n

$$E_n^0 = -\frac{mZ^2e^4}{2\hbar^2n^2} = -\frac{(Ze)^2}{2a_0n^2} \quad (4.6)$$

where $a_0 = \hbar^2 / (me^2) \approx 0.529 \cdot 10^{-8}$ cm is the Bohr radius. As a consequence of the spherical symmetry of the system, it follows that ψ_{nlm} are eigenstates of the *orbital* angular momentum and its z -component:

$$\mathbf{L}^2\psi_{nlm} = l(l+1)\hbar^2\psi_{nlm} \quad \text{and} \quad L^z\psi_{nlm} = m\hbar\psi_{nlm} \quad (4.7)$$

(\mathbf{L} is often defined to be dimensionless; then $\mathbf{L}^2\psi_{nlm} = l(l+1)\psi_{nlm}$ and $L^z\psi_{nlm} = m\psi_{nlm}$). The corresponding angular dependence is described by the spherical harmonics $Y_l^m(\vartheta, \varphi)$.

Most of the magnetic phenomena observed in solid state materials are strongly related to the magnetic behaviour of their constituent entities such as atoms, molecules, vacancies, crystal structure etc. For an atom with Z electrons, the Hamiltonian of the system is given by [155]

$$H_0 = \sum_{i=1}^Z \left(\frac{p_i^2}{2m_e} + V_i \right) \quad (4.8)$$

If an external magnetic field \mathbf{B} is present which is given by $\mathbf{B} = \nabla \times \mathbf{A}$ with \mathbf{A} being the magnetic vector potential which is chosen such that the magnetic field is homogenous within the atom and the Coulomb gauge $\nabla \cdot \mathbf{A} = 0$ is valid. In this situation, the magnetic vector potential can be written as $\mathbf{A}(r) = (\mathbf{A} \times r) / 2$. The corresponding kinetic energy amounts to:

$$E_{kin} = \frac{1}{2m} (p + eA(r))^2 = \frac{1}{2m} (p^2 + e(p \cdot A + A \cdot p) + e^2 A \cdot A) \quad (4.9)$$

Due to the Coulomb gauge one obtains: $p \cdot A = A \cdot p$ and as result, the Hamiltonian, H^i of the i^{th} electron is given by [155]

$$H^i = \frac{p_i^2}{2m} + V_i + \frac{e}{m} A \cdot p + \frac{e^2}{2m} A \cdot A \quad (4.10)$$

The last term can be written can be written as a function of the external magnetic field

$$\frac{e^2}{2m} A \cdot A = \frac{e^2}{2m} \left(\frac{1}{2} (B \times r) \right)^2 = \frac{e^2}{8m} (B \times r)^2 \quad (4.11)$$

The third term of the Hamiltonian can be written as

$$A \cdot p = \frac{1}{2} (B \times r) \cdot p = \frac{1}{2} (r \times p) \cdot B = \frac{1}{2} \hbar L \cdot B \quad (4.12)$$

where $\hbar L$ is the quantized orbital angular momentum. Therefore the Hamiltonian H^i of the i^{th} electron can be expressed as

$$H^i = \frac{p_i^2}{2m} + V_i + \mu_B L \cdot B + \frac{e^2}{8m} (B \times r_i)^2 \quad (4.13)$$

where the term $\mu_B L \cdot B$ gives rise to the Zeeman effect. The consideration of the electron *spin* angular momentum S results in an additional term $\mu_B g S \cdot B$ with $g \approx 2$ being the g -factor of an electron as before. Therefore the complete Hamiltonian is given by [155]

$$H = \sum_{i=1}^Z \left(\frac{p_i^2}{2m} + V_i \right) + \mu_B (L + gS) \cdot B + \frac{e^2}{8m} \sum_{i=1}^Z (B \times r_i)^2 = H_0 + H_1 \quad (4.14)$$

The part H_1 represents the modification of the electronic system due to the external magnetic field B and amounts to

$$H_1 = \mu_B (L + gS) \cdot B + \frac{e^2}{8m} \sum_{i=1}^Z (B \times r_i)^2 = H_1^{\text{para}} + H_1^{\text{dia}} \quad (4.15)$$

The first term H_1^{para} is known as the paramagnetic term and the second term H_1^{dia} is known as the diamagnetic term.

4.2 Magnetic Interactions

In real systems such as solid state materials and nanostructures, long range magnetic phenomena e.g. ferromagnetism develop as a direct result of interactions between magnetic moments in the system. Since magnetic moments can interact in different configurations, for the purposes of the present study we consider the magnetic dipole interaction and in comparison, the exchange interactions which are fundamentally quantum mechanical effects that arise as a consequence of the Coulomb interaction and Pauli's exclusion principle.

4.2.1 Magnetic Dipole Interaction

The energy of any two magnetic dipoles μ_1 and μ_2 separated by the vector r is given by:

$$E = \frac{\mu_0}{4\pi r^3} \left(\mu_1 \cdot \mu_2 - \frac{3}{r^2} (\mu_1 \cdot r)(\mu_2 \cdot r) \right) \quad (4.16)$$

and thus depends on their distance and relative orientations. In an arbitrary case where $\mu_1 = \mu_2 = 1\mu_B$ and $r = 2\text{\AA}$, to estimate the energy of the magnetic dipole interaction we assume $\mu_1 \uparrow \uparrow \mu_2$ and $\mu \uparrow \uparrow r$. Under these conditions, the energy given by

$$E = \frac{\mu_0 \mu_B^2}{2\pi r^3} = 2.1 \cdot 10^{-24} J \quad (4.17)$$

Since the corresponding system temperature ($E = kT$) is well below 1 K, it is clear that energy of the magnetic dipole interaction is too low to induce co-operative ferromagnetism.

4.2.2 Exchange Interactions

The spontaneous order of magnetic moments is a characteristic signature of so called cooperative or collective magnetism and is typically observed in ferromagnetic, ferrimagnetic and antiferromagnetic materials. Such ordering takes place at temperatures below a critical temperature T^* which is material specific. In the case of ferro and ferrimagnetic materials, the critical temperature $T^* = T_C$ is known as the *Curie* Temperature, while in antiferromagnetic materials, $T^* = T_N$ and known as *Neel* temperature. In all solid state magnetic materials, the spontaneous magnetization is destroyed (vanishes) at temperatures above T^* . Exchange interactions were discovered independently by *Dirac* and *Heisenberg* in 1926 to be primarily responsible for long range magnetic ordering (cooperative magnetism) in solid state materials [156]. The matrix elements of the exchange interaction constructed with completely antisymmetric wavefunctions, contain terms which are classically not understandable and correspond to an exchange of the indices of the identical particles (Fermions). Nonetheless, as a precondition for collective magnetism in solid state materials, there must exist *permanent* magnetic moments in the material. In real systems *direct* and *indirect* exchange interactions are possible.

Direct Exchange

Consider a model consisting of only two electrons with position vectors r_1 and r_2 where the total wavefunction of the system is equivalent to the product

of single electron states $\psi_a(r_1)$ and $\psi_b(r_2)$. Electrons are fermions therefore the system wavefunction must be antisymmetric as a consequence of Pauli's exclusion principle on fermions. The electrons in the considered model are indistinguishable therefore the wavefunction squared must be invariant for the exchange of both electrons. In addition, due to spin of the electrons two possibilities arise: a symmetric spatial part ψ in combination with an antisymmetric spin part χ or an antisymmetric part in combination with a symmetric spin part. The first case presents a singlet state with $S_{total} = 0$ while the second case presents a triplet state with $S_{total} = 1$. The corresponding total wave functions are given by:

$$\psi_S = \frac{1}{\sqrt{2}} [\psi_a(r_1)\psi_b(r_2) + \psi_a(r_2)\psi_b(r_1)] \cdot \chi_S \quad (4.18)$$

$$\psi_T = \frac{1}{\sqrt{2}} [\psi_a(r_1)\psi_b(r_2) - \psi_a(r_2)\psi_b(r_1)] \cdot \chi_T \quad (4.19)$$

The energies of the singlet and triplet states amount to:

$$E_S = \int \psi_S^* H \psi_S dV_1 dV_2 \quad (4.20)$$

$$E_T = \int \psi_T^* H \psi_T dV_1 dV_2 \quad (4.21)$$

taking into account normalized spin components of the singlet and triplet wavefunctions, i.e.

$$s^2 = (S_1 + S_2)^2 = S_1^2 + S_2^2 + 2S_1 \cdot S_2 \quad (4.22)$$

we thus obtain:

$$S_1 \cdot S_2 = \frac{1}{2} S_{total} (S_{total} + 1) - \frac{1}{2} S_1 (S_1 + 1) - \frac{1}{2} S_2 (S_2 + 1) \quad (4.23)$$

$$= \frac{1}{2} S_{total} (S_{total} + 1) - \frac{3}{4} \quad \text{due to } S_1 = S_2 = \frac{1}{2} \quad (4.24)$$

$$= \begin{cases} -\frac{3}{4} & \text{for } S_{total} = 0 \quad (\text{singlet}) \\ +\frac{1}{4} & \text{for } S_{total} = 1 \quad (\text{triplet}) \end{cases} \quad (4.25)$$

The effective Hamiltonian can be expressed as:

$$H = \frac{1}{4} (E_S + 3E_T) - (E_S - E_T) S_1 \cdot S_2 \quad (4.26)$$

The first term is constant and often included in other energy contributions. The second term is spin dependent and more important concerning ferromagnetic properties. The exchange constant or exchange integral J is given by:

$$J = \frac{E_S - E_T}{2} = \int \psi_a^*(r_1) \psi_b^*(r_2) H \psi_a(r_2) \psi_b(r_1) dV_1 dV_2 \quad (4.27)$$

Then the spin dependent term in the effective Hamiltonian can be written as:

$$H_{spin} = -2JS_1 \cdot S_2 \quad (4.28)$$

If the exchange integral J is positive then $E_S > E_T$, i.e. the triplet state with $S_{total} = 1$ is energetically favored. If the exchange integral J is negative, then $E_S < E_T$, i.e. singlet state with $S_{total} = 0$ is energetically favoured. In the case of many electron atoms in magnetic systems, the Schrödinger equation cannot be solved without assumptions. The most important part of such an interaction like the exchange interaction mostly apply between neighbouring atoms. This consideration within the Heisenberg model leads to a term in the Hamiltonian of the form:

$$H = - \sum_{ij} J_{ij} S_i \cdot S_j \quad (4.29)$$

with J_{ij} being the exchange constant between spin i and spin j . The factor 2 is included in the double counting within the sum. Often a good approximation is given by:

$$J_{ij} = \begin{cases} J & \text{for nearest neighbor spins} \\ 0 & \text{otherwise} \end{cases} \quad (4.30)$$

Generally, J is positive for electrons at the same atom whereas it is often negative if both electrons belong to different atoms.

Indirect Exchange

In real systems, i.e. magnetic materials, magnetic nanostructures etc., the separation between two magnetic moments is generally large in comparison to average inter-electron distance presented in the *direct* exchange mechanism. For this reason, *direct* exchange is frequently not acceptable as a coupling mechanism in magnetic materials. There are a number of *indirect* exchange mechanisms which within the framework of second-order perturbation theory lead to an effective Hamiltonian of the Heisenberg type. They are different from *direct* exchange because the *direct* exchange is a result of first-order perturbation theory. Nonetheless, the concept of *indirect* exchange is not uniquely defined, for this reason, three different types of *indirect* exchange mechanisms are briefly discussed below [157].

- **Superexchange:** This type of indirect exchange occurs predominantly in ionic solids. The exchange interaction between non-neighboring magnetic ions is mediated by means of a non-magnetic ion which is located in-between. The distance between the magnetic ions is too large that a direct exchange can take place.

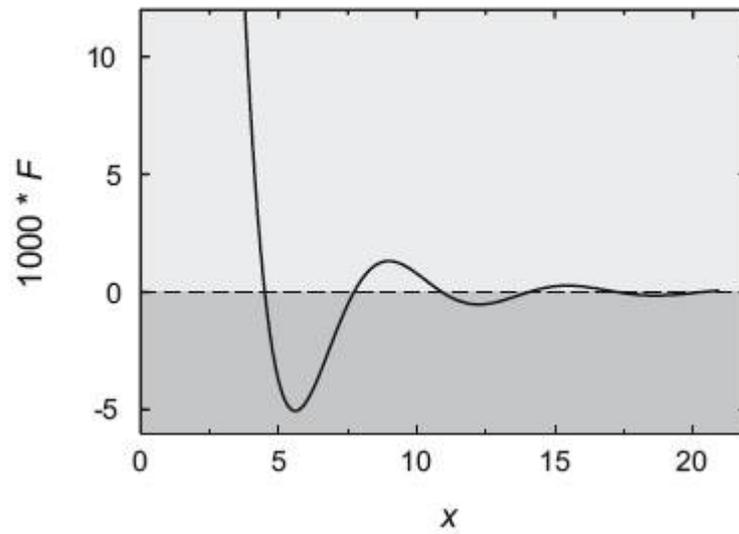


Figure 4.1: Graphical representation of the function $F(x)$ defined in Eq.4.31 using $x=2k_F r$. Positive values lead to a ferromagnetic coupling whereas negative values lead to an anti-ferromagnetic arrangement [157].

- **RKKY exchange interaction:** The RKKY exchange (Ruderman, Kittel, Kasuya, Yosida) occurs typically in metals with localized magnetic moments. The exchange is mediated via the conduction electrons ("indirect") where the coupling is characterized by a distance dependent exchange integral $J_{RKKY}(r) \propto F(2k_F r)$ with

$$F(x) = \frac{\sin(x) - x \cos x}{x^4}. \quad (4.31)$$

This type of exchange coupling is long range and anisotropic which often results in complicated spin arrangements. In addition, the oscillating behaviour predictates a type of coupling (ferro- or anti-ferromagnetic nature) that is a function of the distance between the magnetic moments (see Fig.4.1).

- **Double exchange:** This type of exchange interaction occurs in some oxides where the magnetic ions exhibit mixed valencies, i.e. different oxidation

states which results in ferromagnetic arrangement, eg. magnetite (Fe_3O_4) which includes Fe^{2+} as well as Fe^{3+} ions.

4.3 Classification of Magnetic Materials

The magnetic response of solid state materials can be classified into three different groups based on their magnetic susceptibility χ where

$$\chi = \frac{M}{H} \quad (4.32)$$

and M represents the magnetization parallel to an externally applied magnetic field H . The magnetic moment of a free atom has three principal sources: the intrinsic spin of the electron, their orbital angular momentum about the nucleus and the change in orbital angular momentum induced by an externally applied magnetic field. The first two effects give paramagnetic contributions to the magnetization while the third effect gives a diamagnetic contribution [158].

- **Diamagnetism:** Diamagnetism is purely an induction effect. An external magnetic field H induces magnetic dipoles which are oriented antiparallel with respect to the exciting field as a consequence of Lenz's rule. Therefore, the diamagnetic susceptibility is negative:

$$\chi^{dia} = \text{const.} < 0 \quad (4.33)$$

Examples of diamagnetic materials are; nearly all organic substances, metals (eg. Hg) and superconductors (below the critical temperature). Below their critical temperature, superconductors are ideal diamagnets, i.e. $\chi^{dia} = -1$ (Meißner-Ochsenfeld effect).

- **Paramagnetism:** Paramagnetic materials are characterized by a positive

magnetic susceptibility, i.e.

$$\chi^{Para} = \chi^{Para}(T) > 0 \quad (4.34)$$

A crucial precondition for the appearance of paramagnetism is the existence of permanent magnetic dipoles. These are oriented along the direction of the external magnetic field H . The magnetic moments can be localized or of itinerant nature. Electronic paramagnetism is found in numerous systems including

- **Localized Moments** in atoms, molecules and lattice defects possessing an odd number of electrons. In such systems, the total spin of the system cannot be zero. Such materials exhibit the so-called Langevin paramagnetism. The susceptibility χ^{Langevin} depends in the temperature. At high temperatures the Curie law is valid

$$\chi^{\text{Langevin}}(T) = \frac{c}{T} \quad (4.35)$$

- **Itinerant moments:** Nearly free electrons in the valence band carry a permanent magnetic moment of $1\mu_B$. This type of paramagnetism is called Pauli paramagnetism. The corresponding susceptibility is nearly independent of temperature:

$$\frac{\partial \chi^{\text{Pauli}}}{\partial T} \approx 0 \quad (4.36)$$

The magnitudes of these susceptibilities are very different:

$$\chi^{\text{Pauli}} \ll \chi^{\text{Langevin}} \quad (4.37)$$

- **Collective Magnetism:** The susceptibility exhibits a significantly more complicated functionality of diverse parameters compared to dia- and paramagnetism:

$$\chi^{\text{coll}} = \chi^{\text{coll}}(T, \mathbf{H}, \text{"history"}) \quad (4.38)$$

The collective magnetism is a result of an exchange interaction between permanent magnetic dipoles. Materials that exhibit collective magnetism undergo spontaneous magnetization in the absence of an external magnetic field at temperatures below a critical temperature T^* which is specific to the material. In addition, magnetic moments in some materials can also be localized. Collective magnetism can be divided into three subclasses:

- **Ferromagnetism:** The critical temperature associated with spontaneous magnetization T^* is called the *Curie temperature* T_C . At the temperatures between zero and T_C i.e. ($0 < T < T_C$) the magnetic moments are aligned in preferential orientation due to thermal effects however, at $T = 0$, all the magnetic moments are aligned parallel to each other. Ferromagnetic magnetic materials that exhibit itinerant magnetic moments are referred to as band or itinerant ferromagnets. Examples of these materials are Cobalt (Co), Nickel (Ni) and Iron (Fe).
- **Ferrimagnetism:** In ferrimagnetic materials, the lattice consists of two ferromagnetic sublattices A and B exhibiting different magnetization (i.e. $M_A \neq M_B$) such that the effective magnetization M is non zero below the Curie temperature (i.e. $M = M_A + M_B \neq 0$). Cubic spinel ferrites such as NiFe_2O_4 and CoFe_2O_4 are examples of materials that exhibit this interaction.
- **Antiferromagnetism:** Antiferromagnetism is a special case of ferrimagnetism where the critical temperature T^* is called the *Néel temperature* T_N and is characterized by $|M_A| = |M_B| \neq 0$ for temperatures below T_N , i.e. ($T < T_N$) and also $M_A = -M_B$. There-

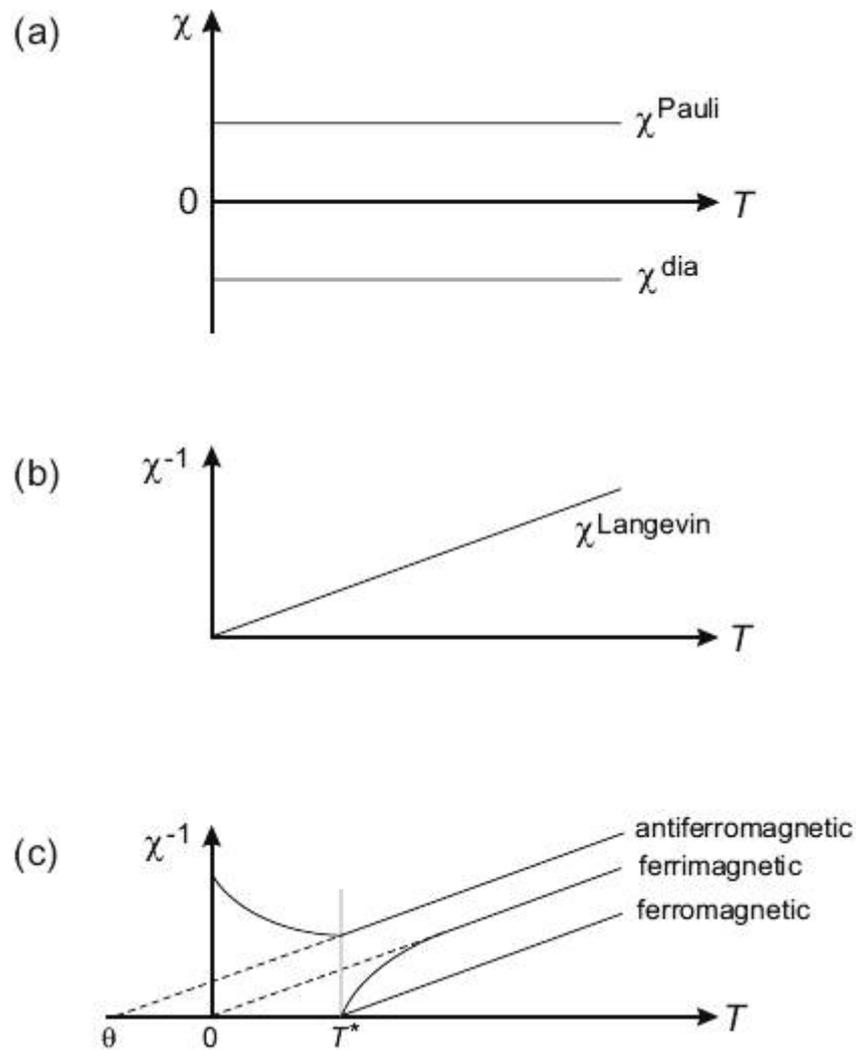


Figure 4.2: Temperature dependence of the magnetic susceptibility χ and inverse magnetic susceptibility χ^{-1} in the case of (a) diamagnetism and Pauli paramagnetism, (b) Langevin paramagnetism, (c) ferromagnetism, antiferromagnetism and ferrimagnetism with T^* being the critical temperature and θ the paramagnetic Curie temperature

fore, the total magnetization vanishes, i.e. $M = M_A + M_B = 0$. Above the critical temperature, collective magnetism transforms into paramagnetism corresponding characteristic discussed above. A summary the behaviour of different magnetic materials is shown in Fig. 4.2 in terms their magnetic susceptibility and its dependence on temperature. An example of this phenomenon is seen in MnO_2 for which M along the [111] is equal and opposite.

4.4 Magnetism in Carbon Systems

Along with several special properties already discovered and explored in carbon such as the existence of high carrier mobilities and superior mechanical strength, the prospect of long range magnetic order in carbon materials provides a platform for fabricating devices that exploit both the electron charge as well as its spin. The miniaturisation of electronic devices as an inevitable demand of modern technology poses a technical challenge when dimensions approaches atomic scales as proposed by the famous *Moore's* law. At such length scales, the significance of quantum mechanical phenomena such as quantum entanglement demands that a new generation of devices based fundamentally on different physical principles be envisaged.

Spintronics (i.e. the science of fabricating devices that exploit the electron spin as the primary principle of operation) is facilitated by the ability to control electron spin dynamics using magnetic fields and electromagnetic radiation e.g. radio, optical, UV and microwave frequencies. In addition, materials for spintronics should incorporate and/or transport spins with high integrity and coherence at room temperature. However, since most carbon materials are naturally diamagnetic and paramagnetic, the systematic fabrication of carbon materials that exhibit long range order is far from trivial.

Before the discovery of ferromagnetism in the open shell radical *p*-NPNN [159, 160], the [TDAE]⁺C₆₀ charge-transfer salt [9] with Curie temperatures 0.6 K and 16 K respectively as well as in metal-free polymerized fullerenes at room temperature [161, 162], cooperative or collective magnetism has been primarily associated with exchange interactions in metals consisting of *3d* and *4f* atomic orbitals, eg. Fe, Ni and Co. Nonetheless, the lack of reproducibility in these earlier observations of ferromagnetism as well as inadequate analysis of metallic impurity contributions resulted in prolonged skepticism on the notion of organic ferromagnetism in the scientific community.

Although no complete theory has been formulated to describe the general process by which spontaneous long range magnetic order occurs in carbon materials at room temperature, several theories and scenarios have been proposed in an effort to provide relevant insight from an atomic level using first principles. In addition, experimental investigations have confirmed the possibility of inducing room temperature magnetic ordering in various 0D, 1D, 2D and 3D carbon materials including graphite, graphene, graphone, carbon nanotubes and carbon spheres.

Nonetheless, although numerous investigations on the physical properties of diamond have been carried out since the 1950s, very few experimental studies geared towards inducing long range magnetic order in diamond have been reported. Talapatra et al. [38] carried out magnetism studies of nitrogen irradiation of nanodiamonds. Theoretical investigations performed using spin-polarized density functional theory (DFT) based on the generalized gradient approximation (GGA) of Perdew and Wang (PW91) functional [163] have shown that when a single vacancy is created in diamond, the structure relaxes such that the nearest neighbour atoms of the vacancy are displaced towards each other with a displacement of 0.14 Å [28] at maximum from their equilibrium positions (i.e. the uncoordinated atoms of the vacancy undergo a Jahn

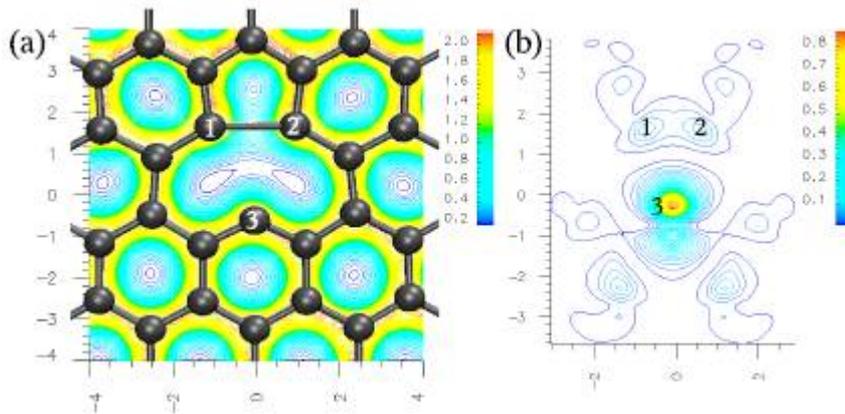


Figure 4.3: (a) Structure, charge density ($e/\text{\AA}^3$), and (b) spin density ($e/\text{\AA}^3$) of the graphite vacancy. Density plots are slices in the graphene plane [37].

Teller distortion).

Vacancy creation in diamond produces four uncoordinated carbon atoms each with dangling bonds that still exhibit sp^3 hybridization. The four sp^3 hybridized dangling bonds give rise to four energy levels, three of which lie near Fermi energy. The fourth energy level lies below the Fermi energy and is fully occupied by two electrons from the dangling bonds. The remaining three orbitals are split with splitting energies of 0.9 eV between polarized levels for spin up and spin down electrons. The remaining two electrons then occupy the spin-up energy levels giving rise to a net magnetic moment of $2 \mu_B$ where the non-magnetic state is 0.24 eV higher than the ground state [28].

In comparison, single vacancy production in a graphene sheet leaves three sp^2 hybridized dangling bonds on each of the three neighbouring atoms. By virtue of a Jahn Teller distortion, two of the nearest neighbour atoms to the vacancy form a weak covalent bond resulting in a pentagon-like structure (see Fig. 4.3) in which the final atom is displaced 0.18 \AA out of the surface [164]. Formation of the pentagon results in the saturation of two of the three dangling bonds. The remaining unsaturated bond results in a ground magnetic moment of $1.04 \mu_B$ where the difference between magnetic and non-magnetic states is

about 0.1 eV [37], which is comparable to the energy of interlayer van der Waals interaction.

Various defect configurations and topologies up to 3D have been investigated theoretically with respect to their effect on the magnetic response in carbon systems. Using full potential, all electron, spin polarized electronic structure *ab initio* calculations based on DFT it has been shown that the existence of a 3D network of single vacancies in the graphite lattice can also induce long range magnetic order at room temperature. However, the geometry of the supercell directly affects the strength of the predicted magnetic moment. It is found that the 3 x 3 x 1 super lattice exhibits the strongest magnetic moment with values of $2.06 \mu_B$ and $1.76 \mu_B$ in relaxed and non-relaxed energy states respectively compared to for example the more dilute 4 x 4 x 1 super cell which exhibits a 'relaxed' magnetic moment of $1.21 \mu_B$ [36].

The presence of interstitial carbon point defects as well as adatoms in the diamond graphite or graphene structure have been investigated using density functional theory. Due to the relatively large interlayer spacing between nearest graphitic layers ($\approx 1.35 \text{ \AA}$), carbon interstitials can be qualitatively be treated as adatoms on the graphene layer. Although the presence of atoms in carbon exhibits a magnetic moment, the low theoretical barrier of 0.45 eV [165] of adatom migration may result in high adatom mobility on graphene and graphite. In comparison, experimental estimates for interstitial diffusion suggest an energy barrier of 0.1 eV [166]. Interstitials are therefore likely to recombine with vacancies even at room temperature thus reducing their contribution to observed magnetic ordering in carbon systems.

The effect of the local bonding environment on long range magnetic ordering has been experimentally demonstrated by ion irradiation of graphite and diamond [10,38]. Nitrogen is by far the most common impurity in all types diamond and most carbon systems. By considering the most stable and en-

ergetically favourable lattice sites for the incorporation of nitrogen impurities, it has been shown using DFT methods that nitrogen adsorbed on the surface of graphite or a carbon nanotube exhibits finite magnetic moments [?]. In addition, Zhang *et al.* [28] conducted a DFT study to show that the presence of a nitrogen impurity at various lattice sites next to a single vacancy can significantly alter the spin configuration of the graphitic system. This is in contrast to the presence of nitrogen in defect free graphite where it is readily incorporated in the graphitic system without affecting its sp^2 bonding character.

Another common impurity in most allotropes of carbon is hydrogen. Hydrogen readily bonds to most carbon surfaces when exposed in air terminating the carbon dangling bonds. In the case of diamond, termination of surface dangling bonds by atomic hydrogen stabilizes the sp^3 carbon phase thus preventing diamond to graphite transformation. The incorporation of hydrogen impurities into bulk carbon materials at desired concentrations and locations is not trivial and is best carried out using ion implantation. Initially considered to be a controversial result, Esquinazi *et al.* [10] demonstrated that proton irradiation of highly oriented pyrolytic graphite (HOPG) at ~ 2 MeV energy and fluences below 10^{18} cm^{-2} results in the formation of magnetically ordered (ferromagnetic or ferrimagnetic) domains that are observable using techniques such as magnetic force microscopy (MFM) and the superconducting quantum interference device (SQUID).

The surface of most bulk materials, typically ~ 1 μm , contains large fractions of hydrogen. However, this is not sufficient to render the respective materials as ferro/ferri magnetic materials. Therefore, controlled creation of point defects by e.g. ion irradiation is pivotal in the observation of room temperature magnetic ordering in carbon materials. These results inspired further similar [12,17,167] and more detailed [31,168] experiments involving ion irradiation of carbon materials and other organic materials [13]. It has been shown

experimentally that defect mediated magnetic ordering in carbon materials can be triggered by ion irradiation using different ion species e.g. nitrogen [31,38] and carbon [15,168] even at low energies \sim keV. Therefore, the formation of magnetically ordered domains in carbon materials is independent of the ion species used for implantation or its impact energy [31].

In order to discuss and provide quantitative estimates for magnetism induced by ion implantation in carbon materials, it is imperative to quantify the content of magnetic impurities present in any sample prior to irradiation. The most accurate and appropriate techniques of necessary and adequate resolution are nuclear techniques including particle induced x-ray emission (PIXE), Rutherford backscattering spectroscopy (RBS) and neutron activation analysis (NAA). Several studies have shown that most 'pure' HOPG graphite samples contains magnetic impurities below $1 \mu\text{g/g}$. Although much theoretical work has been carried out to provide insight into the origin of room temperature magnetic ordering in carbon materials and possibly pave way towards optimization of the effect, the choice of experimental parameters necessary to trigger the effect in an optimal manner appear to be limited within a 'narrow' range and are primarily responsible either enhancing or destroying the effect.

Fig 4.4 shows an example of the net magnetic response of HOPG (mounted on a Si substrate) acquired using a SQUID device following 2 MeV proton irradiation i.e. after subtraction of the magnetic response from the virgin sample (a) represents the net magnetic response as function of the temperature (M vs T) at a constant applied magnetic field of 1 T and (b) represents the net magnetic response as function of the applied magnetic field cycled between $[-1,1]$ T at two different temperatures *viz.* 5 K and 300 K. The irradiation consisted of three 'broad' proton spots of 0.8 mm diameter that are 0.7 mm with a total charge of $150 \mu\text{C}$ per spot (i.e. total accumulated charge is $450 \mu\text{C}$) at a proton current of 100 nA. The inset in (b) shows the net magnetic

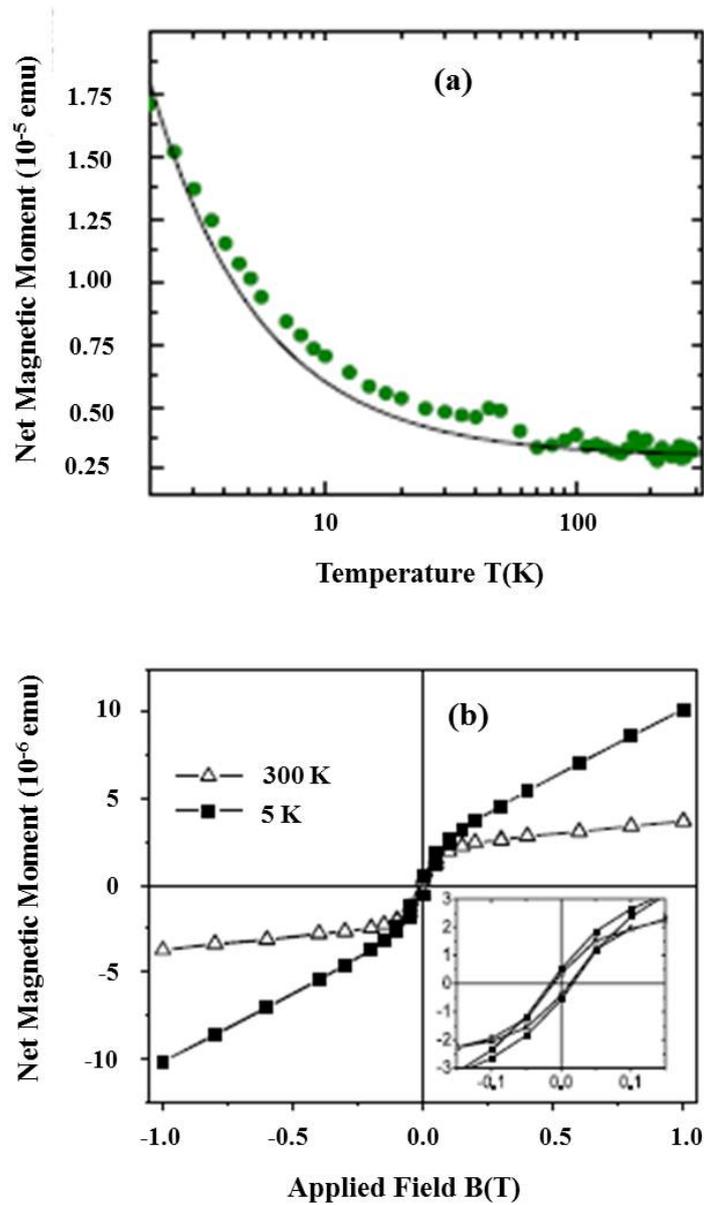


Figure 4.4: Net magnetic moment following irradiation of HOPG (on Si substrate) at a constant applied magnetic field of 1 T using a broad proton beam (total accumulated charge $450 \mu\text{C}$ at 100 nA) of 2 MeV energy. (a) Net magnetic moment vs temperature at 1 T. The continuous line is the function $3 \times 10^{-5}[\text{emu K}]/T + 3 \times 10^{-6}[\text{emu}]$. (b) Hysteresis loop; net magnetic moment of the irradiated HOPG sample as a function of the applied magnetic field cycled between [-1, 1] T at 5 K and 300 K. The inset shows the hysteresis loop in a narrow range [-0.15, 0.15] T for clarity [26].

contributions in a smaller field range for clarity [26].

The M vs T curve in Fig. 4.4(a) represents a paramagnetic contribution superimposed on a constant ferromagnetic contribution. The paramagnetic behaviour roughly follows the Curie law $3 \times 10^{-5}/T$ emu and the constant ferromagnetic contribution is of the order of 3×10^{-6} emu, i.e. $m(T, B > B_s) \simeq \frac{3 \times 10^{-5}}{T} + 3 \times 10^{-6}$, where B_s is the minimum saturation field for the ferromagnetic part [26]. The observed increase in the net magnetic moment at room temperature in Fig. 4.4(b) is due the presence of ferromagnetism in the HOPG sample induced by irradiation with a Curie point above room temperature and is superimposed on a paramagnetic contribution which constitutes $\sim 25\%$ at 300 K and 1 T [26].

The Curie law emerges when the main variable of the Brillouin function $B_J(x)$ with $x = gJ\mu_B B/k_B T$ takes on values $x \ll 1$ in which case only the first term of the Brillouin function remains. However, assuming for simplicity the product of the Landé factor g and the total angular momentum J , $gJ \sim 1$, at an applied magnetic field of 1 T and temperatures [5, 300] K used in Fig. 4.4, x reaches relatively high values, i.e. $0.13 \leq x \leq 2.2 \times 10^{-3}$ [26]. These relatively large values together with the assumption of a strictly temperature independent ferromagnetic contribution could be responsible for the slight deviation from the Curie law observed in Fig. 4.4(a).

Fig. 4.5(a) shows M vs T curves acquired in the second pure HOPG sample at constant applied magnetic field of 1 T. The sample is irradiated using a 2.25 MeV proton micro beam of diameter $\simeq 2 \mu\text{m}$ and current of 700 pA. The total number of spots irradiated is 3×10^4 (first 10^4 spots corresponding to a total charge of $11.6 \mu\text{C}$ then later 2×10^4 corresponding to a total charge of $34.8 \mu\text{C}$) corresponding to an ion fluence of $0.37 \text{ nC}/\mu\text{m}^2 = 2.3 \times 10^{17} \text{ H}^+/\text{cm}^2$. The dependence of the net magnetic moment on temperature shows no obvious Curie-like contribution after irradiation. However, as shown in Fig.4.5(b), part

of the magnetic response of the irradiated spots is due ferromagnetism where each spot contributes $\sim 2 \times 10^{-10}$ emu to the total ferromagnetic response of the sample [26].

Figs.4.4 and 4.5 illustrate the influence of ion irradiation experimental parameters on the magnetic response of HOPG. The strongest magnetic ferromagnetic signals in the discussed investigations are obtained using *micro* beams at currents < 1 nA and fluences < 1 nC/ μm^2 (6.25×10^{17} cm $^{-2}$). Due to heating effects, large proton currents and high fluences can decrease the extent of magnetic ordering in carbon. However, for a very low density of regions irradiated using *micro* beams, the reliability of both SQUID and magnetic force microscopy (MFM) may be limited especially at zero field where the remanence can be significantly reduced. Therefore, it is imperative to consider reliable sensitivity limits for instruments when selecting ion irradiation parameters.

Fig. 4.6 shows examples of AFM/MFM images over $(20 \times 20) \mu\text{m}^2$ regions on HOPG with a spot irradiated parallel to the *c*-axis using a 2.25 MeV proton *micro* beam of 1-2 μm diameter. The micro irradiation creates radiation damage in the confined spot resulting in upswelling of the surface. The scale of the upswelling is ~ 5 nm (see Fig 4.6(b) top image) and is directly proportional to the ion fluence. The phase shift plot i.e. bottom image of Fig. 4.6(b) illustrates the magnetic response in the irradiated spot shown in (a). The irradiated spot exhibits positive phase shifts from cantilever resonance which is indicative of a repulsive magnetic force between the cantilever and the irradiated spot [17]. Following the application of a magnetic field (in both parallel and anti parallel directions to the *c*-axis) to the irradiated HOPG sample, line scans acquired across the irradiated spot shows positive phase shifts for all magnetization directions with only a variation in the scale of the phase shift. These results confirm and support the existence of magnetically ordered domain the irradiated spot as observed using the SQUID technique where the

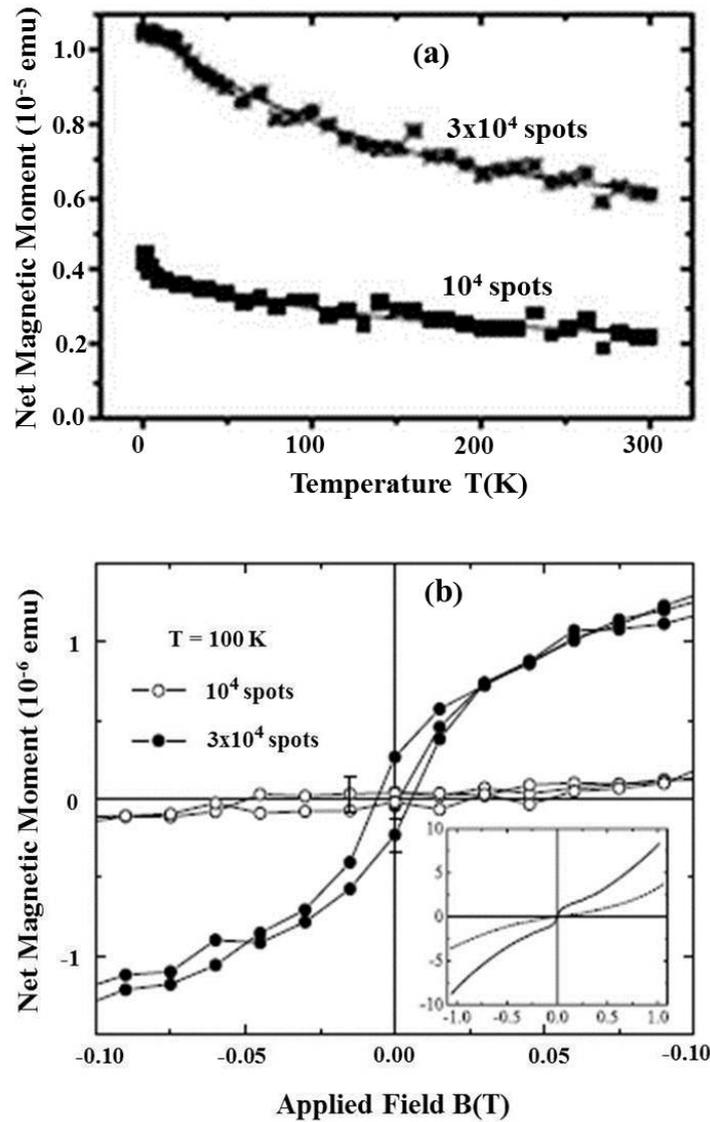


Figure 4.5: Net magnetic moment of HOPG following two sets of irradiations using a proton micro beam of $2 \mu\text{m}$ diameter and energy 2.25 MeV at 100 K and an applied magnetic field of 1 T . First with 10^4 spots with a total charge $11.6 \mu\text{C}$ at 700 pA and the second adding similar 2×10^4 spots with total charge $34.8 \mu\text{C}$ at 700 pA . (a) M vs T curves showing the net magnetic moment after 10^4 and 2×10^4 irradiated spots. The continuous lines are fits to the function $m_0 + m_1 \exp(-T/T_0)$ with parameters $m_0 = 2.2(5.6) \times 10^{-6} \text{ emu}$, $m_1 = 1.9(5.07) \times 10^{-6} \text{ emu}$ and $T_0 = 116(140) \text{ K}$ for the first(second) irradiated sample. (b) The hysteresis loops corresponding to data the in (a). The inset shows the hysteresis loops in a broader field range for the first (dotted line) and second irradiation (continuous line) [26].

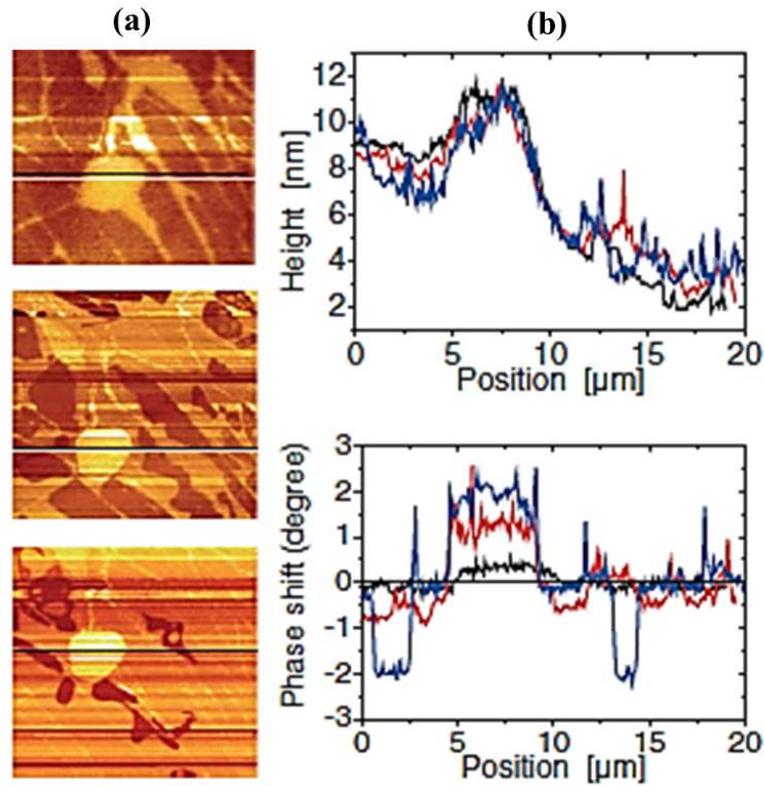


Figure 4.6: (a) Magnetic force gradient images (20×20) μm^2 of a spot and its surroundings irradiated with $0.115 \text{ nC}\mu\text{m}^{-2}$ (current $I=171 \text{ pA}$). The images were taken, from top to bottom, before field application, after applying a field of $\sim 0.1 \text{ T}$ in the $+z$ direction (normal to the surface), and in the $-z$ direction. The tip-sample distance was 50 nm ; (b) the corresponding height (top) and phase shift (bottom) obtained at the linescans (black line (a)) [17].

field applied across the sample for MFM imaging is less than the coercivity of the magnetic domain in the irradiated spot.

Most successful experiments of defect induced magnetic ordering in carbon have been carried out using proton beams although other projectile species such as N and C have been used successfully while He implantation resulted in no "observable" net magnetic ordering at room temperature. In addition to single and 3D networks of vacancies discussed above, the effect of the implanted

ions requires thorough consideration in searching for the origin of magnetic ordering in carbon materials. By considering stable and energetically favourable lattice sites of hydrogen in graphite, the effect of hydrogen on magnetic properties of proton irradiated graphite has been investigated using spin polarized DFT methods [37, 169]. Lehtinen *et al* [37]., showed that although vacancies exhibit a net magnetic moment at room temperature, the high mobility of carbon interstitials implies that they can annihilate with vacancies at room temperature thus reducing their contribution to the total magnetic ordering in graphite. However, in investigating several prolific defects induced by proton irradiation of graphite, two energetically favourable configurations of hydrogen in irradiated graphite that exhibit stable magnetic moments at room temperature were discovered (see Fig. 4.7).

When hydrogen encounters an empty (unoccupied) vacancy in a carbon material, e.g. graphite (or diamond), it will saturate the dangling bond by the formation of a covalent bond. In the case of graphite (or graphene), the hydrogen is bonded at a height of 1.25 \AA above the plane with an adsorption energy of 4.36 eV. This configuration however, is non magnetic. Nonetheless, if a second hydrogen atom encounters a vacancy in which one carbon dangling bond is saturated by a hydrogen atom, the hydrogen atom will saturate another carbon dangling bond 0.89 \AA beneath the graphene plane forming a covalent bond with an adsorption energy of 3.2 eV (Fig. 4.7(a)). This configuration has a magnetic moment of $1.2 \mu_B$ localized on the remaining sp^2 dangling bond [37]. If a third hydrogen atom bonds to and hence saturating the remaining sp^2 dangling bond, the magnetism of the vacancy is destroyed. The adsorption energy of a third hydrogen atom to the remaining sp^2 dangling bond is 4.0 eV. However, steric hindrance sets an energy barrier that reduces the probability of this configuration [37].

The second stable configuration involves the following; if a hydrogen atom

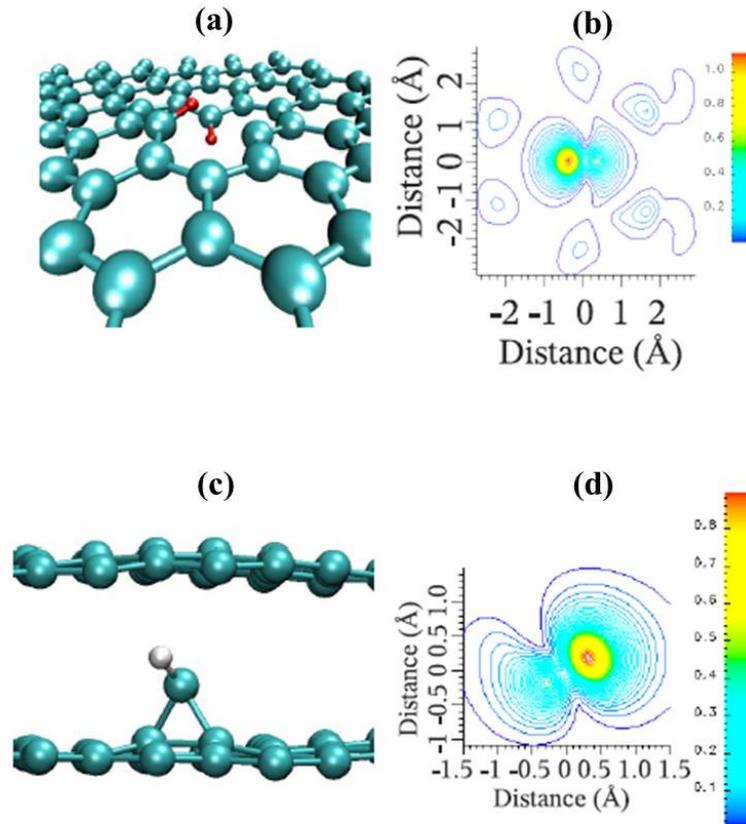


Figure 4.7: (a) Structure and (b) spin density ($\mu_B/\text{\AA}^2$) of a vacancy surrounded by two hydrogen atoms in graphite (graphene). (c) Structure and (d) spin density ($\mu_B/\text{\AA}^2$) of a C-H group adsorbed between two layers of graphene [37].

encounters a carbon atom that has is adsorbed between two graphene sheets, it will saturate the dangling bond forming a C-H bond that is tilted with respect to the c -axis due to interaction with the second graphene layer. The structural complex has an adsorption energy of 3.8 eV and results in a magnetic moment of $0.9 \mu_B$ [37]. These two configurations provide insight into the mechanisms by which localized magnetic moments can be induced in carbon materials at room temperature. In addition, room temperature stability of the magnetic moments requires that the ground state energy of the magnetic state should be sufficiently higher than the non-magnetic state in order to survive thermal fluctuations. Since no complete theory of magnetic ordering in carbon

materials has been achieved, these results highlight the possible influence of hydrogen in observed magnetic ordering in carbon systems.

A key experimental study of magnetism in carbon was conducted by Ohldag *et al.* [29] using X-ray magnetic circular dichroism (XMCD) to analyze the magnetic response of carbon thin films following proton irradiation. Two different types of carbon thin films were prepared by pulsed laser deposition (PLD). Firstly, a structurally disordered thin film of ≈ 200 nm deposited via PLD at 30°C onto a 200 nm thick Si_3N_4 window and secondly; a graphitic-like carbon thin film of ≈ 200 nm was prepared and deposited via PLD at 560°C onto a 100 nm thick Si_3N_4 window. The samples were both irradiated using a 2.25 MeV proton micro beam with fluences ranging between 0.1 and $50 \text{ nC}/\mu\text{m}^2$. Protons of 2.25 MeV have a longitudinal range much larger than 200 nm (i.e. the sample thickness) hence the projectile protons will not be embedded in the carbon thin films. This provides a platform to investigate the irradiation effect without the influence of hydrogen from the proton beam.

Results from this investigation show that proton irradiation induces ferromagnetic ordering in carbon materials that originates from the spin polarization of the carbon π -electrons. While σ -electrons do not exhibit any XMCD contrast upon X-ray polarization changes and thus do not contribute to magnetic moment of the carbon system. The π electrons are sensitive to changes in X-ray probe polarity. The different carbon thin films produced exhibit a XMCD signal i.e. possess non-zero magnetic moments following proton irradiation, however, the magnetic moment in the graphitic-like sample show a higher magnetic moment than the disordered carbon sample. This observation supports the role of π -electrons in the magnetism of carbon since larger order in the π bonds leads to higher value and anisotropy of the orbital moment and hence anisotropy of the magnetization [29].

The XMCD results further question the role of hydrogen in magnetically

ordered carbon since a negligible fraction of projected protons are captured by the 200 nm carbon thin films. However, proton irradiation at 2.25 MeV energy provides sufficient energy to dissociate surface molecular hydrogen and displace resulting atomic hydrogen deeper into the surface/bulk. Therefore, only in this sense can hydrogen contribute to the magnetic state of the sample given the different bonding configurations discussed above. Theoretical studies using DFT methods have indicated that the primary ferromagnetic contribution in proton irradiated carbon (graphite) originates from ~ 20 nm from the surface [170]. In addition, low-energy muon spin rotation (LE μ SR) experiments on HOPG samples indicate the formation of ferromagnetic layer of ~ 15 nm thickness [171]. Therefore, the XMCD results provide further evidence indicating that the ferromagnetic contribution in carbon following proton irradiation possibly originates from the surface and near-subsurface regions at least $< 1\mu\text{m}$ from the surface.

In ion irradiated carbon materials such diamond, graphite and graphene, both single or monovacancies (V_1) as well as multivacancies (V_n) can be created. Multivacancies can be formed via agglomeration of neighbouring single vacancies in the collision cascade during irradiation. Known multivacancies in carbon (graphite) include V_2 , V_4 , V_6 , V_9 . Experimental investigations involving low energy carbon irradiation of graphite [15, 168] as well as corresponding theoretical studies [15, 32, 168] have provided further insight on phenomenon of magnetic carbon and role of vacancies therein. Results from positron annihilation lifetime spectroscopy (PALS) have shown that monovacancies are the dominant defects near the end of range (EOR) of the projectile in carbon irradiated graphite while multivacancies such as V_6 and V_9 defects are more dominant near the surface. It has been shown that some multivacancies also exhibit stable magnetic moments e.g. the V_6 defect with a planar ring structure exhibits a magnetic moment of $\sim 5.54 \mu_B$ with an energy difference of 0.67 eV between spin polarized and spin unpolarized states [168].

Nonetheless, in spite of both experimental and theoretical progress towards interpreting the observed room temperature magnetic ordering in carbon materials, recent studies [30, 173] highlight possible significance of artifacts induced by metallic impurities in carbon-based macroscopic magnetic ordering at room temperature. The prediction of an intrinsically long range magnetically ordered states in graphene sheets (discussed above) has attracted considerable interest in the scientific community especially with the prospect of fabricating spintronics devices in which both charge and spin manipulation can be achieved [25, 169, 174]. The key issues surrounding the phenomenon of carbon based magnetic ordering at room temperature are; (i) role of magnetic impurities introduced during synthesis on the overall magnetic response of the sample and (ii) identifying the mechanism(s) that mediates coupling between the magnetic moments. The role of experimental parameters in triggering various magnetic properties in pure carbon systems is of fundamental importance. These include, ion species, ion energy, ion beam size, beam current and current density. The experimental aspects and implications of these parameters on the magnetic properties of carbon are discussed in the next section with particular focus on diamond.

Chapter 5

Experimental Techniques

This section covers the details of experimental aspects utilized in the present study. Only the details deemed relevant in the context of this thesis are discussed, including:

- Sample Preparation
- Particle Accelerator Techniques
- Nuclear Microprobe
- Elemental Analysis Techniques (PIXE, RBS)
- Irradiation Parameters
- Atomic Force Microscopy (AFM)
- Magnetic Force Microscopy (MFM)
- Electric Force Microscopy (EFM)
- Raman Spectroscopy
- Photoluminescence Spectroscopy
- Superconducting Quantum Interference Device (SQUID)

5.1 Sample Preparation

Carbon materials used as targets for systematic ion irradiation in this study are diamond (types Ib and IIa) as well as highly oriented pyrolytic graphite (HOPG). However, our focus in this thesis will be on the studies in diamond. For the purposes of investigating surface nanostructuring by means of impact of HCIs, diamonds of type-Ib with nitrogen content ~ 50 ppm obtained from DeBeers Element Six in South Africa were used. From known literature, the dimensions of surface defects created by impact with SHCIs are expected to be ~ 10 nm. To enable effective characterization by AFM techniques, the surfaces of the target material have to be atomically flat. Due to the high mechanical hardness of diamond, polishing diamond surfaces is typically a challenging task that hardly results in adequate atomically flat surfaces. Most reliable polishing techniques cannot produce sufficiently low surface roughness which is essential for imaging nanoscale structures using AFM techniques.

The relatively weaker points in the diamond structure are found along its crystallographic axes. To exploit this feature, a laser system at iThemba LABS in Johannesburg South Africa, was used to align (identify) the $\langle 111 \rangle$ crystallographic axes of the diamond samples. A small incision was then made on the surface of the diamond which corresponds to the $\langle 111 \rangle$ axis. The incision was then used to cleave the diamond samples along $\langle 111 \rangle$ axis to expose atomically flat terraces which can be analyzed using Atomic Force Microscopy (AFM) techniques. To prepare the diamond samples for experiments, the samples were cleaned in a $\text{HNO}_3 + \text{H}_2\text{SO}_4 + \text{HF}$ tri-acid solution for approximately 60 minutes using an ultrasonic bath to remove (residual) surface impurities and/or edge contamination. An optical microscope was used to assess the extent of cleaning process.

HCIs utilized in the present investigations were produced using different facilities. Firstly, Xenon HCIs with charge states varying between $q = 20 - 31$

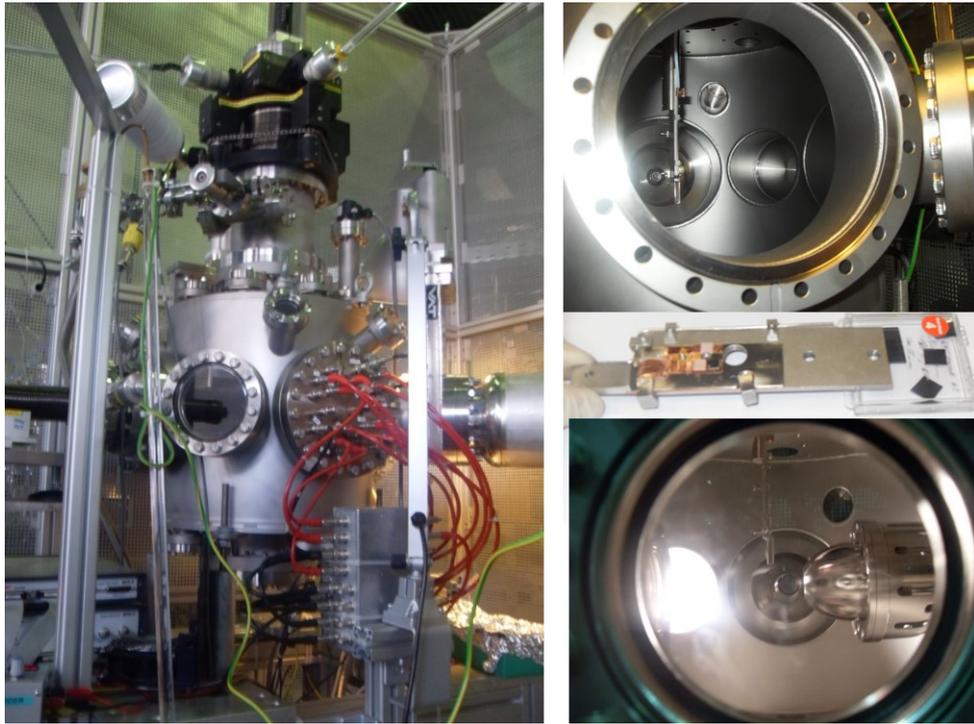


Figure 5.1: *Target preparation and experimental end station of the EBIT at Max Planck Institute in Heidelberg*

were produced using the Electron Cyclotron Resonance technique at GANIL in France to investigate the surface nanostructuring in a relatively lower charge state regime. The Heidelberg EBIT was used to produce Bismuth HCIs with charge states varying between $q = 50-62$ to investigate the higher charge state regime. Fig. 5.1 shows the images acquired during target preparation at the experimental end station at Max Planck Institute: (*left*) the target chamber in a Faraday cage, (*top right*) mounted sample holder in target chamber, (*mid-left*) sample holder with mounted samples, (*bottom left*) view through a target chamber window showing the mounted sample holder and the back end of the beam deceleration tube.

To investigate the evolution of physical properties in diamond induced by energetic proton irradiation, two approaches were adopted, *viz.*, using micro-beam irradiation and macro (bulk) beam irradiation. In order to avoid interfer-



Figure 5.2: Target chamber with golden quartz sample holders at the 5 MV Tandem Accelerator in CMAM.

ence and noise from impurities and various defect centers, ultra pure type-IIa diamonds were used for these investigations. The observation of magnetic effects was the primarily focus of these investigations although optical properties were investigated in the process. The macro irradiation experiments were carried out at the Centre for Microanalysis of Materials in Madrid Spain using the 5MV Tandem accelerator.

Two near-identical type-IIa ultra pure diamond samples with dimensions $4 \times 4 \times 0.25 \text{ mm}^3$ were utilized for the the macro irradiation experiments. The diamond samples were cleaned in an ethanol solution in an ultra-sonic bath

to remove possible residual surface (and/or edge) impurities prior to irradiation. Following analysis under an optical microscope, the diamond samples were mounted onto specially made golden quartz sample holders designed for mounting samples in the target implantation chamber as well into the SQUID sample holder to minimize sample handling and possible proliferation of contamination. Fig. 5.2 shows an example of the golden quartz sample holder with a mounted sample (*left*) as well as the target chamber (*top left*) with the golden quartz sample holders mounted inside (*bottom left*) at the CMAM 5 MV Tandem accelerator.

Micro-irradiation experiments were carried out at the iThemba LABS in South Africa using two different accelerators, *viz.* the Van der Graaf accelerator at Faure as well as the 6 MV Tandem accelerator in Gauteng. These facilities were used to create micro-scale irradiated regions in type-IIa diamond samples using nuclear microprobe techniques.

5.2 Ion Sources

5.2.1 Electron Beam Ion Trap (EBIT)

The EBIT is a (*electro-mechanical*) device designed to breed, store highly charged ions (HCIs) using an electron beam of very high current density. For the purposes of our experiments the HCIs were extracted from the trap by applying an electrical bias to one terminal of the trap region. The extracted ions were then channeled by means of various beam-line components (see later) to the target chamber to perform HCI irradiation. The EBIT was developed at Lawrence Livermore National Laboratory (LLNL) by Mort Levine and Ross Marrs. It is currently the only ion source in the world that can create HCIs at rest thus enabling investigations of exotic domains of potential energy versus

kinetic energy.

In an EBIT an electron beam focused using a set of Superconducting Helmholtz coils to a current density of about 5000 A/cm^2 is accelerated at uniform energy to a target gas mixture in the ion trap region. The trap region is typically under ultra high vacuum (UHV) conditions and is under high magnetic confinement due to the strong field induced by the coils resulting in a dense gaseous mixture within a diameter of $60\text{-}100 \mu\text{m}$. The electron beam continuously ionizes the target until the binding energy of the next bound electron exceeds the beam energy. In this way, HCIs with predetermined charge states can be created.

Confinement or trapping of the ions created by the successive electron bombardment is achieved both radially and axially. The positive ions created by the bombarding electron beam are electrically attracted to the negatively charged electron beam along the axis of the electron beam thereby creating space charge confinement of the HCIs in the radial direction. In the axial direction, confinement is achieved by applying voltage to the terminal drift tubes such that the terminals are positively charged to repel the positively charged ions. In addition, the system is under magnetic confinement induced by the superconducting Helmholtz coils (see Fig. 5.3).

For the purposes of our experiment, the HCIs have to be extracted from the potential well and systematically accelerated towards the diamond targets described above to investigate resulting morphological changes and responsible interactions leading to them. Applying a negative extraction bias at one end of the drift tube assembly accelerates the HCIs out of the trap along a beam line and eventually towards the desired target. In practice, a complex mixture of HCIs with different atomic number/nuclear charge and electronic charge states is created by the EBIT. Therefore to obtain a beam of HCIs with a single atomic number and electronic charge state, the extracted beam is channeled

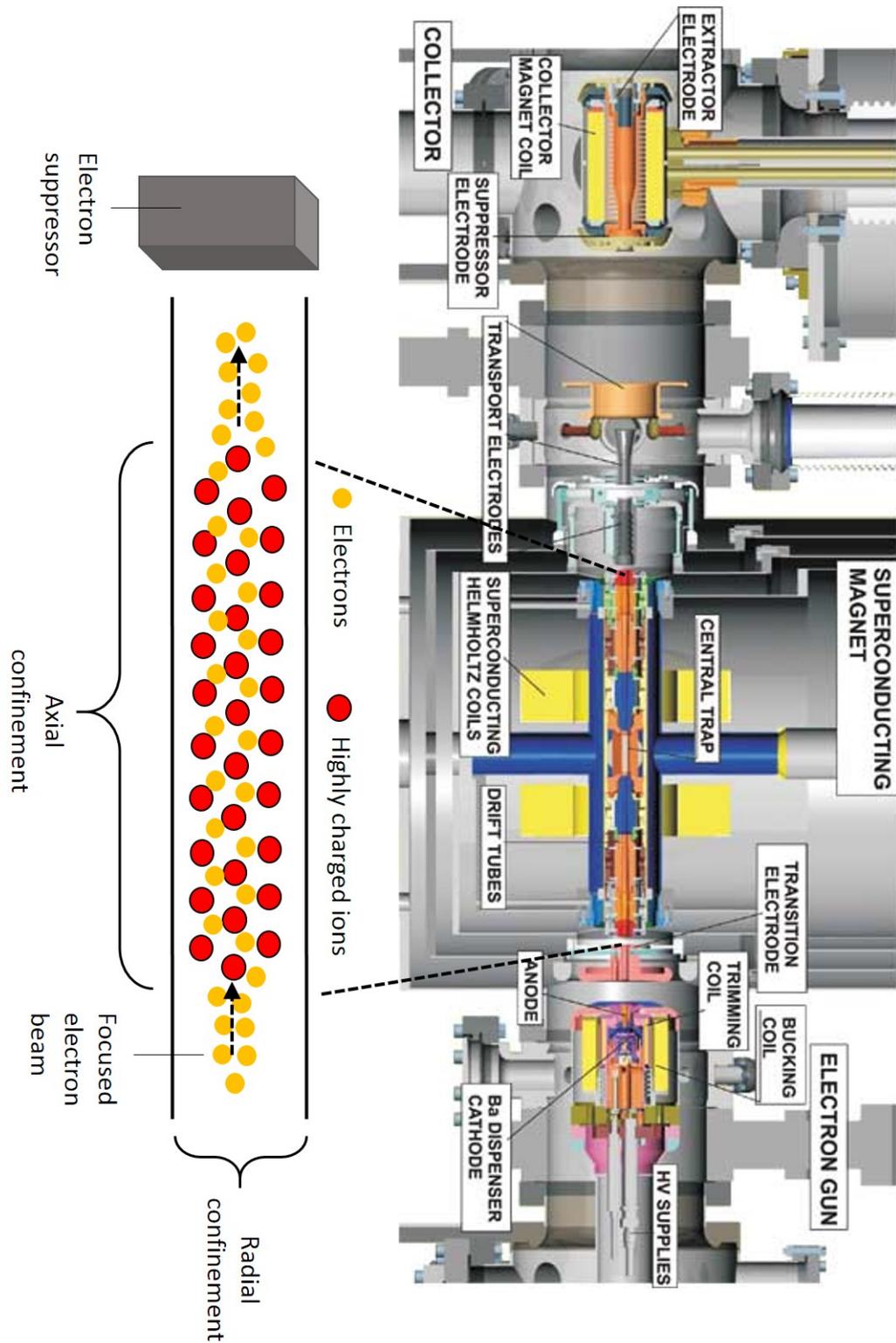


Figure 5.3: Diagram showing the Heidelberg EBIT used for the production of Bismuth HCIs used in the present study.

through an analyzing magnet which separates the different HCI species using the charge to mass ratio.

5.2.2 Electron Cyclotron Resonance Ion Source (ECRIS)

Majority of the heavy ion accelerators such as CERN, GANIL, iThemba LABS, make use of ECR sources for the production of a wide range of ion species, including multiply charged ions. In an ECR ion source, ions are produced in a microwave heated plasma under magnetic confinement. The production of multiply charged ions with an ECR ion source requires several conditions including the following:

- Appropriate magnetic field strength and structure
- Adequate microwave frequency and power
- Good vacuum
- Constant flow of material into the plasma chamber and
- Suitable extraction system

In a typical ECR system, magnetic confinement is achieved by generating an axial magnetic field using solenoids and a radial field using hexapole magnets. The geometry of the system allows the creation of the so-called minimum-B magnetic field structure inside the plasma chamber which is located at approximately the centre of the plasma chamber. The introduction of microwave energy into the system results in the generation of a rapidly changing electric field, \vec{E}_{ext} in the confined plasma.

Free electrons, which move in helical paths in the plasma are accelerated by the electric field thus ionizing atomic and molecular species in the plasma and resulting in the formation of ion species in the plasma chamber. In this way the electrons are heated stochastically and the plasma is ignited. The

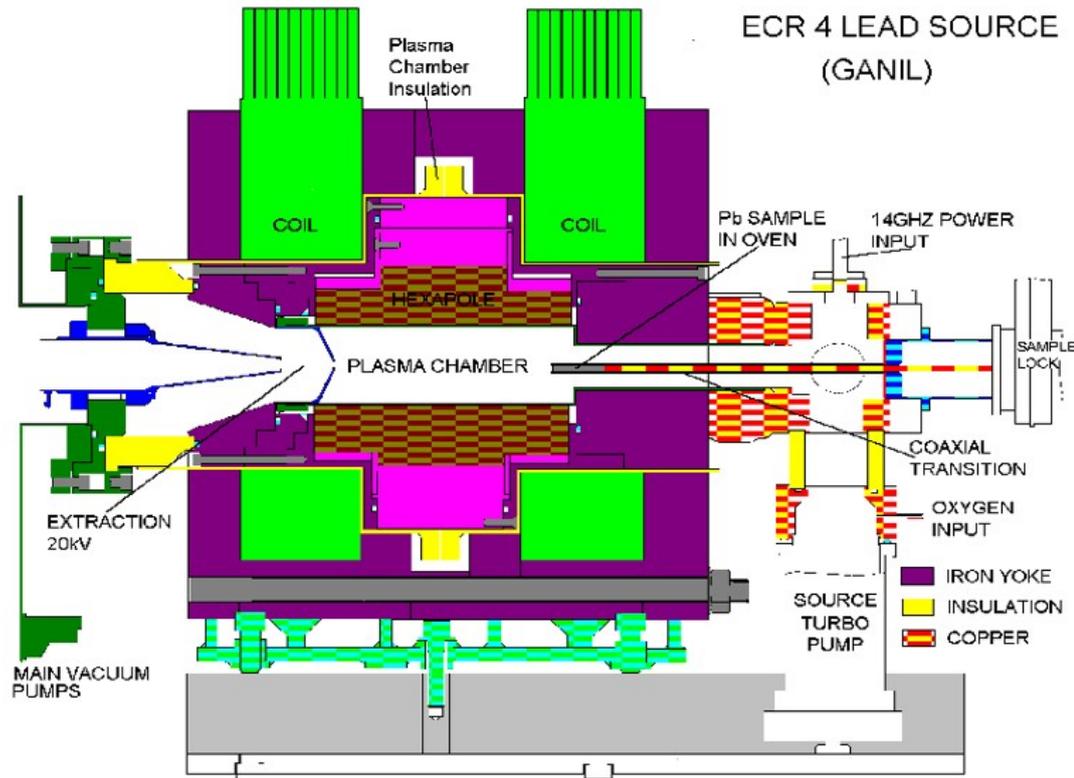


Figure 5.4: Schematic diagram showing the ECR 4 Lead Source used for ion production including HCIs at GANIL in France.

stepwise nature of the ionization process results in the generation increasing number of electrons in the plasma therefore the plasma ignition proceeds like an avalanche until an equilibrium is reached. Electron Cyclotron Resonance is achieved when the gyration frequency of the electrons ω_{ce} equals the frequency of the applied electromagnetic waves (microwaves) ω_{RF} , i.e.:

$$\omega_{ce} = \frac{eB}{m_e} \omega_{RF} \quad (5.1)$$

where B is the magnetic field [175].

When producing HCIs, the vacuum has to be very good to reduce the probability of charge exchange between ions and neutrals which increases in direct proportion to the pressure in the plasma chamber. Ion extraction from

the chamber is achieved by applying electric fields to the extraction line from the chamber. In this a way a potential difference between the beam-line and ion source is created which accelerates ions out of the plasma chamber. In the present work, the ECRIS were used for the production of protons which were injected into the low voltage terminal accelerated to 2.2 MeV using the 6 MV EN Tandem Accelerator at iThemba LABS in Gauteng for magnetism experiments in diamond and HOPG. In addition, the ECRIS was used for the production of Xenon Highly Charged Ions (HCIs) of intermediate charge states at GANIL in Caen France (see Fig.5.4) for use in surface nanostructuring studies in type-Ib diamond.

5.2.3 Duoplasmatron Ion Source

The duoplasmatron ion source was developed by V. Ardenne in 1956 from the concept of the unoplasmatron ion source [176]. This type of ion source is commonly used for the production of H and He ions. The duoplasmatron ion source, is typically composed of two ('duo') plasma regions one of lower density which is between the cathode and the intermediate electrode (IE) and the high density plasma between the IE and the anode. The cathode plasma is compressed by a double layer into the IE channel and then further compressed by an axial magnetic field. In this way a very high plasma density (10^{14} cm^{-3}) can be reached [176].

The duoplasmatron ion source can be configured to produce both negative and positive ions. In the present study, the duoplasmatron ion sources were used for the production of protons beams for use in magnetism studies in diamond. A schematic diagram of a duoplasmatron ion source is shown in Fig.5.5. At CMAM in Madrid Spain, the duoplasmatron ion source was used to produce H^+ ions. These ions were further accelerated up to 2.2 MeV using a Tandem accelerator for energetic macro irradiation of ultra pure type-IIa

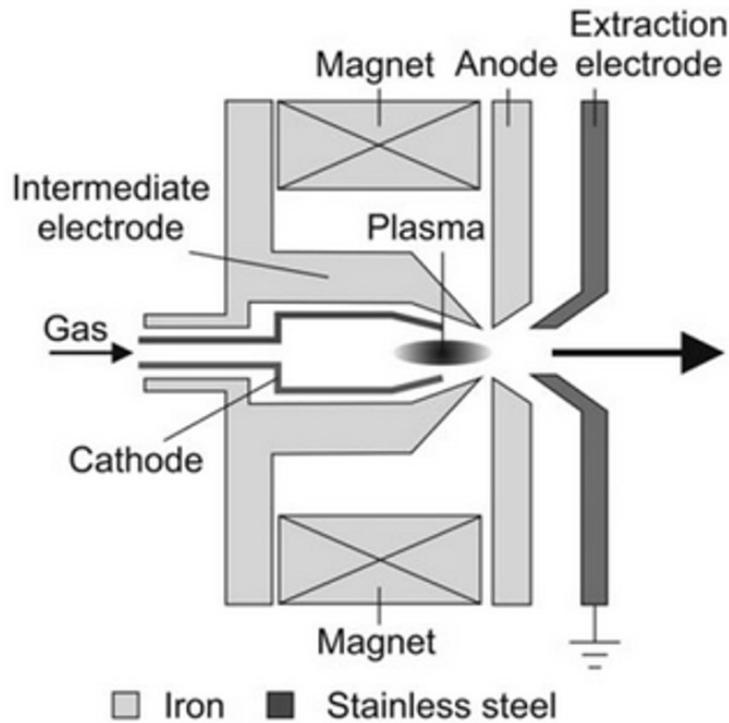


Figure 5.5: *Top: Schematic diagram of a duoplasmatron ion source [176].*

diamond. At iThemba LABS (Somerset West), the duoplasmatron ion source was also used for the production of protons which were further accelerated using a vertical Van der Graaff accelerator up to 2.2 MeV and directed through a Nuclear Microprobe system to produce micro-beams for irradiation of Ila diamond (and HOPG).

5.2.4 Source of Negative Ions by Cesium Sputtering

In order to produce 2.2 MeV protons using the Tandem Accelerator, negative ions have to be injected into the accelerator. At iThemba LABS negative ions were produced using the Cesium Negative Ion Source (see Figure 5.6) commonly known as the Source of Negative Ion by Cesium Sputtering (SNICP). In the SNICP, cesium vapour is created by heating cesium metal in an oven at

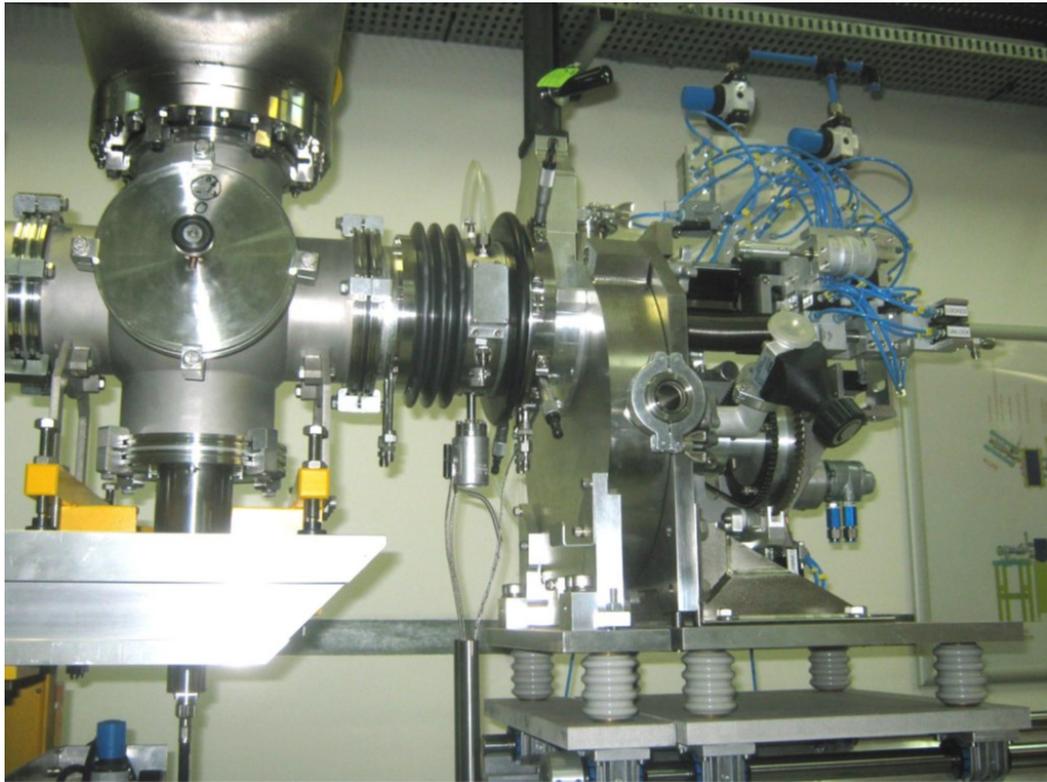


Figure 5.6: *Top: Source of Negative Ions by Cesium Sputtering (SNICP) at iThemba LABS.*

$\sim 120^\circ$. The Cs vapour then fills a confined space between the cooled cathode and a heated ionizing surface. A fraction of the Cs vapour partly condenses on the cooled cathode surface and is partly ionized thermally by the heated surface. The positive cesium ions created by the thermal ionization process are subsequently focused and accelerated towards the cathode, ultimately sputtering the cathode through the condensed Cs layer. Some materials preferentially sputter negative ions while for those materials which preferentially sputter positive ions, the ions bind to electrons as they pass through the condensed layer Cs thus creating negative ions.

5.3 Particle Accelerator Techniques

Our studies require the use of various ion species for irradiation of diamond at desired energies. Ions therefore have to be extracted from the plasma chamber and accelerated using particle accelerator techniques. Extraction of ions from the plasma chamber is in general limited by the emission capability or by space charge forces. In the case of space charge limitations, the maximum ion current density j_{sc} is given by the Child-Langmuir formula [177, 178]:

$$j_{sc} = \frac{4 \cdot \varepsilon_0}{9} \sqrt{\frac{2 \cdot n \cdot q}{M \cdot m_a}} \cdot \frac{\Phi^{3/2}}{d^2} \quad (5.2)$$

where ε_0 is the absolute permittivity, q the electric charge, n the charge state, M the mass in atomic mass units, m_a the atomic mass unit, and Φ is the potential drop across the extraction gap d . For practical purposes, the maximum ion current density is thus given by:

$$j_{sc} [mA \cdot cm^{-2}] = 1.72 \cdot \sqrt{\frac{n}{M}} \cdot \frac{\Phi [kV]^{3/2}}{d [mm]^2}. \quad (5.3)$$

The space charge limited ion current is proportional $\Phi^{3/2}$. This proportionality factor is known as the perveance and describes the beam broadening due to repulsive forces in the space charge region [176].

The emission limited ion current density j_p extracted from the plasma ion source is given by formula:

$$j_p = 1.57 \times 10^{-10} \cdot n_i \sqrt{\frac{z \cdot T_i}{M_i}} \quad (5.4)$$

where n_i is the ion density in the plasma, z is the charge state of the ion, T_i is the ion temperature and is M_i the ion mass.

The simplest widely used method of accelerating charged particles such as H^+ and HCl is achieved by exploiting the electrostatic field generated when a potential difference U_{ext} is applied across extraction gap. The Cockcroft-Walton accelerator built by J.D Cockcroft and E.T. Walton in 1932 is the prototype of an electro static accelerator that still finds application in many variations in accelerators to date. The high voltage generator of the Cockcroft-Walton accelerator is the well known cascade generator or voltage multiplier circuit invented by H. Greinacher in 1921 [179]. Extracting a DC current causes a mean voltage drop of ΔU and ripple δU which are proportional to the DC current I . Cockcroft and Walton shared the 1951 Nobel Prize in physics for the development of the Cockcroft-Walton accelerator and demonstration of Nuclear physics studies using their system [180].

For the purpose of generating high potential fields for particle acceleration, typically \sim MV, the Van der Graaff generator/accelerator has been widely used. The Van der Graaff generator/accelerator was invented by American physicist Robert J. Van de Graaff in 1929 [181]. One notable advantage of the Van de Graaff accelerator is that it produces very high DC voltage at low current levels. The system is based on continuous accumulation of electric charge on a hollow metallic globe connected to an insulated column. Charge accumulation using a moving belt/chain e.g. the pelletron system is used in Tandem Accelerators to deliver charge to the metallic globe/terminal using a brush or comb of metallic wires. The terminal behaves like a spherical capacitor which has capacitance $C = 4\pi\epsilon_0 r = (1.11 \cdot 10^{-10} F/m)r$ where r is the radius of the terminal electrode [182].

The Tandem accelerator design is based on the Van der Graaff accelerator. The Tandem uses a two stage acceleration process involving a combination of a positive and negative potential to double the energy output. The pelletron system used to charge the terminal of Tandem accelerator to create highly

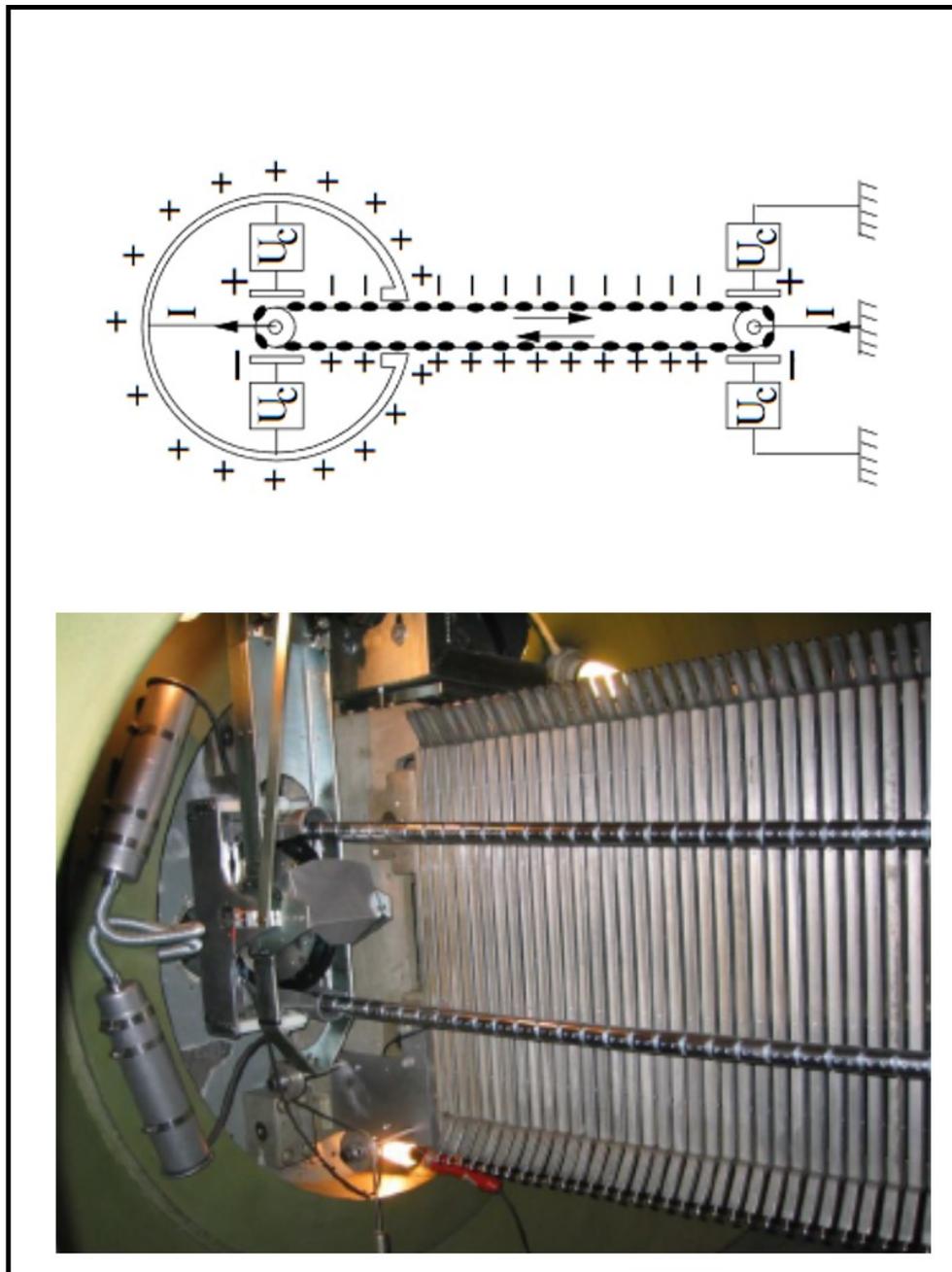


Figure 5.7: Top: Schematic diagram of the pelletron and ladderton high voltage generator [182]. Bottom: Pelletron charging system at iThemba LABS in Gauteng during a maintenance operation.

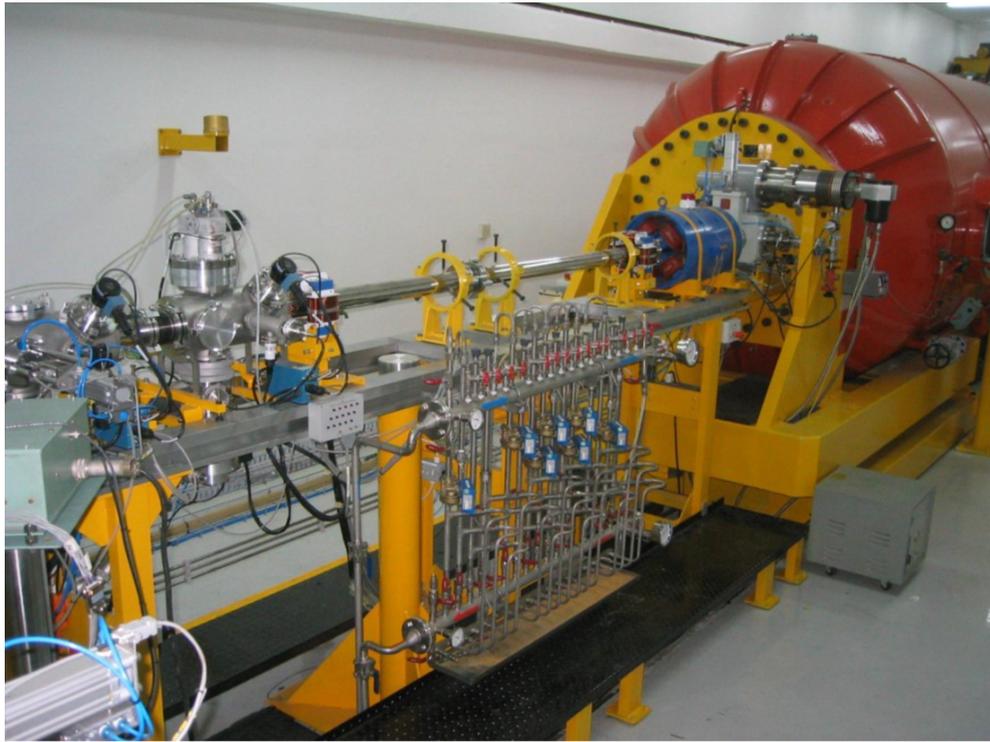


Figure 5.8: *The 6 MV Tandem accelerator at iThemba LABS in Gauteng, South Africa.*

accelerating potentials consists of charged metal pellets interconnected using nylon links forming a chain. Ladderton charging chains are made of metal plates. The pellets are slightly charged and are used to transfer charge to the terminal as the chain is driven by the pulleys. Figure 5.7 shows a schematic diagram of the pelletron and ladderton high voltage generator system.

A notable disadvantage of the standard Tandem accelerator is that it requires negatively charged ions as input into the Van der Graaff based accelerator which are practically very difficult to produce especially for higher qe , for ($q = 1, 2, 3\dots$). In the first acceleration stage, negatively charge ions each carrying charge $-e$ are accelerated towards the positive terminal charged to an externally applied potential U_{ext} thus gaining kinetic energy $|-eU_{ext}|$ assuming the highest negative charge state produced is $q = 1$. When the ions reach the positive terminal they are channeled through a 'stripper' typically made of

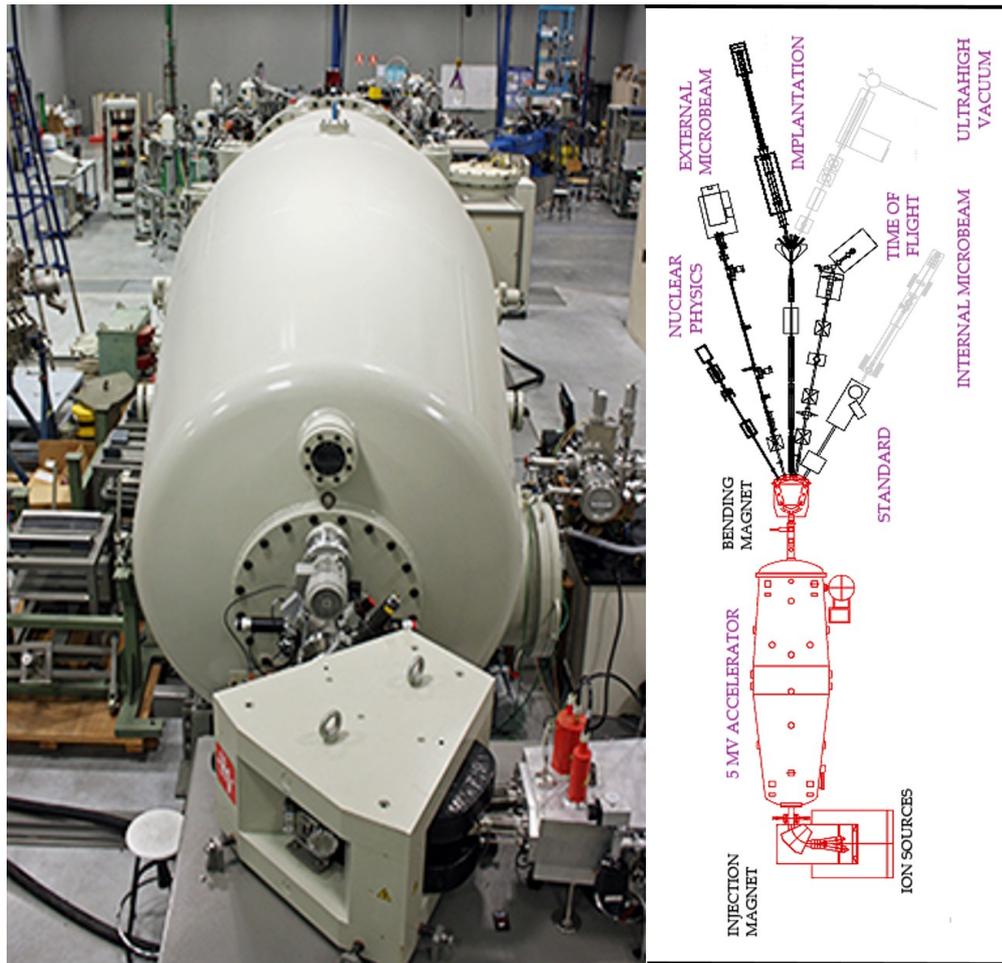


Figure 5.9: 5 MV Tandem Accelerator (left) with schematic diagram showing ion/particle beam lines (right) at CMAM.

carbon or a gas such as argon which strips or removes electrons from the ions thereby altering their charge into a positive state. Ions are thereafter repelled (accelerated) away from the positive terminal thereby gaining additional energy $|-qeU_{ext}|$ which is typically in the range MV. In total, each ion gains total kinetic energy $E_{kin} = (1+q)eU_{ext}$, where e is the electron charge and for heavy ions, $q \gg 1$.

In practice the tank has to be filled with insulating gas to reduce the probability of arcing and corona discharge caused by electrical breakdown of the insulation due to excessive electric fields at the surface of the terminal [182].

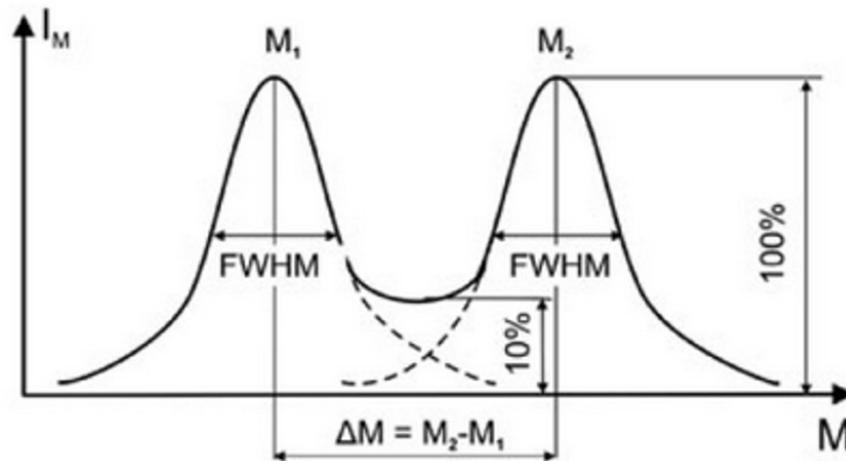


Figure 5.10: Schematic diagram for determination of the ion mass resolution of analyzing section magnets [176]

In addition, the accelerating tube of the Tandem has to be evacuated to limit secondary electron emission from charge exchange reactions which reduce the terminal voltage and produce harmful X-rays. Figure 5.8 shows the low voltage injection end of the 6 MV EV Tandem accelerator at iThemba LABS in Gauteng, South Africa, one of the two Tandem accelerators used in the present study. The 6 MV EN Tandem was used in conjunction with the nuclear microprobe to produce proton microbeams of 2.2 MeV kinetic energy with a spatial resolution of $1 \sim \mu\text{m}$. The second tandem accelerator was used to produce proton macro (bulk) beams with energies in the range 1.4-2.2 MeV and fluence in the range $3.8\text{-}22 \times 10^{17} \text{ H}^+/\text{cm}^2$ at CMAM in Madrid, Spain (see Fig. 5.9).

After (and before) the accelerated ions exit the high voltage terminal of the Tandem accelerator, various beam elements/beam optics are used to produce the desired output beam. In practice the beam produced is a composite beam consisting of various charge states and mass carrying different kinetic energies. To obtain a 'homogenous' beam consisting of a single type of ion species, the composite beam is channeled through an analyzing section magnet which

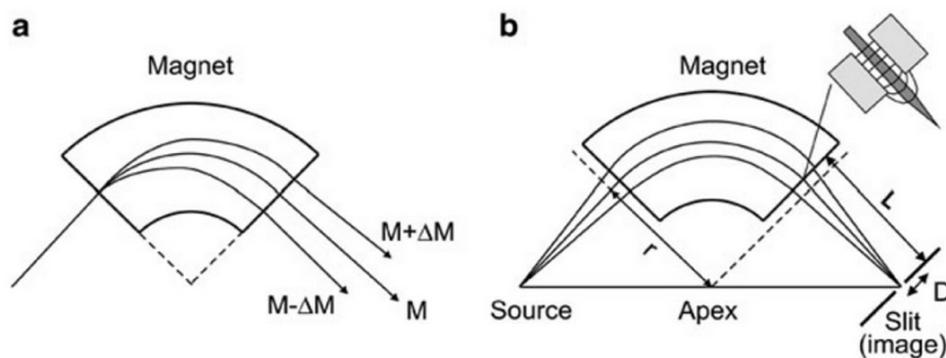


Figure 5.11: Scheme of the basic sector magnet for mass analyzing. (a). The higher masses are less deflected and the lower masses more. Co-linearity (Barber's rule) of sector magnet object (source), image, and magnet apex (b). Due to the extended magnetic field the pole faces can be shifted relative to the dotted line by a distance in the order of gap width of the exit slit [176].

spatially separates ions according to their charge to mass ratio, q/m . Analyzing sector magnets can be characterized by their ion mass resolution as well as their magnetic rigidity. In the former, $R = M_i/\Delta M$, in general this happens where $\Delta M \approx 2 \cdot \text{FWHM}$. Two masses are resolved if the intensity valley between the adjacent masses less than 10 % of the intensity of the mass lines (see Fig. 5.10) [176].

The magnetic rigidity is given by: $Br = (m/q)v$ [176]. In the case of 90° sector magnets, if the direction of the incident ion beam is perpendicular to the magnetic field inside the sector magnet, the ions will follow a circular trajectory of radius r . In this configuration, the magnetic force $F_m = qvB$ is equivalent to the centripetal force, $F_r = Mv^2/r$ and the ions travel along a circular trajectory where the radius r is given by:

$$r = \frac{M}{q} \cdot \frac{v}{B} = \frac{1}{B} \sqrt{\frac{2 \cdot M}{q} \cdot U_{ext}} \quad (5.5)$$

where M , q , v , B and U_{ext} are the ion mass, charge state, ion velocity, mag-

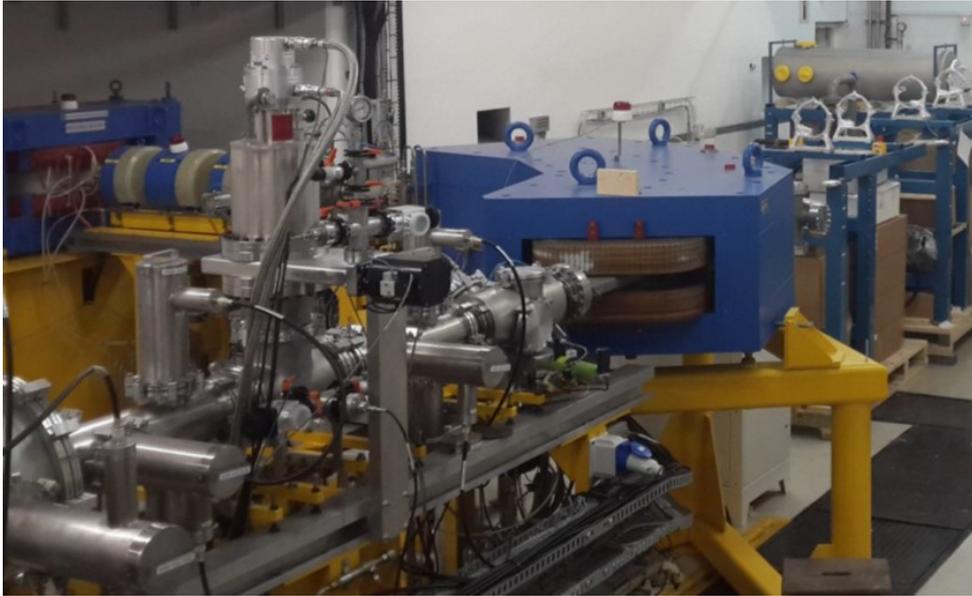


Figure 5.12: Analyzing 90° sector magnet at iThemba LABS in Gauteng.

netic field intensity (induction) and the extraction voltage respectively [176]. Therefore ions with different mass and equal charge are deflected to different paths. By placing a slit in the image plane of the magnet only one mass to charge ratio m/q will have the correct radius of curvature to exit the mass separator. In 90° magnets, the field is typically homogenous and perpendicular to the beam direction, and the beam object and image are symmetric. In this configuration, where a beam enters and leaves a 90° magnet, perpendicular to the magnetic field in the magnet, the separation D for a mass difference $\pm\Delta M$ is given by (see Fig. 5.11)

$$D = \pm \frac{r \cdot \Delta M}{2M} \left(1 - \cos\varphi + \frac{L}{r} \cdot \sin\varphi \right) \quad (5.6)$$

where r is the radius of the analyzing magnet, L is the length from the magnet to the image plane (exit slit) and φ is the angle between the magnet entrance and exit planes (see Fig 5.11). For example, upon exiting the analyzing sector magnet, the separation between ^{14}C is 8 cm, hence purpose built magnets with wide poles pieces at the exit are required to accommodate the

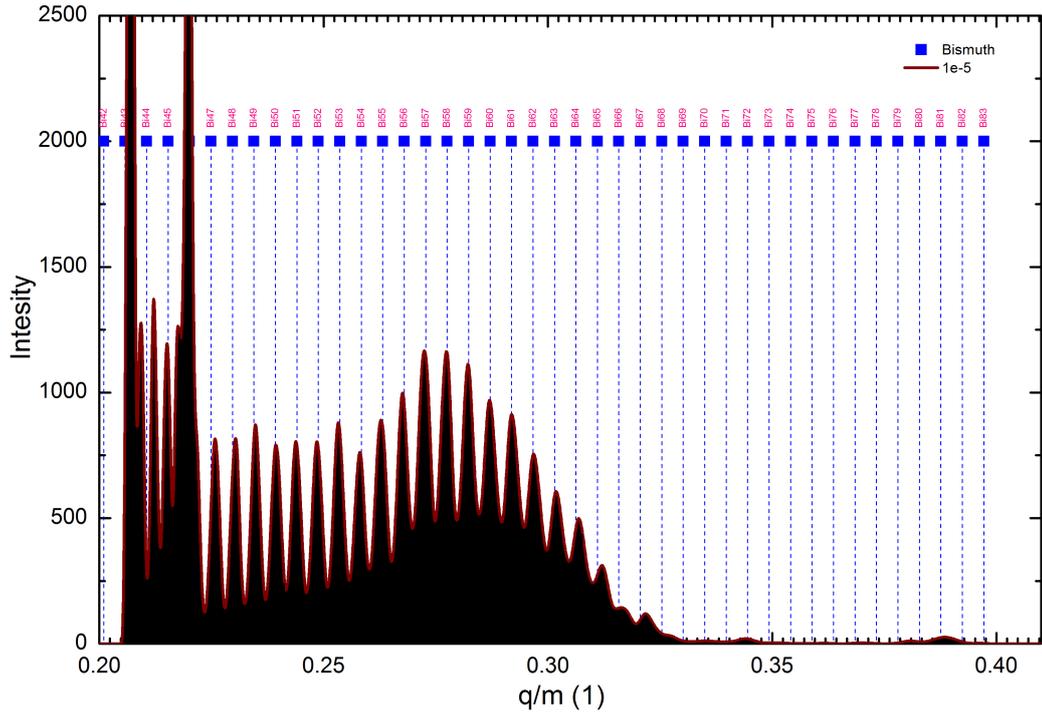


Figure 5.13: *Bismuth charge to mass selection through the 90° analyzing magnet at Heidelberg EBIT.*

different ion species [176]. Fig. 5.12 shows the actual 90° analyzing sector magnet used at iThemba LABS in Gauteng.

Figure 5.13 shows an example of resolved Bismuth intermediate charge states through the 90° analyzing magnet by mass to charge ratio at the Heidelberg EBIT at Max Planck Institute. For the highest bismuth charge state extracted, Bi^{62+} , the magnetic field intensity was $\sim 450G$. In practice, the charge to mass ratio is used, for the Heidelberg EBIT we typically have:

$$\frac{q}{m} = 7.615 \frac{U_{EBIT}(V)}{B^2(G)} \quad (5.7)$$

For example, using Fig.5.13 we have: for the highest charge state extracted, Bi^{62+} , $q/m \approx 0.295$, therefore $U_{EBIT} \approx 8055$ V. In practice $U_{EBIT} \approx 8115$ V primarily due to space charge effects. In our investigations of the nanoscale

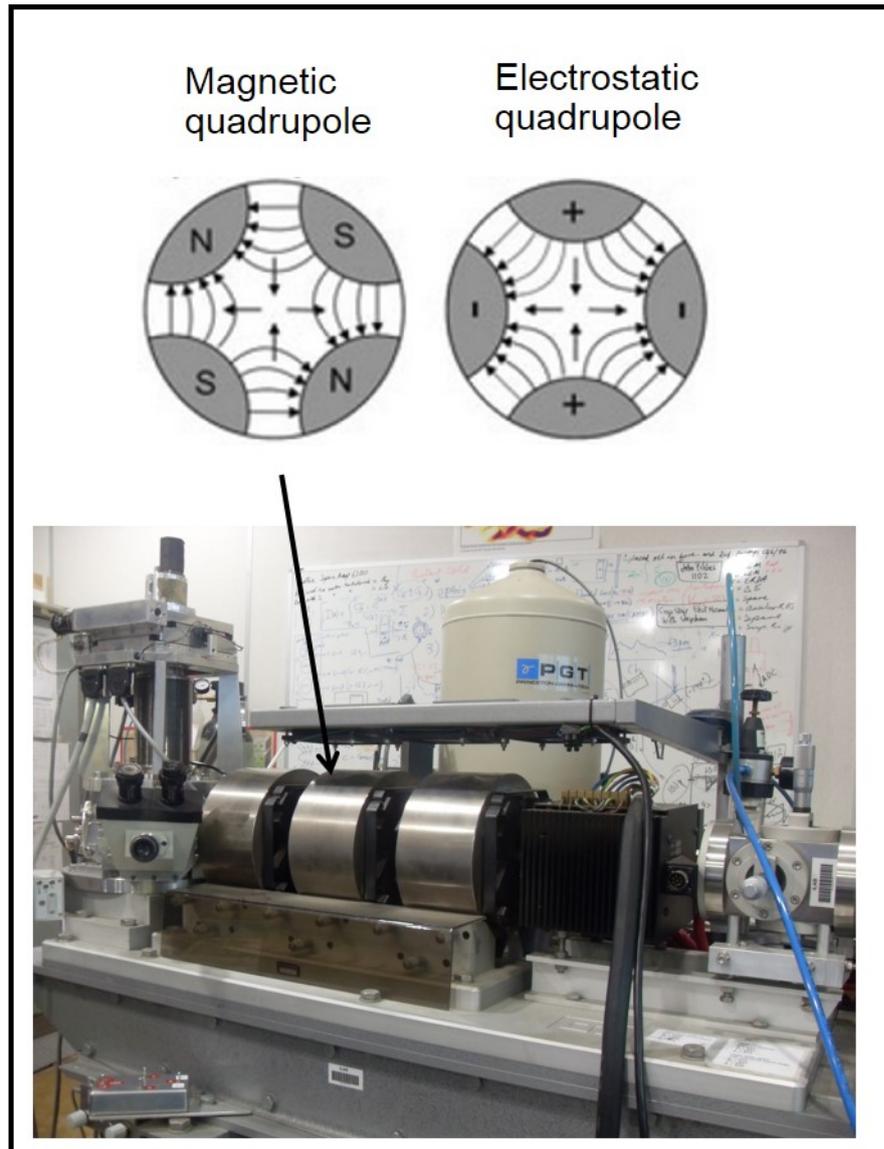


Figure 5.14: *Top: Schematic diagram showing the magnetic and electrostatic quadrupole [176], Bottom: Nuclear microprobe at iThemba LABS Faure.*

transformation of diamond surfaces for nanostructuring, Bismuth HCIs of intermediate range extracted from the Heidelberg EBIT are presented in Table 5.1.

The investigation of magnetic effects in an ultra-pure diamond matrix upon imparting a fluence $\sim 10^{17} - 10^{18} \text{ H}^+ / \text{cm}^{-2}$ within a microscale domain requires techniques to reproducibly construct a micro beam of $\sim 1 \mu\text{m}$ spatial resolution.

This was achieved by channeling the ion beam using a switching magnet to a nuclear microprobe end station after q/m ion separation in a 90° analyzing sector magnet. Experiments were carried out at iThemba LABS in Gauteng and Faure, where Oxford-type nuclear microprobes were used.

The Nuclear microprobe is in essence an ion beam focusing and scanning system with data acquisition devices commonly used in micro to sub-micro scale ion beam irradiation and analysis of materials. The Oxford-type nuclear microprobes used in the present study consists of precision collimation slits, quadrupole magnets used in series as a triplet with alternating polarities and a scanning system to raster the beam on a desired target within the target chamber. The target chambers are fitted with an X-Y-Z translation stage for sample positioning, an optical camera for beam and sample visualization and solid state detectors for Particle Induced X-ray Emission (PIXE) and Rutherford Backscattering Spectroscopy (RBS) based analysis of the target material.

A schematic diagram of the magnetic quadrupole is shown in Fig. 5.14 (*top*) together with its electrostatic analog. It is primarily composed of two N and two S magnets which focus the beam along one axis while defocusing along a perpendicular axis. When used in series with alternating polarities, the setup can be used as an effective beam focusing system.

Fig. 5.14 (*bottom*) shows one of the two nuclear microprobes used in the current investigation. In addition to its micro-irradiation capabilities, the Nuclear Microprobe used in the present study also provides an opportunity for in-situ elemental characterization in terms of distribution and quantification by means of the PIXE and RBS techniques.

For the PIXE technique, a Si(Li) detector was positioned at 135° from the beam axis in the target chamber. The signal from the detector was fed through a preamplifier, amplifier and through the analog to digital converter (ADC)

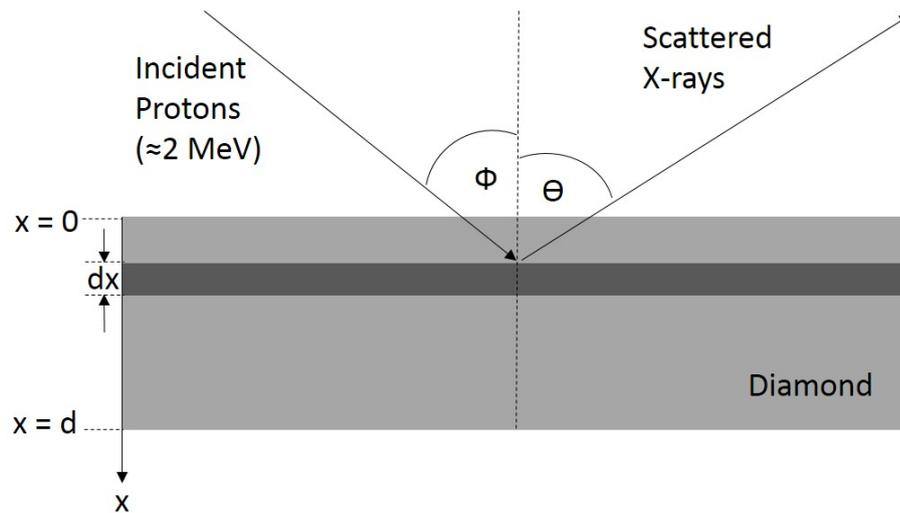


Figure 5.15: Schematic diagram showing the PIXE experiment for a proton beam incident on a diamond sample of thickness d .

where the signal is digitized and processed via software on the installed on the PC. In the PIXE technique, incident protons of ~ 2 MeV energy bombard the target material wherein inelastic collisions between the target atoms and protons take place. The protons create inner shell electron vacancies in the atomic structure of the target atoms. These vacancies are then filled by electrons from outer shells and this process is accompanied by the emission of photons (X-rays) which are unique to the energy state, also known as characteristic X-rays. Acquisition and analysis (including energy calibration) of these characteristic X-rays can be used to provide quantitative trace element analysis in the target sample. For the thick samples (i.e. where the beam is not transmitted through the sample) the quantification is in practice not trivial.

The quantification can be given by the energy integral that describes the intensity I of each X-ray line of the element Z as measured by a particular detector of efficiency ε_z :

$$I(z) = \frac{N_{Av}\omega_z b_z \varepsilon_z Q}{A_z e} C_z \int_{E_o}^{E_f} \frac{\sigma_z(E) T_z(E)}{S(E)} dE \quad (5.8)$$

where N_{Av} is Avogadro's number, A_z atomic mass, ω_z and b_z are fluorescence yield and branching ratio of a particular X-ray line, while Q/e is the total number of beam particles arrived at the target. C_z is the element concentration (if it is a function of depth inside then it is inside the integral), σ_z is the X-ray production cross-section, T_z is the X-ray absorption in the sample and S is the stopping power of ions in the material [183].

$$T_z(E) = \exp \left(- \left(\frac{\mu}{\rho} \right)_{z,M} \frac{\cos \phi}{\cos \theta} \int_{E_o}^{E_f} \frac{dE}{S(E)} \right) \quad (5.9)$$

and

$$\left(\frac{\mu}{\rho} \right)_{z,M} = \sum_i C_i \left(\frac{\mu}{\rho} \right)_i \quad (5.10)$$

where μ/ρ is the mass absorption coefficient, ϕ and θ are angles defined by the geometry of measurement as shown in Fig 5.15.

The energy efficiency of the Si(Li) detector can be determined by either direct measurement or by the theoretical predictions. Theoretically, the absolute efficiency ε of the detector is the product of the detector solid angle $\Omega/4\pi$, and its intrinsic efficiency ε_i . By neglecting the energy dependence of the detector solid angle (due to the different X-ray mean interaction depths in the detector), the detector efficiency is given by:

$$\varepsilon = \frac{\Omega}{4\pi} e^{-\sum_{i=1}^4 \mu_i t_i} f_E (1 - e^{-\mu_{Si} D}) \quad (5.11)$$

The exponential term corresponds to the absorption in each one of the 4 layers in front of the detector (Be-window, ice, contact layer and incomplete charge collection (ICC) layer). The factor f_E reflects the loss of events due to the Si K X-ray escape, while the last term describes the effect of the finite

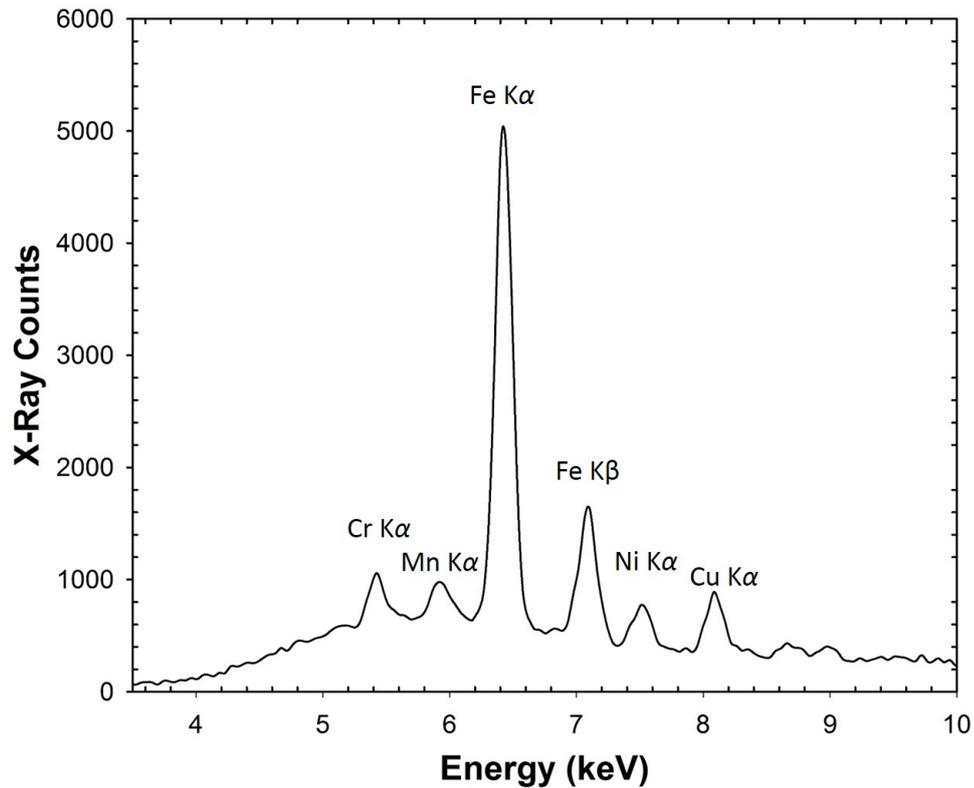


Figure 5.16: *PIXE spectrum acquired during irradiation of type-IIa diamond using a 2.2 MeV proton micro beam at iThemba LABS Faure.*

detector dimensions [183]. Fig. 5.16 shows the PIXE spectrum acquired during irradiation of a type-IIa diamond surface by 2.2 MeV Protons at iThemba Labs Faure in South Africa. A proton beam of current ≈ 10 nA was used to irradiate an area of approximately $(500 \times 500) \mu\text{m}^2$ using the nuclear microprobe. The PIXE spectrum shows a collection of trace elements in the diamond sample, mainly Fe, Ni, Cu, Cr and Mn which are incorporated into the ultra-pure diamond matrix in catalysis of the CVD diamond synthesis process.

The second analytical technique incorporated in the discussed accelerator setup is the RBS technique. In 1911 Rutherford used the backscattering of alpha particles on a Gold film to determine the fine structure of the atom, resulting in the discovery of the atomic nucleus. However, RBS was initially

described as a technique for materials analysis in 1957 by Rubin *et al.* [184]. The RBS technique is based on the backscattering of impinging particles (typically in the energy range $\sim 0.5 - 4$ MeV) from atomic nuclei in the sample. The dependence of the backscattering of incident particles on the atomic nuclei involved in the elastic collision allows for quantitative elemental analysis as well as depth profiling deduced from the energy loss of the particles along their path into and out of the sample. These parameters can be deduced without the necessity for reference samples. Depth resolution in RBS is \sim nm and sensitivity for heavy elements \sim ppm. RBS is however not very sensitive to lighter elements hence the necessity to use the technique in conjunction with other techniques such nuclear reaction analysis (NRA) or elastic recoil detection analysis (ERDA) for a broad range elemental analysis.

In the present study, protons of 2.2 MeV were used to irradiate atomically flat ultra-pure type-IIa diamond surfaces. A solid state detector was mounted in the target chamber to enable data acquisition for RBS analysis with the aim of estimating the range of the protons as well as the presence of magnetic impurities in the samples. The energy E_1 of a backscattered projectile with incident energy E_0 and mass M_1 after scattering in the laboratory system is given by:

$$E_1 = KE_0 \quad (5.12)$$

where the kinematic factor K is given by:

$$K = \frac{M_1^2}{(M_1 + M_2)^2} \left\{ \cos \theta \pm \left[\left(\frac{M_2}{M_1} \right)^2 - \sin^2 \theta \right]^{1/2} \right\}^2. \quad (5.13)$$

θ is the scattering angle and M_2 the mass of the target nucleus initially at rest [185]. In the case $M_1 < M_2$, as is the case in our current study for protons impinging on diamond, the plus sign in Eq.5.13 applies. The Rutherford cross-section for backscattering is therefore given in the laboratory system by:

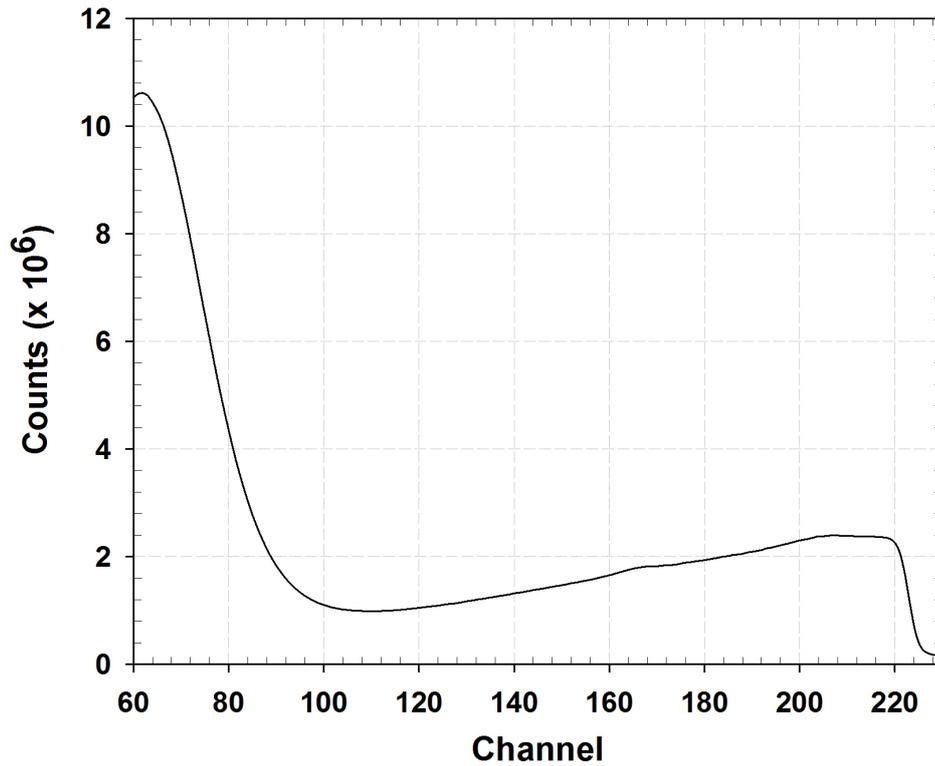


Figure 5.17: RBS spectrum acquired during irradiation of type-IIa diamond using a 2.2 MeV proton beam at iThemba LABS Faure.

$$\sigma_R [\text{mb/sr}] = 5.1837436 \times 10^6 \left(\frac{Z_1 Z_2}{E[\text{keV}]} \right)^2 \frac{\left[(M_2^2 - M_1^2 \sin^2 \theta)^{1/2} + M_2 \cos \theta \right]^2}{M_2 \sin^4 \theta (M_2^2 - M_1^2 \sin^2 \theta)^{1/2}} \quad (5.14)$$

where θ is the scattering angle, Z_1 and M_1 are the nuclear charge and the mass of the projectile, respectively, and Z_2 and M_2 are the nuclear charge and the mass of the target atom, respectively. σ_R is the differential cross-section in the laboratory system [185]. Fig. 5.17 shows the RBS spectrum acquired during irradiation of ultra-pure type-IIa diamond using 2.2 MeV proton micro beams at iThemba Labs in Faure.

5.4 Irradiation Parameters

Following production of Bismuth and Xenon SHCIs in the EBIT and ECRIS respectively, the SHCIs were channeled through an analyzing sector magnet where the charge to mass analysis was carried out as shown in Fig. 5.13 for the case of Bismuth. For the case of Bismuth, SHCIs were then directed via electrostatic elements through a High-Voltage deceleration stage to obtain extraction voltages between 400 V and 900 V. This then corresponded to kinetic energies ranging from 20 keV to 48 keV on target. Five charge states of Bismuth from $q=50+$ to $q=62+$ were produced which corresponds to potential energies ranging between 49 keV and 110 keV with fluence $(1-5)\times 10^9$ ions/cm² as per Table 5.1.

Table 5.1: *Table showing Bismuth Highly Charged Ions produced using the Heidelberg EBIT for surface nanostructuring experiments.*

Charge State (+e)	50	53	56	59	62
Kinetic Energy (keV)	30.0	21.2	47.6	35.4	37.2
Potential Energy (keV)	49.9	58.9	71.3	88.6	108.2

For the case of Xenon, after charge to mass analysis, the produced SHCIs were extracted from the plasma chamber using a constant extraction voltage of 15 kV. Table 5.2 provides a summary of HCIs produced using the GANIL ECR with their respective kinetic and potential energies.

A summary of irradiation parameters used at the CMAM Tandem accelerator in the investigations of magnetic effects following proton macro-irradiation of diamond is presented in Table 5.3 for both samples A and B. Four sets of macro irradiations were carried out on type IIa diamond sample A. The beam

Table 5.2: *Table showing Xenon Highly Charged Ions produced using the GANIL ECR for surface nanostructuring experiments.*

Charge State (+e)	20	23	27	29	31
Kinetic Energy (keV)	300	345	405	435	465
Potential Energy (keV)	4.56	6.53	10.4	13.7	17.22

Table 5.3: *Summary of irradiation parameters used at the CMAM tandem for proton macro irradiation of type-IIa diamond*

Irradiation	E (MeV)	F (H⁺/cm²)
SAMPLE A		
A:I1	2.2	3.8x10 ¹⁷
A:I2	2.0	7.1x10 ¹⁷
A:I3	1.8	9.9x10 ¹⁷
A:I4	1.6	12.4x10 ¹⁷
SAMPLE B		
B:I1	2.2	1.2x10 ¹⁸
B:I2	2.2	2.2x10 ¹⁸

energy was varied for each irradiation as indicated in Table 5.3 from the highest energy (2.2 MeV) down to 1.6 MeV in the fourth irradiation. The beam surface area on the diamond was kept approximately constant for each irradiation. A total charge of $\approx 23600 \mu\text{C}$ was imparted to diamond sample A with a proton current around 280-340 nA. A total proton fluence of approximately $1.0 \times 10^{18} \text{H}^+/\text{cm}^2$ was therefore imparted to the diamond. After the fourth irradiation (A: I4), diamond sample A was annealed at 800 °C in an argon atmosphere for 60 minutes and SQUID measurements acquired thereafter.

Table 5.4: Summary of irradiation parameters used at iThemba LABS for proton micro irradiation of type-IIa diamond

Region	F (H^+/cm^2)	Charge (μC)
SAMPLE 1		
A	14×10^{17}	8.1
B	10×10^{17}	7.5
C	1.1×10^{17}	2.0
D	2.1×10^{17}	4.0
E	10×10^{17}	50
SAMPLE 2		
A	0.2×10^{17}	0.021
B	0.74×10^{17}	0.078
C	2.1×10^{17}	0.2
D	8.4×10^{17}	0.9
E	3.8×10^{17}	2.2

For diamond sample B, two sets of irradiations were carried out using 2.2 MeV protons in each irradiation. As in sample A, the beam surface area was kept approximately constant for each irradiation. The proton current was kept around 400 nA.

Proton micro-irradiation of type-IIa diamond was carried out at iThemba LABS in South Africa using Oxford-type nuclear microprobe end stations with a Van der Graaf accelerator for Sample 2 and 6 MV Tandem Accelerator for Sample 1. The proton fluence and charge accumulated for each irradiation are shown in Table 5.4.

5.5 Scanning Probe Microscopy Techniques

Scanning Probe Microscopy (SPM) techniques refers to the collection of imaging techniques that utilize a sharp mechanical probe to detect local physical properties of material surfaces with nanoscale resolution to produce 3D images and facilitate quantitative and qualitative analyses of micron to nanoscale surface structures. The SPM techniques utilized in the present study include Atomic Force Microscopy (AFM), Magnetic Force Microscopy (MFM) and Electric Force Microscopy (EFM). Other commonly used SPM techniques include Scanning and Tunneling Microscopy (STM) and Kelvin Probe Microscopy (KPM).

In our studies of surface nanostructuring using Highly Charged Ions discussed in section 3.3, the impact of HCIs on atomically flat material surfaces produces spatially confined defects within \sim nm domains. The empirical characterization of these structures calls for a highly sensitive imaging technique with a spatial resolution of at least a few \sim nm. For this purpose the AFM technique is employed to characterize the surface nanostructures and in conjunction with numerical analysis methods, to ultimately carry out quantitative analysis on the interaction between the respective radiation with matter. In addition, the AFM technique has also been applied in conjunction with MFM and EFM in the imaging of microscale surface modifications following energetic proton bombardment of diamond in our studies of magnetism in carbon systems also discussed in this thesis.

5.5.1 Atomic Force Microscopy (AFM)

Since its invention by IBM scientists in 1982, the AFM technique has been successfully utilized to characterize a range of surface structures typically in the range \sim 1-1000 nm. The AFM probe constitutes of a sharp metallic pyramidal

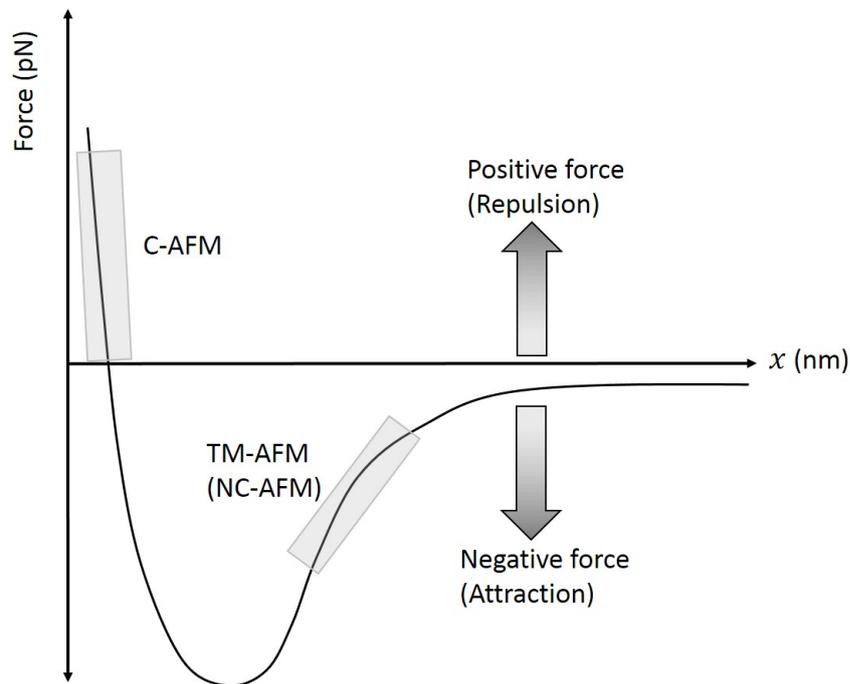


Figure 5.18: *Qualitative representation of the van der Waals interaction force dependence on the tip-sample spacing, x (nm).*

or conical tip of radius typically <5 nm mounted on a relatively elongated cantilever of length ≈ 100 - 200 nm. Atoms in material surfaces generate van der Waals forces which have a typical range of ~ 10 nm from the surface. When the cantilever is brought in close proximity to the surface within the van der Waals force field, the cantilever interacts with the force field resulting in either its attraction or repulsion to or from the surface. This interaction is empirically detected as a deflection of the cantilever measured by means of a laser system linked to a position sensitive photo diode (PSPD) and an electronic feedback control system which is ultimately digitized, processed and used to generate a 3D topography image of the surface by means of appropriate software installed on a computer. The dependence of the van der Waals force interaction on the tip-sample spacing (x) is shown in Fig.5.18.

In practice the AFM technique can be operated in different modes, the most

common being Contact Mode (C-AFM), Non-Contact Mode (NC-AFM) and Tapping Mode (TM-AFM, which is derived from NC-AFM). In TM-AFM, the cantilever is driven at or close to its resonance frequency as it rasters across the sample. Operation of the AFM in tapping mode allows the cantilever to interact primarily with attractive forces from the surface with the absence of repulsive forces by maintaining a tip-sample separation of $\sim 1-10$ nm making the technique ideal for imaging *soft* and elastic samples due to low probability of contact between tip and sample.

AFM can be used to generate topography data operating in either constant height mode or in constant force mode. In constant height mode, the spatial variation of the cantilever deflection can be used directly to generate the topographic data since the height of the scanner is fixed as it scans across the sample. In constant force mode, the deflection of the cantilever is used as input to a feedback circuit that moves the scanner up and down in the z -direction, responding to the topography by keeping the cantilever deflection constant. However, the speed of the scanning is limited by the response time of the feedback circuit but the total force exerted on the sample by the tip is well controlled. The control of tip-sample spacing during scanning is enabled by the electronic feedback control loop which typically uses either the oscillation frequency or the amplitude signal as an input.

In the current study, the Veeco Dimension 3100 AFM (see Fig 5.19) with a Nanoscope III Controller operated in Tapping Mode (TM) using amplitude feedback control under ambient conditions is used to characterize radiation induced morphological modifications as well as corresponding magnetic and electric fields (as force gradients) in diamond.



Figure 5.19: *Veeco Dimension 3100 AFM with Nanoscope IIIa Controller.*

5.5.2 Magnetic Force Microscopy (MFM)

Magnetic Force Microscopy (MFM) is a scanning probe microscopy technique derived from AFM used primarily for imaging magnetic structures. Imaging is achieved by registering the interaction between a given magnetic structure and a magnetic probe which is driven at or near its resonance frequency. Interaction of the oscillating MFM probe with the magnetic field generated from the sample under investigation results in a measurable phase shift in the oscillating cantilever. The dependence of the measured phase shift on the force gradient can be expressed as:

$$\Delta\Phi \approx \frac{Q}{k} \frac{\partial F}{\partial z} \quad (5.15)$$

where Q is the quality factor, k is the spring constant of the oscillating cantilever and \mathbf{F} is the magnetic force vector [186].

Figure 5.20 shows a schematic representation of the MFM operational principle. In the current study MFM is operated in Tapping/Lift mode. In this configuration, the magnetic contrast and topography can be distinguished. The sample is scanned twice, where the sample topography is acquired in the first sweep using the cantilever's oscillation amplitude signal for electronic feed-

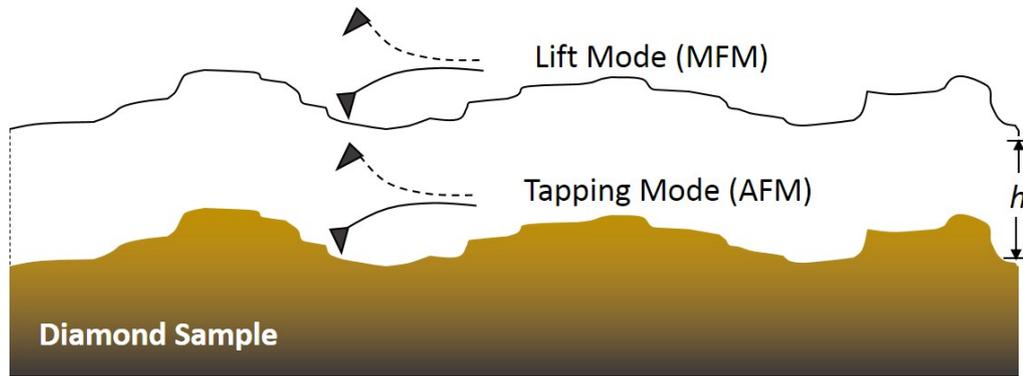


Figure 5.20: Schematic diagram representing the basic MFM principle of operation.

back control of the probe. The magnetic contrast is acquired in the second sweep where the probe is raised to a user controlled lift scan height, h (typically in the range 10-200 nm) above the sample surface. The phase shift $\Delta\phi$ or frequency shift of the magnetic probe from resonance upon interaction with the sample's magnetic field is then monitored as per eq. 5.15.

To provide a reference check for our MFM system, we scanned a platter from a standard hard disk drive in lift mode using Co/Cr coated type MESP probes under ambient conditions. An example of an MFM image with corresponding line profiles showing magnetic domains in the hard disk drive is presented in Fig. 5.21. The magnetic domains on the hard disk drive were imaged with the probe polarized in opposite directions, i.e. normal ('-1') and anti-normal ('+1') to the hard disk platter surface. Line profiles from the MFM image data were extracted from the region indicated by the dashed lines (approximately) for interpretation. As expected, scanning the hard disk drive with polarized MESP probes results in corresponding alignment of the spin in the magnetic domains. In this way, data can be read-out from the hard drive using binary configuration, i.e. sequences of '0' and '1'.

Quantitative analysis using MFM empirical data can be achieved when the magnetic properties and geometry of the tip as well as the substrate are known

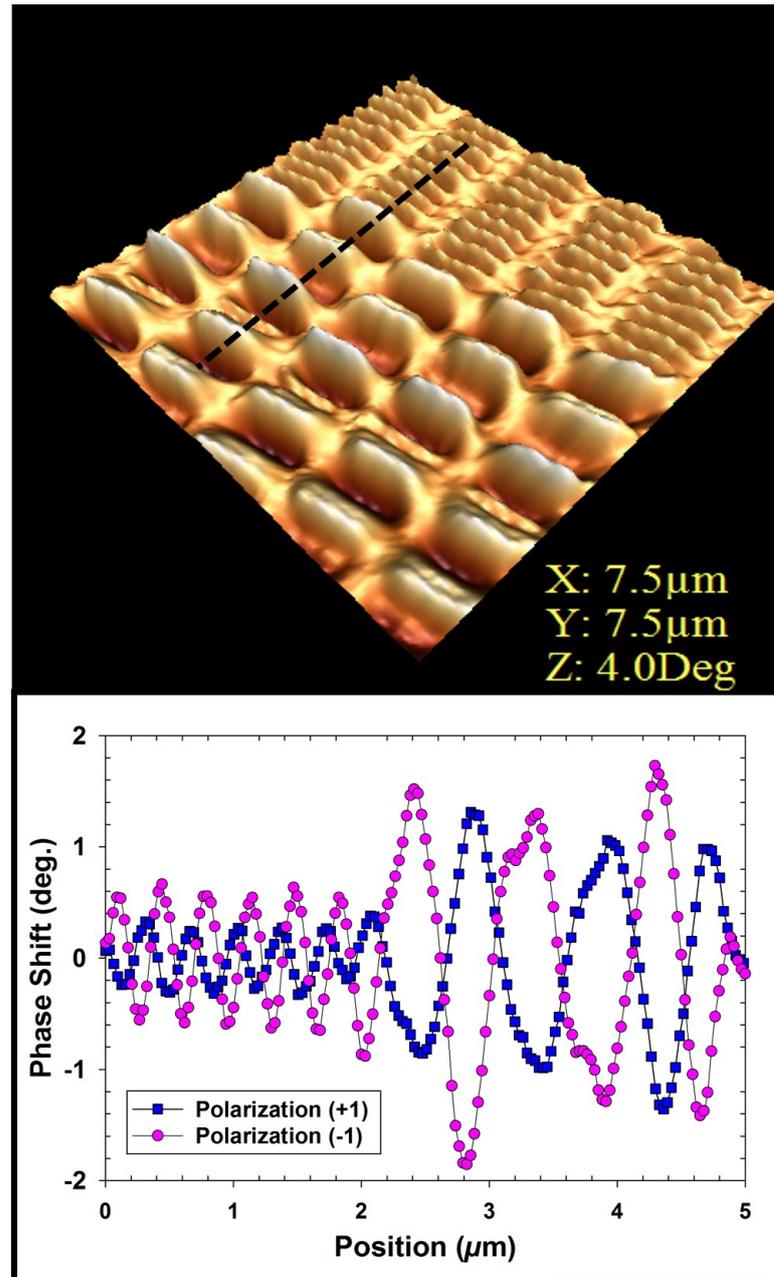


Figure 5.21: MFM image of magnetic domains on a standard computer hard disk drive platter with corresponding line profiles showing polarization dependence of the domains.

precisely in order to determine the magnetic force acting on the probe. In practice, the exact tip geometry is unknown, although reasonable approximations can be made. Nonetheless, eq. 5.15 is also useful for conducting qualitative

MFM assessment of the magnetic response from a given sample where a positive phase shift represents a repulsive force between tip and sample, and a negative force represents attraction between tip and sample relative to the background signal. The magnetic force (force gradient) is a function of the magnetic moment distribution of the tip and sample. To investigate the effect of the magnetic moment of the probe on the irradiated samples, probes of type MESP with Co-Cr coatings of high and low magnetic moments (LM, HM) as well as low coercivity (LC) probes were used for characterization.

5.5.3 Electric Force Microscopy (EFM)

EFM is a SPM technique based on the measurement of electrostatic force gradients between a conductive probe and a given sample. The instrumentation and operation principles of EFM are very similar to those of MFM with the primary difference being the origin of the detected signal (electrostatic field gradients in the case of EFM and magnetic field gradients in the case of MFM) and also the application of dc/ac voltages during EFM imaging. To a first order approximation, the force $F(z)$ detected by the oscillating cantilever at a mean distance z_0 from the surface can be written as [187]:

$$F(z) = F(z_0) + \frac{\partial F}{\partial z}(z_0)(z - z_0) \quad (5.16)$$

where $\partial F/\partial z(z_0)$ is the force gradient acting on the tip expressed in Nm^{-1} . Assuming no charge inside the ideal tip-substrate capacitance $C(z)$, the force gradient detected by the EFM probe is expressed as:

$$\frac{\partial F}{\partial z}(z_0) = \frac{1}{2} \frac{\partial^2 C}{\partial z^2} (V_{EFM} - V_S)^2 \quad (5.17)$$

where V_S is introduced to account for e.g. tip-sample work function difference and surface state, V_{EFM} is the EFM bias voltage. When the charge Q

is now introduced in the tip-sample capacitance, an effective surface potential V_Q proportional to the charge Q builds in, and the total force gradient can now be expressed as [187]:

$$\frac{\partial F}{\partial z}(z_0) = \frac{1}{2} \frac{\partial^2 C}{\partial z^2} [(V_{EFM} - V_S)^2 - 2(V_{EFM} - V_S)V_Q + V_Q^2] \quad (5.18)$$

In the present study, EFM data is acquired using conductive PtIr coated type SCM-PIT probe. For comparison with MFM data, conductive MESP type Co/Cr coated probes were also used to acquire EFM data. Results of these investigations are discussed in the following chapter.

5.6 Optical Spectroscopy

Optical spectroscopy refers to the study of the interaction between electromagnetic radiation of optical frequency range (typically spanning the near-infrared, visible and ultraviolet) with matter. Optical spectroscopies utilized in the present study are μ -Raman as well as Photoluminescence spectroscopy due to (among other practicality reasons) the optical transparency of diamond as well as the effectiveness of these techniques in probing various defects and colour centres in diamond as evidenced by literature.

5.6.1 Raman Scattering Theory

When light (electromagnetic radiation) is projected onto matter (molecules and crystals), both elastic and inelastic scattering phenomena take place. Elastic scattering phenomena known as Rayleigh Scattering dominates this interaction process accounting for over 99% scattered photons which have the same frequency ω_i as the incident monochromatic light. Less than 1% of the scattered

photons are scattered inelastically. This fraction of the interaction is due to a process known as the Raman effect after its discovery by C.V Raman in 1928 who was awarded a Nobel Prize in Physics for the discovery work in 1930. In Raman scattering, the scattered photons have a different frequency, ω_f (usually a lower frequency) than the incident photons i.e $\omega_i \pm \Delta\omega$. In molecular systems, the frequency change is typically in the energy range associated with vibrational, rotational and electronic energy levels. The Raman bands that occur at frequencies lower than ω_i , i.e $\omega_i - \Delta\omega$ are referred to as Stokes bands while those of type $\omega_i + \Delta\omega$ are referred to as anti-Stokes bands. Both Rayleigh and Raman scattering process are referred to as linear processes because during the interaction process, the intensity of the scattered radiation is directly proportional to the irradiance of the incident radiation. A schematic diagram of Rayleigh, Stokes and anti-Stokes Raman scattering is shown in Fig 5.22.

Due to the electric field intrinsic in light, interactions with molecules results in perturbation of electron densities leading charge polarization of molecules and the creation of frequency-dependent linear electric dipoles. The relation between the electric dipole vectors $\mathbf{p}^{(i)}$, the polarizability tensor $\boldsymbol{\alpha}$ of the molecule concerned, and the electric field vector \mathbf{E} of the incident monochromatic radiation of frequency ω_i is given by [188]:

$$\mathbf{p}^{(i)} = \boldsymbol{\alpha} \cdot \mathbf{E} \quad (5.19)$$

The polarizability tensor will in general be a function of the nuclear coordinates and hence the molecular vibrational frequencies. The intensity and the polarization of the scattered radiation are dependent on the observation angle because scattering occurs in a spherical geometry. Raman scattering arises from the electric dipoles oscillating at a frequency which is produced when the electric dipole oscillating at incident wave frequency is modulated by the molecule oscillating at the altered frequency. The necessary coupling between

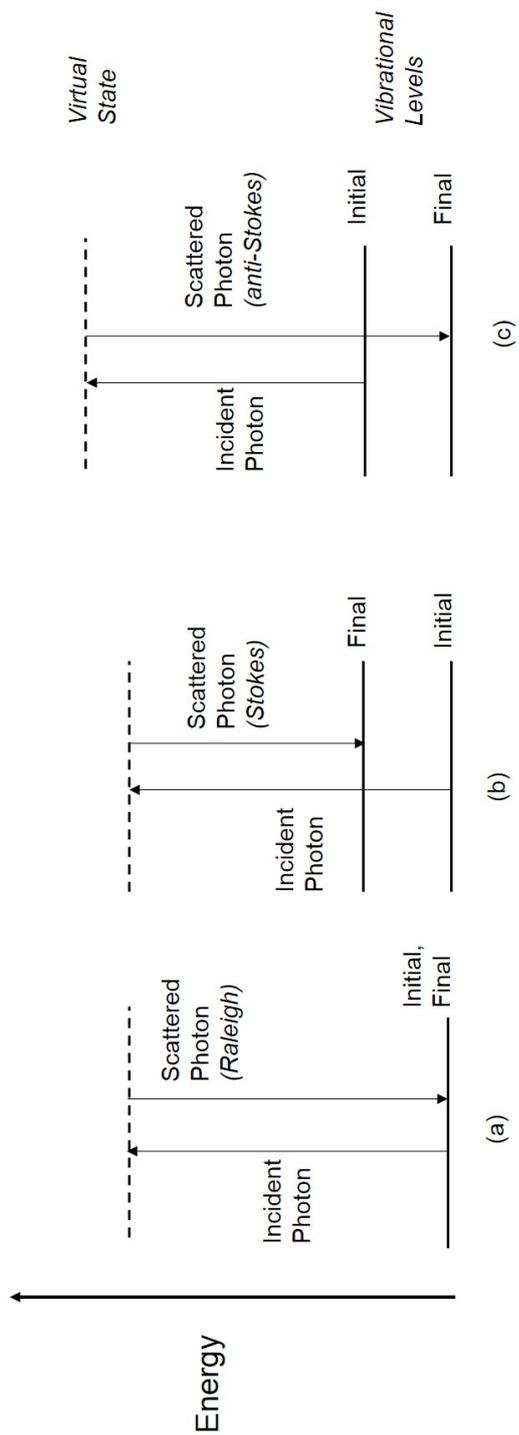


Figure 5.22: Energy level diagram showing Rayleigh (a), Stokes Raman (b) and anti-Stokes Raman scattering (c).

the nuclear motions and the electric field is provided by the electrons whose rearrangement with nuclear motion impose a harmonic variation on the polarizability. The selection rule for Raman scattering is that at least one component of the polarizability tensor with respect to the normal coordinate of vibration must have a non-zero gradient at the equilibrium position [188]. Although the classical treatment of Rayleigh and Raman scattering may be adequate in describing some aspects of the frequency dependence of linear and non-linear light scattering, its falls short of incorporating the influence of molecular properties in the system. The quantum mechanical treatment of the material system in combination with classical treatment of radiation allows for the description of all light-scattering phenomena in a satisfactory manner. The quantum electrodynamical approach involves quantization of both radiation and material properties and provides a more detailed description of light-matter scattering phenomena.

A number of light-scattering phenomena have been discovered to date including Rayleigh scattering, Raman scattering, hyper-Rayleigh scattering, hyper Raman scattering, coherent anti Stokes Raman scattering, coherent Stokes Raman scattering, and Stimulated Raman gain or loss Spectroscopy. More than 25 types of Raman spectroscopies are now known [188]. Further details on the theoretical treatment of light-scattering phenomena can be found elsewhere in literature [188, 189].

In the present study, irradiation effects in diamond are analyzed using μ -Raman Spectroscopy where the 514 nm emission line from an argon laser is used in conjunction with a Horiba Jobin-Yvon LabRAM HR Raman spectrometer. In this configuration, the incident laser beam is focused onto the samples using the Olympus microscope attachment with a 100X objective lens. The backscattered light is dispersed via a 600 line/mm grating onto a liquid nitrogen-cooled charge coupled device (CCD) detector.

5.6.2 Photoluminescence Spectroscopy

In simple terms, photoluminescence (PL) refers to the spontaneous emission of light (*luminescence*) following excitation of a given material by a monochromatic light source (e.g. a laser beam), i.e. *photo-excitation*. When a laser beam of sufficiently high energy is projected onto a sample, photoluminescence as well as Raman scattering can occur where the photoluminescence intensities are typically much higher than those from Raman scattering processes. Typical PL is composed of both fluorescence and phosphorescence processes and is a result of absorption/emission processes between different electronic energy levels in a material.

PL Spectroscopy is a non-destructive, contactless technique used for the probing the optical processes and the electronic structure of materials. The intensity and type of PL observed depends on the laser energy and properties of the material under investigation. Excitation of the electronic system in a target material such as diamond ($E_g \approx 5.5$ eV) using a laser beam with energy $h\nu > E_g$ results in the creation of electron-hole pairs. Recombination of electron-hole pairs takes place through various recombination paths some of which result in the emission of light as electrons return to their ground state.

For $h\nu < E_g$, no electron-hole pairs are created. However, optical centres can be excited using energies in the absorption band $h\nu < E_g$, which de-excite or relax to the ground state after a short time, emitting light in the luminescence sideband. With the exception of edge luminescence and band A luminescence, all of the different luminescence bands are associated with vibronic centres which have their ground state and excited energy levels situated in the forbidden energy gap between the valence and conduction bands (see Fig. 5.23) [190].

The emitted optical signal is channeled through to a spectrometer where

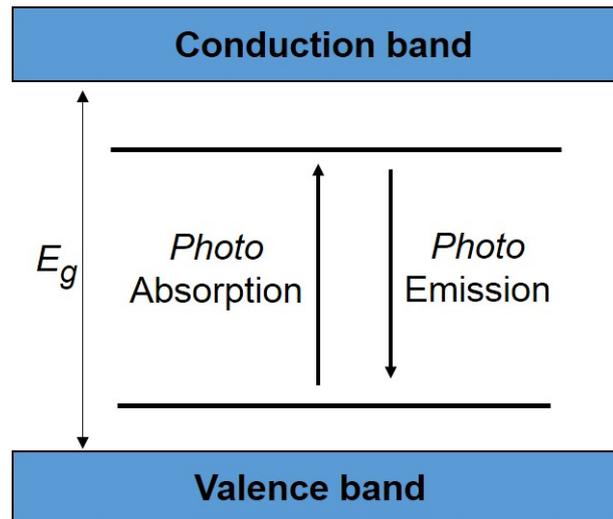


Figure 5.23: *Simplified energy level scheme showing excitation of vibronic centres.*

the light dispersed using e.g. a diffraction grating which *separates* the optical signal into wavelength dependent intensities which are then typically channeled through a photomultiplier tube to enhance the signal to noise ratio. The resolution, R , of a grating monochromator is a measure of its ability to separate two closely spaced spectral lines. The Rayleigh criterion states that two wavelengths, λ_1 and λ_2 , are resolved if the central maximum of one line falls on a diffraction minimum of the other and is expressed as [191]:

$$R = \frac{\lambda}{\Delta\lambda}. \quad (5.20)$$

In practice the resolution depends on several parameters including the resolving power of the grating, system focal length and slit width of the spectrometer. Therefore the resolution of a spectrometer will be the FWHM of a single monochromatic spectral line which is inversely proportional to temperature. Most of the absorption bands in diamond extend into the ultraviolet spectra region, therefore UV excitation is required to observe the corresponding PL signatures which result in photo-emission in the visible spectral region.

In our investigations of irradiation effects in diamond, photoluminescence (PL) spectroscopy spanning the near-infra red (NIR) to ultra-violet (UV) frequencies is carried out using a 40X UVB microscope objective lens from Thor Labs following electromagnetic excitation using a 244 nm UV probe, at room temperature.

5.7 The Superconducting Quantum Interference Device (SQUID)

The Superconducting Quantum Interference Device (SQUID) is an ultra high sensitivity magnetic sensor which primarily measures magnetic flux and the output voltage signal. In essence, the SQUID device can be described as a superconducting loop interrupted by one or more Josephson junctions. SQUIDs with a single junction are also known as RF-SQUIDs while those with double junctions are known as DC-SQUIDs. Two fundamental properties of superconductors are exploited in the fabrication of standard SQUID magnetometers, namely the Josephson effect and flux quantization. The Josephson Effect was initially predicted by Brian Josephson in 1962 [192], which essentially implies that under zero applied voltage, Cooper electron pairs between two superconductors should tunnel through an insulating barrier in a resistance-less supercurrent. Feynman later provided a more widely used theoretical formalism of the Josephson Effect [193].

The requirement for flux quantization is that the magnetic flux enclosed by superconducting loop be quantized in units of the flux quantum $\Phi_0 \equiv h/2e \approx 2.07 \times 10^{-15} \text{ Tm}^2$ where $h \equiv 2\pi\hbar$ is Planck's constant and e is the electron charge. This quantization manifests because the phase of cooper pairs in the superconductor is coherent. SQUID magnetometers therefore present a macroscopic manifestation of quantum effects i.e. quantum mechanical tunneling of

macroscopic wavefunctions through a sufficiently thin insulating barrier and corresponding quantum interference.

It can be shown from the Bardeen-Cooper-Schrieffer (BCS) theory of Superconductivity that electrons in the superconducting state form correlated pairs of electrons with opposite spin and momentum (Cooper pairs) whose coherence length is sufficiently large that they overlap. The relative phase factors of the wavefunctions of each pair match and result in a coherent phase throughout the superconductor. Using the Feynman formalism, we can thus describe the Cooper pairs with a macroscopic wavefunction of the form [193, 194]:

$$\psi = |\psi(\mathbf{r})| e^{i\mathbf{K}\cdot\mathbf{r}} \quad (5.21)$$

where \mathbf{K} is the net wave vector of all cooper pairs and $|\psi(\mathbf{r})|$ is the ensemble-average function when $K=0$. The quantity $\mathbf{K} \cdot \mathbf{r}$ is the position dependent phase of the macroscopic wavefunction which can be written as $K \cdot r = \theta(r)$. The wavefunction can be normalized such that $\int_V \psi^* \psi dr = N$, the total number of electron pairs in the superconductor. The wavefunction may therefore be written as:

$$\psi = \sqrt{n(\mathbf{r})} e^{i\theta(r)} \quad (5.22)$$

where $n(\mathbf{r})$ is the local Cooper pair density (which is approximately spatially invariant in weak fields).

Most SQUID magnetometers are made of a low transition temperature (T_C) superconductor Nb and are operated at or below the boiling point of liquid helium (4.2 K). A Josephson junction consists of two weakly coupled superconducting electrodes separated in the case of low- T_C tunnel junction by a thin (~ 10 nm) insulating barrier. The voltage across the Josephson junction remains zero when DC current is applied across it, up to a current value called

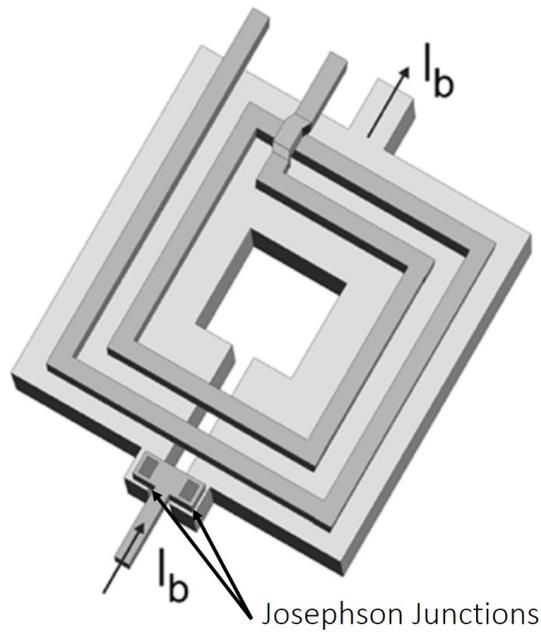


Figure 5.24: Schematic diagram of a low- T_c dc SQUID with integrated input coil [195].

the Josephson critical current I_0 due to the cooper pair tunneling through the barrier/junction (Josephson effect).

The cooper pairs tunneling through the barrier develop a supercurrent $I = I_0 \sin\delta$ where δ is the difference between the phases of the order parameters in the two superconductors. For zero applied current, the two electrodes are coupled by an energy $I_0\Phi_0/2\pi$. In the absence of thermal fluctuations, the voltage V across the barrier is zero for $I < I_0$; for $I > I_0$, a voltage is developed and δ evolves with time as $\dot{\delta} = 2\pi V/\Phi_0$.

For low- T_C junctions, the I - V characteristics are well explained by the Resistively and Capacitatively Shunted Junction (RCSJ) model. For SQUIDS one generally needs nonhysteretic I - V characteristics, a requirement that is met if $\beta_c \equiv 2\pi I_0 R^2 C/\Phi_0 \leq 1$ [195]. Virtually all low- T_C dc SQUIDS used today involve Nb- AlO_2 -Nb Josephson junction technology and a thin-film Nb planar square washer, (Fig. 5.24) [195].

SQUID magnetometers have been widely employed in numerous applications including heart and brain magnetic signal detection [196], detection of axion dark matter [197], the dynamical Casimir effect [198] and the Majorana fermions [199]. A comprehensive review of SQUIDs and their applications can be found elsewhere [200–202].

In the current study, characterization of intrinsic and extrinsic defects was achieved by means of a commercial SQUID magnetometer from Quantum Design operated using the reciprocating sample option (RSO). The primary magnetic field was applied perpendicular to the $\langle 001 \rangle$ crystallographic axes in all measurements. Both isomagnetic (with temperature cycled between 4.2 and 350 K) and isothermal (with the field cycled between ± 2 kOe) measurements were carried out. The sensitivity of the SQUID magnetometry system in RSO mode is enhanced from $\sim 1 \mu\text{emu}$ to $\sim 0.02 \mu\text{emu}$ and can thus adequately measure the effects of ion irradiation in the diamond samples. The diamond samples were mounted using thermal varnish onto gold-coated quartz sample holders (see Fig. 5.2) that fit into both the irradiation target chamber as well as into the SQUID system for the purpose of minimizing sample handling and ensuring reproducibility in measurements.

Chapter 6

Results and Discussions

The results of the current investigation and discussions thereof are addressed in this section. First we address the outcomes from our investigations of surface nanostructuring using highly charged ions (HCIs) in type Ib diamond [203]. In the later part of this chapter we address the outcomes from the investigations of magnetic effects following energetic proton irradiation in ultra pure type IIa diamond [204]. Related magnetism studies were also carried out in nitrogen rich type Ib diamond [205]. However, in this thesis we report only on the studies in ultra pure type-IIa diamond. As discussed earlier, two approaches are adopted in our carbon magnetism studies, namely micro and macro irradiation of diamond using energetic protons. Both approaches are reported and interpreted in the later part of this chapter.

6.1 SHCI Impact on Diamond Surfaces

Bismuth SHCI beams were produced using the Electron Beam Ion Trap (EBIT) facility at Max Planck Institute for Nuclear Physics in Heidelberg, Germany [206, 207]. By appropriately controlling the High Voltage deceleration stage, extraction voltages between 400 V and 900 V were achieved to obtain cor-

responding kinetic energies ranging from 20 keV to 48 keV on target. Five charge states of Bismuth from $q=50+$ to $q=62+$ were produced corresponding to potential energies ranging between 49 keV and 110 keV with fluences $\approx (1-5) \times 10^9$ ions/cm² (see Table 5.1).

Xenon SHCI beams were produced using an Electron Cyclotron Resonance (ECR) source at GANIL in France [208]. An ‘intermediate’ range of Xenon SHCIs with charge states ranging from $q = 20+$ to $q = 31+$ was extracted at ≈ 15 kV resulting in kinetic energies on the target of $\approx 300-465$ keV with fluences $\approx (1-100) \times 10^9$ ions/cm². All HCIs utilized in the present study are SHCIs since the maximum impact velocity is $\approx 0.4v_{\text{Bohr}}$. The corresponding potential energies obtained ranged between 4 keV and 18 keV (see Table 5.2). The energy density imparted by the SHCIs to the surface is of the order $\sim 10^{14}$ W/cm².

Post irradiation surface characterization of the diamond surfaces was conducted at the University of the Witwatersrand in South Africa by means of AFM analysis using the Veeco dimension 3100 AFM with a Nanoscope IIIa controller. The system was operated in Tapping Mode (TM) using amplitude feedback control under ambient conditions. High resolution TM probes were mounted for improved imaging and sensitivity. Topography, Amplitude and Phase signals were simultaneously acquired to assess the correlation of observed nanodefects. Several nanodefects per image were analyzed to improve statistics and reduce sources of error.

6.1.1 Experimental Results

Fig. 6.1 shows a Tapping Mode AFM topography image acquired over type Ib diamond (111) symmetry plane before irradiation together with a line profile extracted from the image data. A 250 nm x 250 nm scan size was captured at room temperature. The surface roughness (rms) of the pristine diamond was $R_q \approx 0.17$ which highlights the atomic flatness of the terraces on the

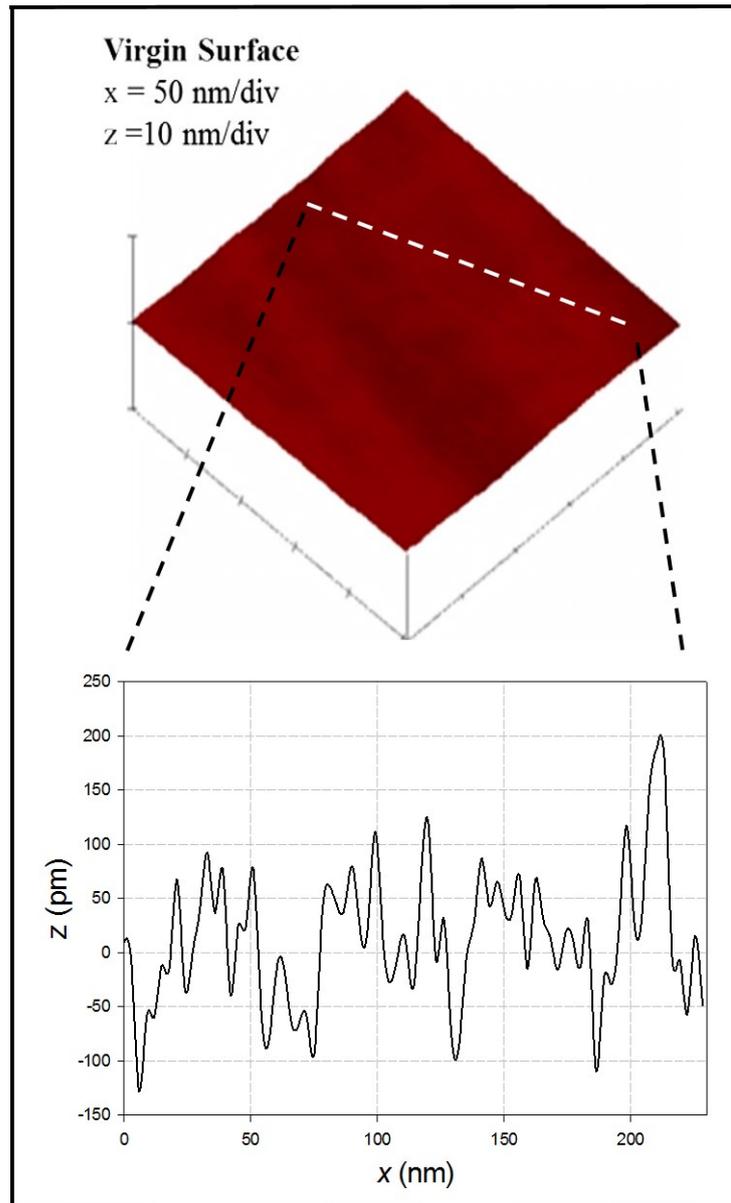


Figure 6.1: *TM-AFM topography image showing the pristine atomically flat diamond (111) surface together with a line profile extracted from the image data represented by the dotted lines.*

diamond (111) plane. Following irradiation with SHCIs at different potential and kinetic energies, nanoscale morphological modifications are created in the diamond surfaces, for all charge states and ion species utilized. For brevity, we present results for ≈ 169 eV/amu Bi^{59+} and ≈ 3.5 keV/amu Xe^{31+} in Fig. 6.2.

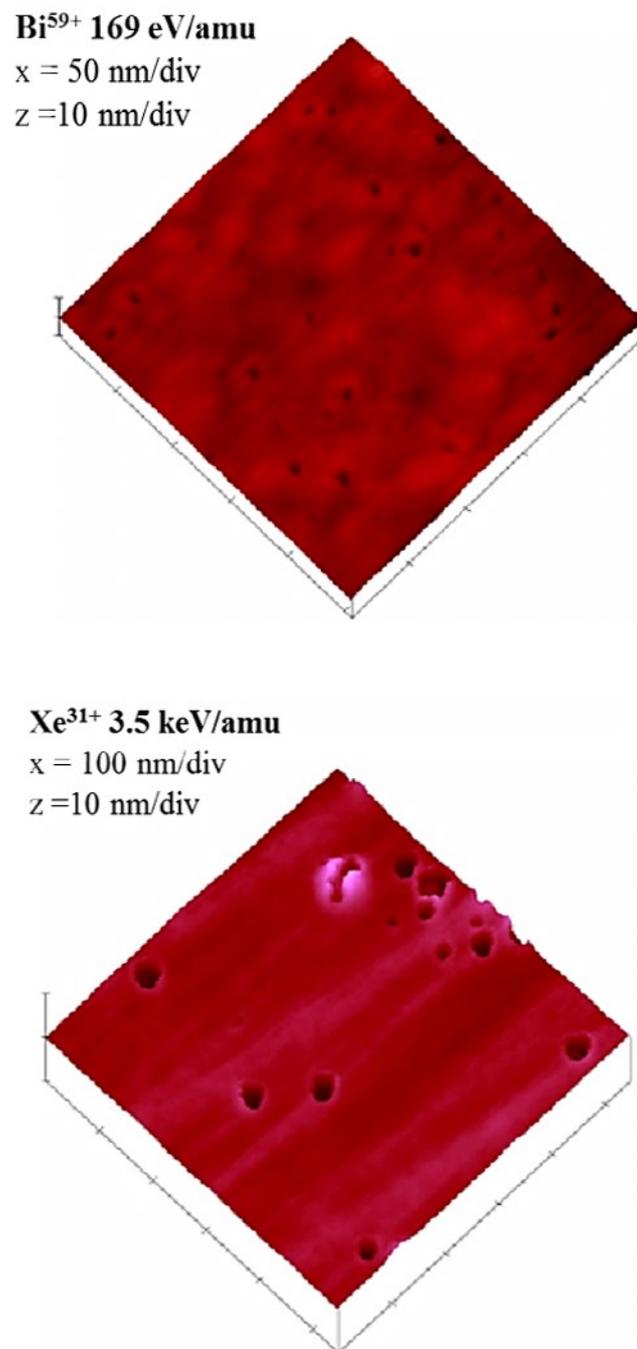


Figure 6.2: Examples of TM-AFM topography images showing diamond (111) surfaces after irradiation with Bi⁵⁹⁺ and Xe³¹⁺ SHCIs.

The acquired images are analyzed according to observed defect densities, defect dimensions and morphology with respect to laboratory parameters such

as extraction voltage and fluence. As seen from Fig 6.2, impact of SHCI on the diamond surface creates nanoscale crater-like depressions onto the diamond surfaces that have diameters up to ≈ 27 nm on average for the investigated SHCIs. Measurement of the depth of the nanocraters is only practical for craters of sufficiently large diameter and requires probes of very small diameter (e.g. carbon nanotube type probes) as this will reduce the effect of imaging artefacts. We therefore focus our discussions on the defect diameters.

In general, the number of nanoscale defects (*nanocraters*) observed by AFM should be consistent with the irradiation fluence and should scale down accordingly assuming a normal distribution of ions and a defect formation probability of ≈ 1 . Given experimental uncertainties such as beam continuity and distribution as well as possible space charge effects on the diamond surface, the ratio of observed craters to the experimental fluences converges towards one to one.

To highlight the surface morphology of the nanocraters, we extracted line profiles from the Bi^{59+} topography signal in Fig 6.2 across several different nanocraters and the resulting plot thereof is shown in Fig 6.3.

Fig 6.4 shows TM AFM analysis results from the interaction of the produced SHCIs with the (111) diamond crystal plane as a function of the potential energy (and charge state). For each charge state, several nanocraters were characterized and analyzed using AFM to improve statistics and to estimate the statistical error $\delta = \sqrt{\sigma/n}$, where σ and n are the standard deviation and the number of nanocraters respectively. The statistical errors are represented by the error bars in Fig. 6.4. Both Xenon and Bismuth SHCI induced nanocraters show a direct proportionality in diameter with respect to potential energy and charge state q as expected. However, a significant difference in the gradient of the trend between Xenon and Bismuth SHCI induced nanocrater diameters is evident in Fig 6.4. The difference in the gradients can be attributed to the difference in the kinetic energy of the produced SHCIs. The

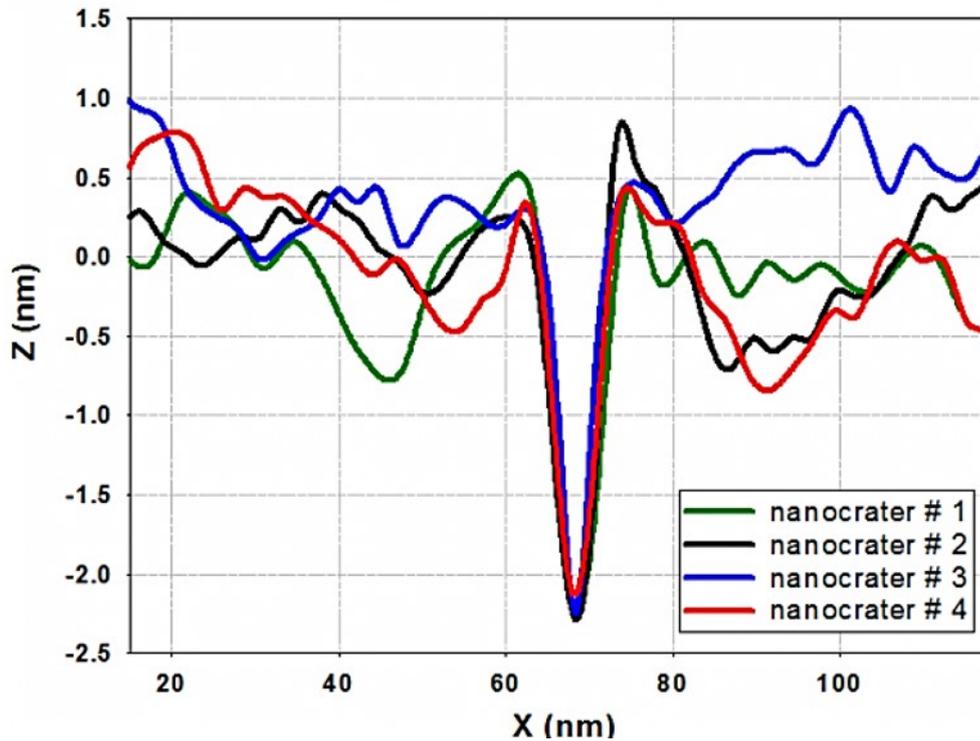


Figure 6.3: Topography line profiles extracted from the Bi^{59+} topography image in Fig 6.2 showing crater-like morphology of the induced nanoscale defects.

Xenon SHCIs used in our experiments carry ~ 10 times more kinetic energy than the Bismuth SHCI. This larger Xenon kinetic energy will also result in higher kinetic sputtering in diamond compared to Bismuth.

The sputtering of surface atoms by Xenon SHCIs vary significantly between materials and can be as large as $500 \text{ amu} \cdot \text{ion}^{-1}$ in some materials [116, 209, 210]. The overall sputtering observed following SHCI impact thus probably results from a synergistic interplay of kinetic and potential energy. Although it has been shown that SHCI potential sputtering plays a more significant role towards defect formation in many materials, the enhancement of nano-crater diameters by kinetic sputtering in diamond is also signified by the observed ‘overlap’ in nano-crater diameter as a function of potential energy.

The dashed line in Fig 6.4 is drawn to show that nano-craters of similar

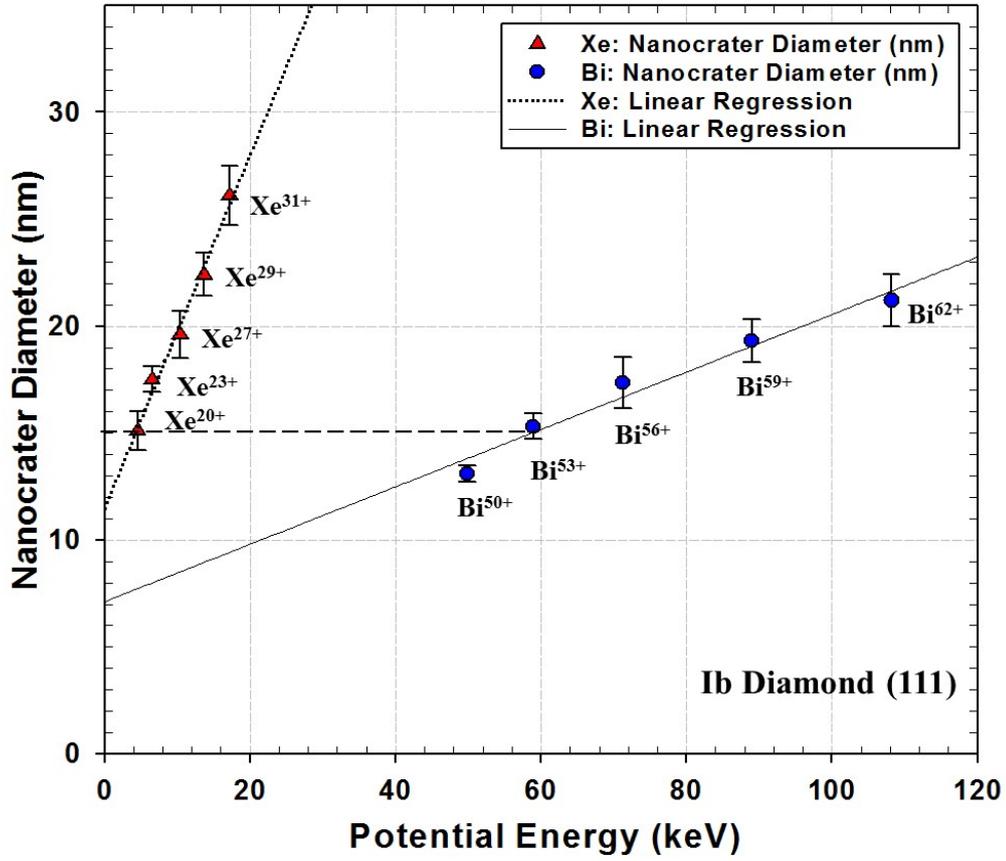


Figure 6.4: Potential energy dependence of Bismuth and Xenon SHCI induced nano-crater diameter in insulating type Ib diamond (111) crystal planes.

average diameter can be produced using SHCIs of different potential energy with sufficiently different kinetic energy. It is also interesting to note that the ‘energy quotient’, E_{kin}/E_{pot} (i.e. kinetic energy/potential energy) varies significantly between Bi and Xe SHCIs. In the case of Xe we have $26 < E_{kin}/E_{pot} < 66$ whereas in the case of Bi we have $0.3 < E_{kin}/E_{pot} < 0.7$. The energy quotient for Xe SHCIs is ≈ 80 -100 times larger than for Bi SHCIs. This relation between the energy quotient and the observed nanod defect diameter provides evidence of a synergistic interplay between the SHCI potential and kinetic energy in nanod defect formation in diamond.

Assuming a linear relationship between nano-crater diameter and potential

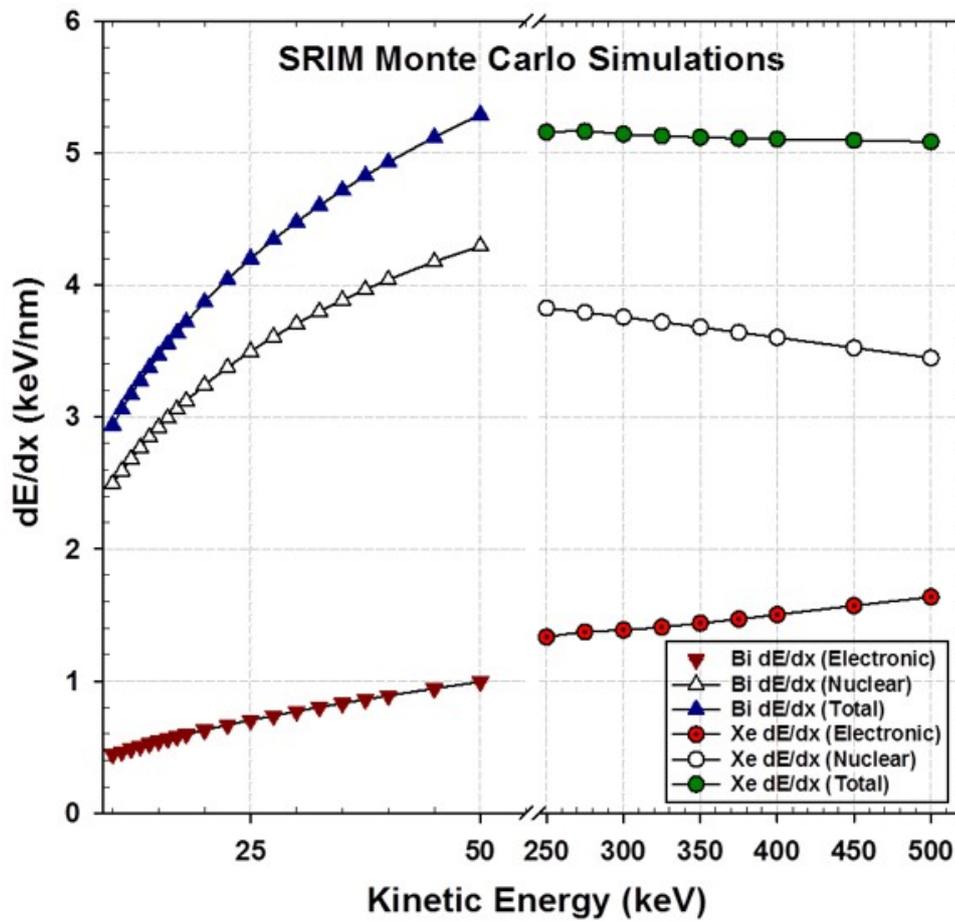


Figure 6.5: SRIM Monte Carlo simulations showing the stopping of Xenon and Bismuth ions in diamond as a function of the ion kinetic energy.

energy and neglecting possible threshold effects, the linear regression of TM AFM data in Fig 6.4 calculated using the least squares method show that even for zero potential energy, a non-zero crater diameter might be observable. This suggests that the kinetic energy of the SHCIs utilized in the present study, may be above the kinetic energy threshold for nanoscale surface defect formation in type Ib insulating diamond. Nonetheless, such extrapolation requires further empirical data towards zero potential energy for validation.

Fig 6.5 shows SRIM Monte Carlo simulations of the stopping powers of Xenon and Bismuth ions in diamond. As usual SRIM calculations only consider neutral projectiles of a certain kinetic energy [211]. The stopping of *slow* ions

used in the present study with kinetic energy ranging between 0.144 keV/amu and 3.55 keV/amu is dominated by nuclear stopping. While total stopping of Bismuth ions in diamond increases with increasing kinetic energy, the Xenon total stopping is more or less constant in the explored kinetic energy range. Xenon SHCIs induce higher thermal excitation of the diamond electronic system due higher kinetic energy transfer than Bismuth ions. This energy is exchanged with the lattice system via electron-phonon coupling. Since diamond has a large mean free path, *hot* electrons can travel relatively large distances in the diamond lattice. This kinetic energy exchange together with potential energy effects discussed above may have the effect of enhancing dilation of the observed Xenon single ion impacts sites. The interplay of charge state and momentum has been observed previously for sputtering and secondary ion formation studies in metal oxides by SHCIs where elastic collision spikes and intense electronic excitation combine synergistically [212].

It has been shown that the formation of surface nanodefects by SHCI impact requires potential energy in excess of the potential energy threshold [213]. However, Fig 6.4 also shows that for the kinetic energy range explored in type Ib diamond (111), reducing the SHCI potential energy below the potential energy threshold could still result in observable nanoscale surface modifications. Nanometric surface modifications using \sim keV kinetic energy with singly charged ions have been observed in several other materials [214–216].

Therefore, to empirically investigate the true potential energy effect in nano-crater (nanodefekt) formation, it will be necessary to reduce the kinetic energy below the kinetic energy threshold for nanodefekt formation in that specific material. However, decreasing the either the kinetic or potential energy may result in increasingly smaller nano-crater diameters. This may pose a challenge for characterization of the nano-craters since the nominal radius of curvature of most high resolution commercially available AFM probes is $\approx(2-8)$

nm. When the nano-crater diameter approaches the nominal tip radius of curvature, aliasing of the surface feature may occur resulting in poor characterization. Appropriate surface imaging techniques are therefore necessary to adequately sample morphological trends at or near the potential (and kinetic) energy threshold for nanodefekt formation in insulating type Ib diamond (and similarly for other relevant materials).

6.2 Proton Induced Evolution of Magnetic and Optical Properties

6.2.1 Monte Carlo Simulation

The Stopping and Range of Ion in Matter (SRIM) Monte Carlo simulations [211] was used to provide estimates of radiation damage by calculating the range, distribution and density of defects (vacancies) created by proton irradiation as a function of the ion energy, ion fluence, material properties and dimensions. In this way the average spacing between vacancies (inter-vacancy spacing) can be controlled which is reported to be a critical parameter in triggering various forms of magnetism, e.g. paramagnetism [25], ferro (ferri) [217] magnetism in carbon systems.

In estimating the kinetic energy effects of irradiation in diamond, we account for the radiation hardness of diamond by using a displacement energy of 45 eV [218, 219] as an input in SRIM simulations. In Fig.6.6 the range of 2.2 MeV protons in diamond is estimated using SRIM Monte Carlo simulations using a diamond density $\rho = 3.52 \text{ g/cm}^3$. The EOR (end of range) of 2.2 MeV proton in diamond is estimated to be $\approx 29 \mu\text{m}$ from the irradiated surface of the diamonds. At this energy, an average of ≈ 11 vacancies/ion are produced from the kinetic effects of irradiation. The SRIM collision events showing the

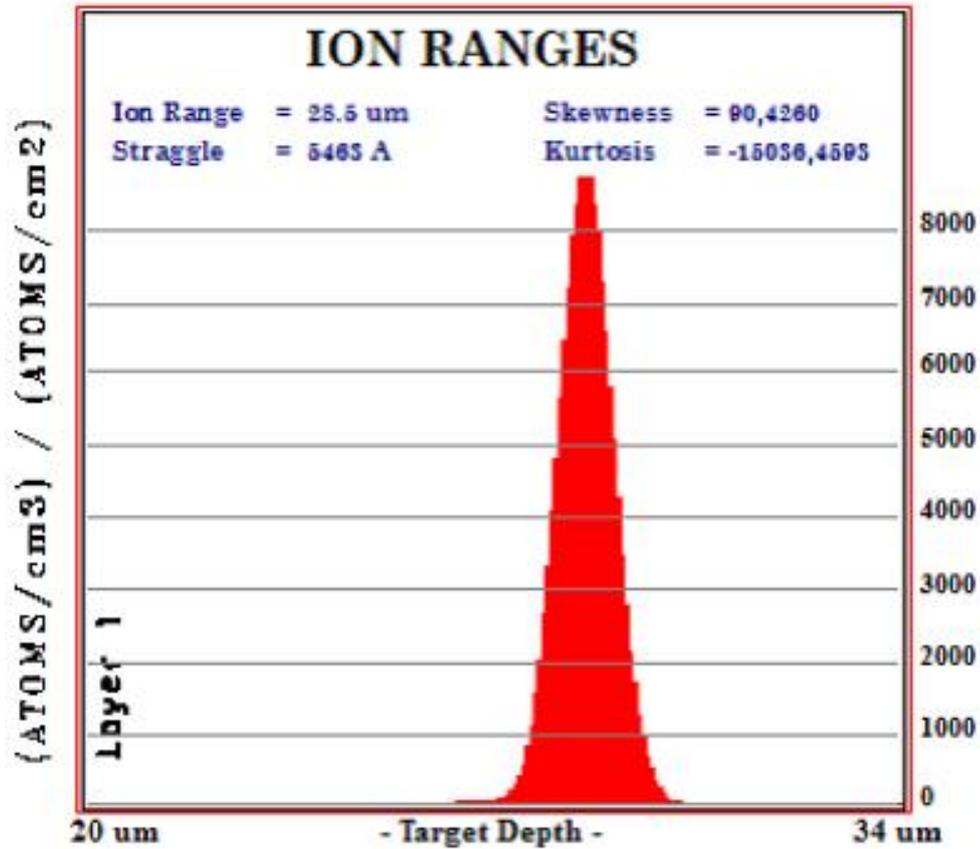


Figure 6.6: SRIM ion range estimates for 2.2 MeV protons in diamond.

target displacement, target Vacancies and replacement collisions are shown in Fig.6.7. Irradiation parameters calculated from the simulated SRIM collision events (Fig.6.7) are shown in Table 6.1.

Following Ramos *et al.* [31], the average volume per vacancy can be written as $v_{vac} = d_{vac}^3$. The vacancy density in the main irradiation area $1/v_{vac,peak}$ is approximately one half of its maximum value at the peak (the maximum damage occurs near the end of range of the energetic protons). If F is the irradiation fluence, we have $F [\text{ions}/\text{nm}^2] \times P/2 [\text{vacancies}/\text{ion} \cdot \text{nm}] = (\text{No. of vacancies})/\text{nm}^3 = 1/v_{vac,peak}$. We therefore have:

$$d_{vac,peak}^3 = 1/[F \cdot P/2]. \quad (6.1)$$

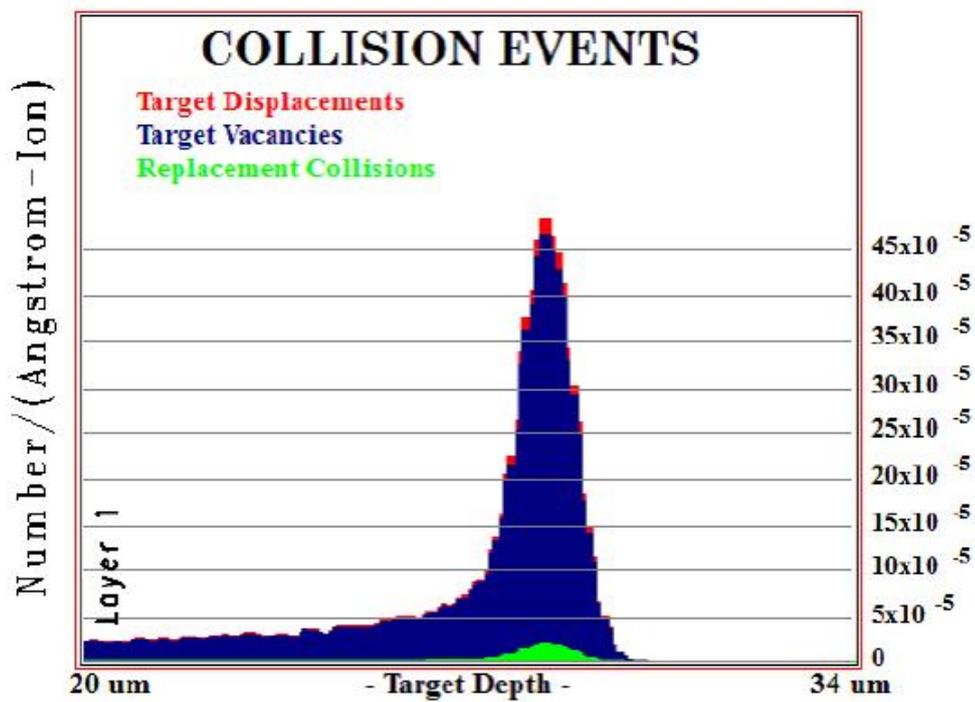


Figure 6.7: SRIM Collision Events for 2.2 MeV protons in diamond.

Table 6.1: SRIM based calculation of irradiation parameters, where P , M and S represents the vacancies/ion-nm at the peak, middle and ‘surface’ of the calculated SRIM vacancy distribution

Energy (MeV)	2.2	2.0	1.8	1.6	1.4
Ion Range (μm)	28.5	24.3	20.4	16.9	13.6
L. Straggle (μm)	0.55	0.47	0.41	0.34	0.27
Vacancies/ion	11.1	11	10.2	10	9
P(vac/ion·nm)	4.6×10^{-3}	5.3×10^{-3}	6.2×10^{-3}	6.9×10^{-3}	8.0×10^{-3}
M(vac/ion·nm)	1.5×10^{-4}	1.6×10^{-4}	1.8×10^{-4}	2.1×10^{-4}	2.4×10^{-4}
S (vac/ion·nm)	0.6×10^{-4}	0.8×10^{-4}	0.8×10^{-4}	0.9×10^{-4}	1.2×10^{-4}

Therefore using the irradiation data in Table 6.1 for the diamond samples, we can calculate the average intervacancy distance, both around the peak region, $d_{vac,peak}$ and closer to the surface (in the first micrometer) $d_{vac,surf}$

using the corresponding equation $d_{vac,surf}^3 = 1/[F \cdot S]$, we thus have irradiation parameters as per Table 6.2:

Table 6.2: *Irradiation parameters deduced from laboratory and SRIM-based estimates.*

SAMPLE	A	B
F [ion/nm ²]	3800	10000
Q_{total} (μ C)	7350	23600
N_{vac} (total number of vacancies)	5.1×10^{17}	1.63×10^{18}
$d_{vac,peak}$ (nm)	0.485	0.352
$d_{vac,surf}$ (nm)	1.64	1.19

6.2.2 Macro-irradiation Investigations

The pristine (unirradiated) diamond samples A and B both revealed a linear diamagnetic background that remains essentially invariant in the temperature range 4.2-300 K with magnetic susceptibility values of -4.8×10^{-7} emu/g and -5.0×10^{-7} emu/g respectively. The respective magnetic susceptibility values were found to be in close comparison with values reported in literature [220]. The diamagnetic background for diamond samples A and B measured at 300 K and 4.2 K is shown Fig. 6.8. All SQUID measurements reported herein were acquired with the primary field applied perpendicular to the $\langle 001 \rangle$ crystallographic axes.

Fig. 6.9 shows the magnetic moment of both diamond samples, before and after irradiation (and annealing), measured at 300 K. The diamagnetic backgrounds of the pristine samples (see Fig. 6.8) were subtracted from the post irradiation data for the respective samples. In all cases the acquired data

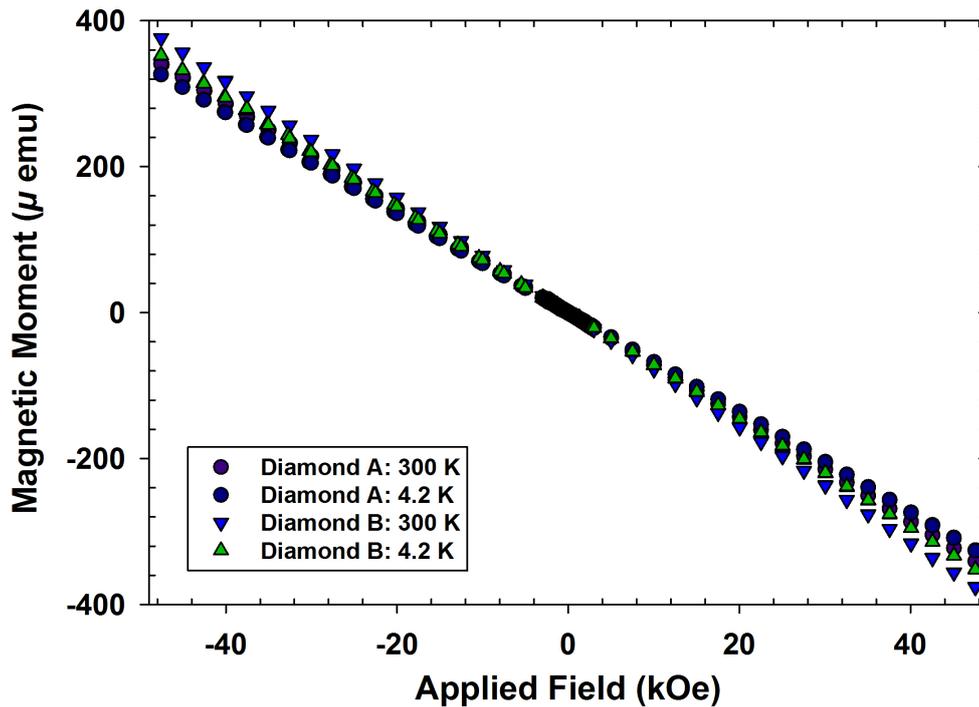


Figure 6.8: *Linear diamagnetic background of pristine diamond samples A and B acquired at 4.2 K and 300 K.*

exhibits an s-like curve behaviour with saturation magnetization $\approx 0.5 \mu\text{emu}$ for sample A and $\approx 1.5 \mu\text{emu}$ for sample B at 300 K.

A narrow hysteresis is observed (see Fig.6.9 inset) with a remanence of $\approx 0.2 \mu\text{emu}$ and coersivity of 0.1 kOe indicating superparamagnetic (SPM) behaviour both before and after irradiation at 300 K, as well as after annealing sample A at 800°C in an argon atmosphere. The observed SPM therefore is not irradiation induced but rather originates from traces of ferromagnetic impurities in the diamonds such as Ni and Cr used as catalysts in the CVD diamond synthesis process. The true effects of irradiation and annealing are observed in Fig.6.10 where the corrected magnetic moment of diamond following the different irradiation stages (and annealing) is measured as a function of the applied field at 4.2 K.

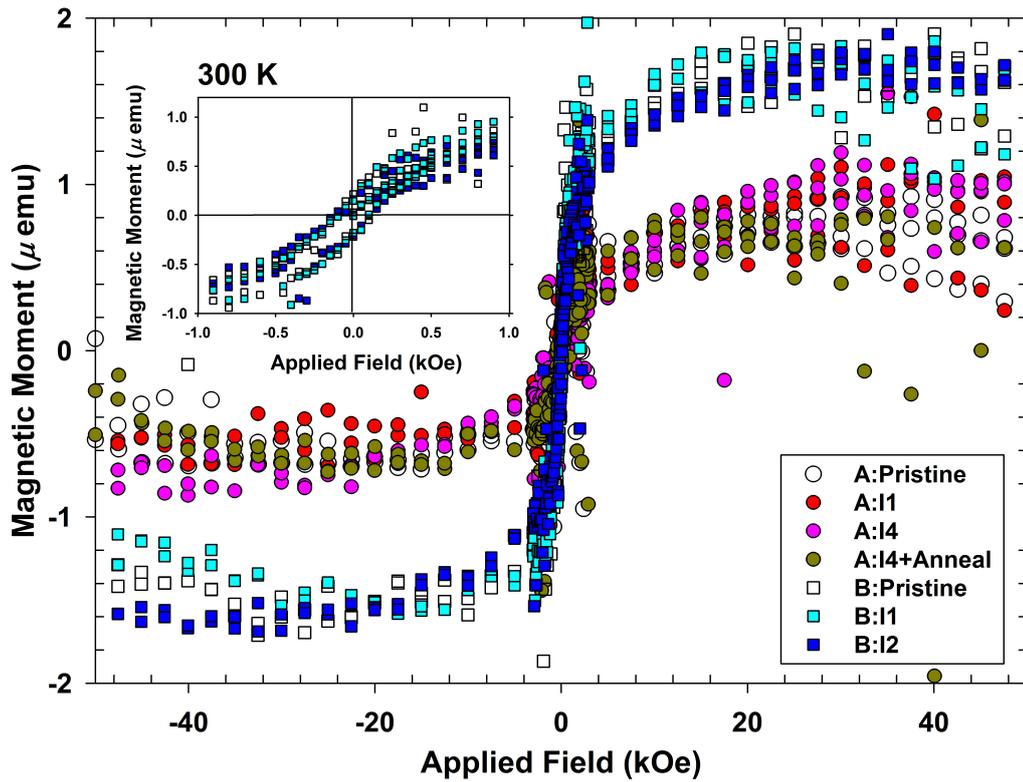


Figure 6.9: Magnetic moments of diamond samples A and B acquired at different irradiation and annealing stages as function of the applied field at 300 K.

The magnetic effect of annealing illustrated in Fig.6.10 is primarily a reduction in the paramagnetic contribution of proton irradiation in diamond. While vacancies are immobile at room temperature, both intrinsic and extrinsic interstitials are mobile due to their relatively low migration barrier in diamond. At the annealing temperature (800 °C) however, both vacancies and interstitials are mobile thus increasing their recombination probability. The recombination is only partial since the paramagnetic contribution of defects following annealing is still greater than that produced by defects in stage A: I1 before annealing as shown in Fig.6.10. The overall system of defects created by irradiation remains primarily paramagnetic even after annealing with no evidence of long range magnetic ordering at 4.2 K.

Fig.6.11 shows the temperature dependence of the net magnetic moments

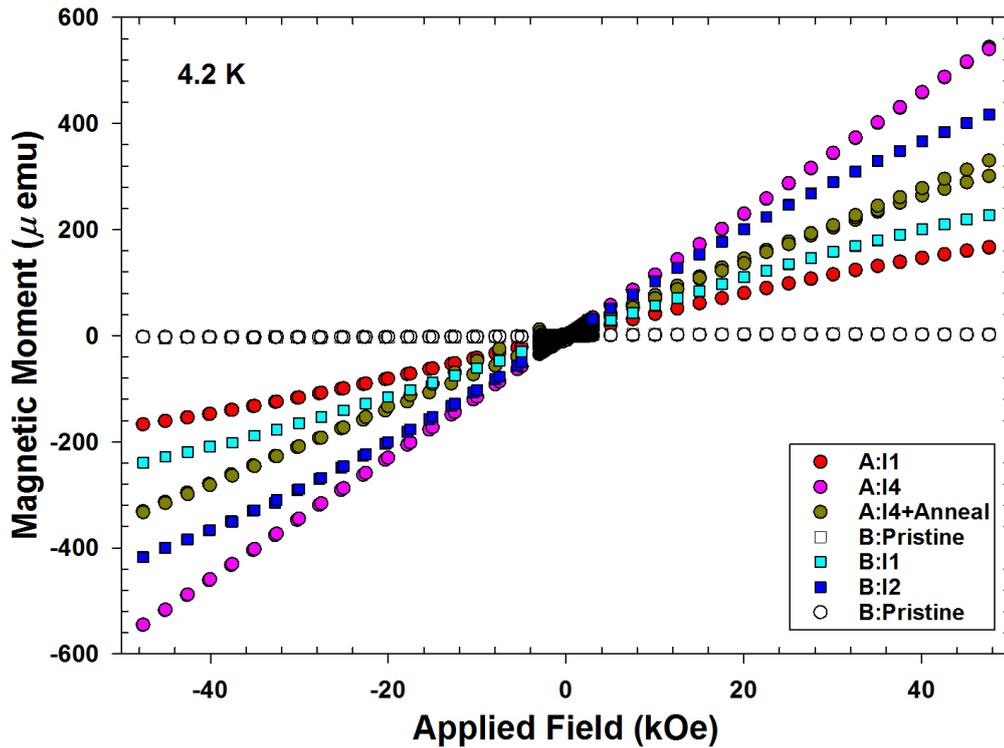


Figure 6.10: *Magnetic moments of diamond samples A and B acquired at different irradiation and annealing stages (see Table.1) as function of the applied magnetic field at 4.2 K*

of samples A and B after irradiation (and annealing) at a constant magnetic field of 2 kOe. In all the data presented, the net magnetic moment for all irradiations is inversely proportional to temperature. The qualitative nature of the temperature dependence of the measured magnetic moment is indicative of Curie type paramagnetism. However, a difference is noted in the ‘A:I4 + Anneal data’. The data appears to be superimposed on a constant magnetic signal of $\approx 6-7 \mu\text{emu}$, independent of temperature. In addition, a minor peak is noted around 40-50 K in the post anneal data.

Various texts attribute such temperature independent magnetic moment to paramagnetism [221] or diamagnetism in the material. However, temperature independent ferromagnetism has been reported in various texts including carbon [26] and Co doped ZnO [222]. In the former, temperature independent

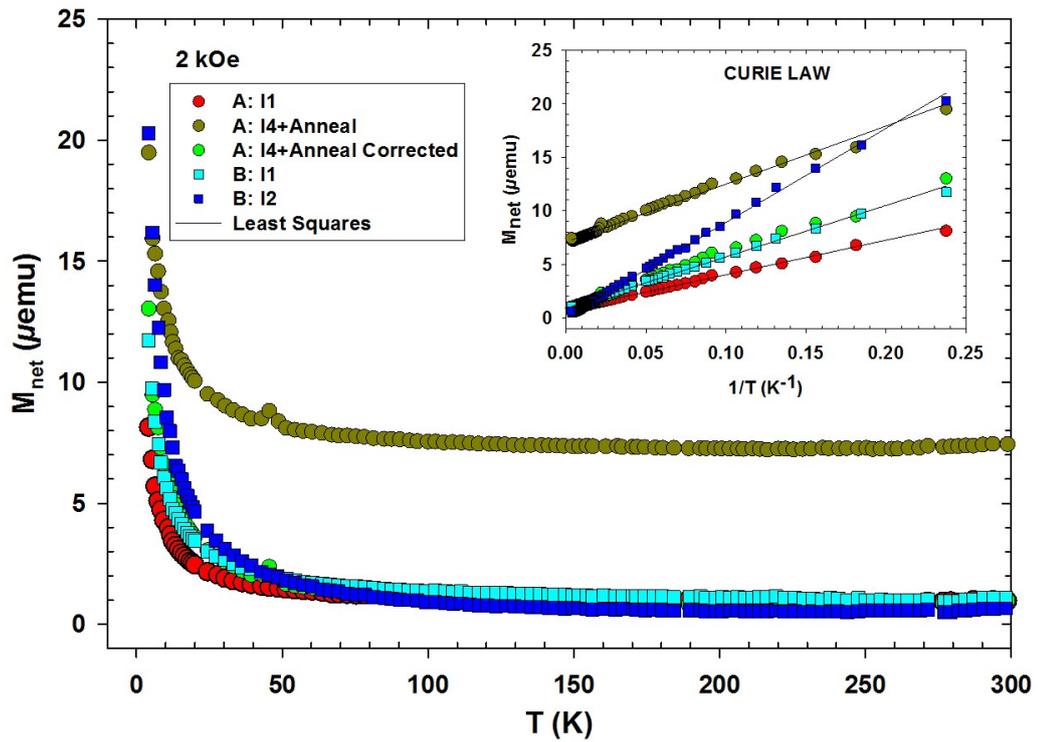


Figure 6.11: Net magnetic moment of diamond samples A and B at different irradiation (and annealing) stages acquired as a function of temperature at 2 kOe. The inset showing the net magnetic moment as a function of the inverse temperature at 2 kOe indicates that at all irradiation (and annealing) stages, the system obeys the Curie law and exhibits Curie-type paramagnetism

ferromagnetism was observed following energetic proton irradiation of carbon (HOPG), where the total magnetic moment measured $m_{\text{tot}} = m_{\text{para}} + m_{\text{ferro}}$. This was also evidenced by hysteretic behaviour of the magnetic moment cycled through an applied field, i.e. M vs H curve.

In the current study however, although a small hysteresis is observed at room temperature, the M vs H data (see Fig. 6.9) is dominated by intrinsic superparamagnetism at 300 K, which saturates to ≈ 1.8 and $0.8 \mu\text{emu}$ respectively for diamond samples A and B at relatively low applied field ≈ 30 kOe. Nonetheless, two main contributions to the pure Curie paramagnetism are evident in the post annealing data, *viz.* a temperature independent magnetic

contribution of $\approx 6-7 \mu\text{emu}$ as well as emergence of the peak at low temperature around 40-50 K. Subtraction of the constant magnetic contribution yields as expected the Curie Law. The net magnetic moment plotted versus the inverse temperature (see Fig.6.11 inset) exhibits linear magnetic behaviour converging towards 0 emu with increasing temperature (K) in all cases (except the post anneal data) confirming the formation of Curie-type paramagnetism in accordance with the Curie Law.

In a system of N atoms or ions of angular momentum J , the magnetization M is given by:

$$M = NgJ\mu_B B_J(x) \quad (6.2)$$

where $x = (gJ\mu_B H) / (k_B T)$, g is Landé g-factor, J is the angular momentum quantum number, μ_B is the Bohr magneton number and the Brillouin function is given by [221]:

$$B_J(x) = \left[\frac{2J+1}{2J} + \text{ctnh} \frac{(2J+1)x}{2J} - \frac{1}{2J} \text{ctnh} \frac{x}{2J} \right]. \quad (6.3)$$

The Curie law emerges when the main variable x of the Brillouin function $B_J(x)$ takes on values $x \ll 1$, then the magnetic susceptibility $\chi = M/H = (NJ(J+1)g^2\mu_B^2) / 3k_B T$. Since the temperature dependence measurements are obtained under isomagnetic conditions (at 2 kOe), we can write $m_p = C/T$ for the classical contribution of N paramagnetic centers each with an effective magnetic moment $\mu_{eff} = p\mu_B$. The Curie constant can therefore be written as:

$$C = N \frac{\mu_{eff}^2}{3k_B} = N p^2 2.08 \times 10^{-15} \mu\text{emuK}. \quad (6.4)$$

For the case of atomic paramagnetic centers the effective Bohr magneton

number is given by $p = g(JLS) \sqrt{J(J+1)}$. However, for the case of complex paramagnetic centers due to multi-vacancies and interstitials, neither the value nor the analytical dependence of p on the defect characteristics is known for the case of diamond.

Using Curie coefficients obtained from the Curie law (see Fig 6.11) in conjunction with Eq.6.4 and calculations of spatially resolved number of vacancies from SRIM Monte Carlo simulations (see Tables 6.1 and 6.2), the present study provides estimates of the effective Bohr magneton number and hence the effective magnetic moment per nominally produced vacancy following proton irradiation in diamond. We obtain an effective Bohr magneton number per nominally produced vacancy: $p \approx 0.17$ for Sample A and $p \approx 0.12$ Sample B and hence an effective magnetic moment of $\mu_{eff} \approx 0.17\mu_B$ for Sample A and $\mu_{eff} \approx 0.12\mu_B$ for Sample B per nominally produced vacancy.

Fig.6.12 shows Raman spectra of Sample A at various stages *viz.* Pristine, A:I4 and A:I4+Anneal. The Pristine spectrum shows a ‘clean’ diamond peak centered at 1331 cm^{-1} . The high sharpness of the peak i.e. narrow full width at half maximum (FWHM) and absence of secondary peaks indicates that the pristine sample is almost purely composed of sp^3 carbon arranged in the diamond tetrahedral geometry with very low fraction of impurities and Raman active defects.

After irradiation A:I4, the Raman spectrum shows a slight broadening in the FWHM as well as formation of secondary peaks at lower intensities. The broadening in the FWHM is related to partial deformation of the sp^3 carbon tetrahedral geometry due to radiation damage and is accompanied by the formation of the broad peak centered at $\approx 1253 \text{ cm}^{-1}$ which is indicative a structural disorder in the lattice system induced by irradiation. The set of peaks observed in the range $1430\text{-}1520 \text{ cm}^{-1}$ are due to local vibration modes of the single vacancy and those in the range $1600\text{-}1700 \text{ cm}^{-1}$ are due to vibration

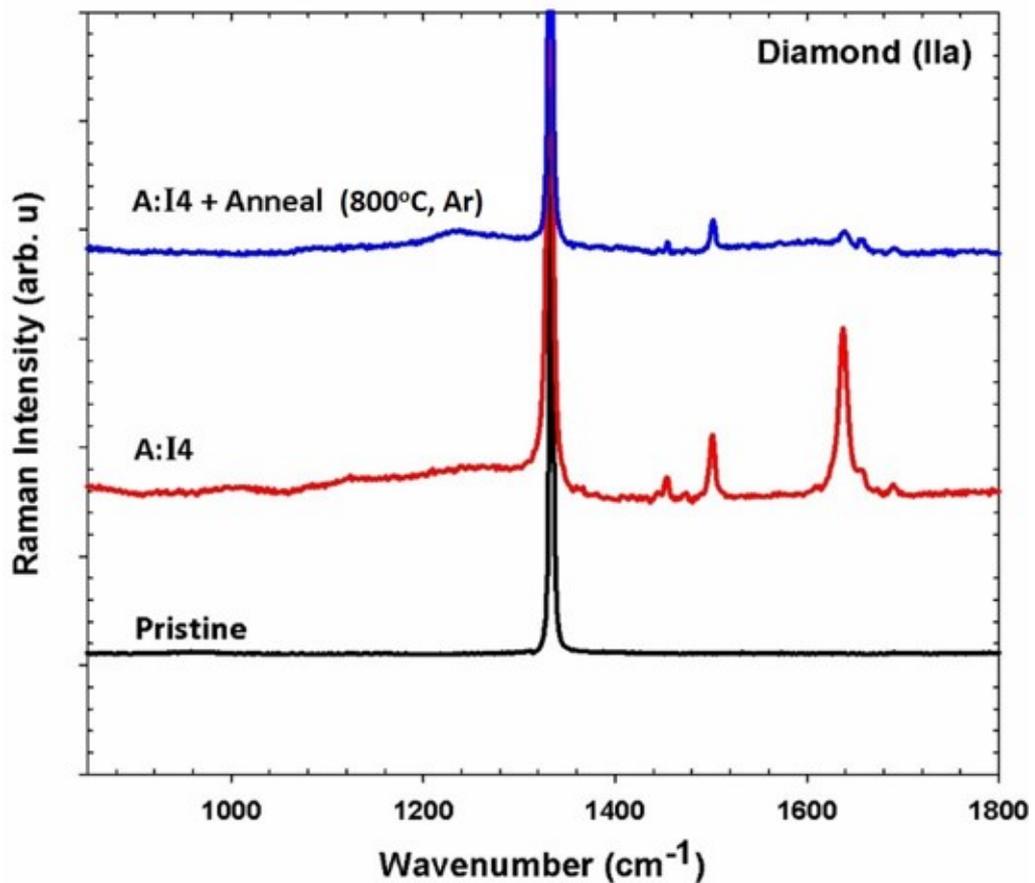


Figure 6.12: Raman spectroscopy of diamond sample A acquired at room temperature showing pristine, A: I4 and A: I4+Anneal spectra.

modes of the carbon split interstitial produced by momentum transfer in the collision cascade.

The effect of annealing as observed in Fig.6.12 is mainly a reduction in the intensity of the single vacancy and split interstitial peak assembly. In addition, the sp^3 structural geometry is partly restored resulting in a slight reduction in the FWHM of the diamond peak and in the intensity of the disorder related peak due to vacancy-interstitial recombination discussed above. No other significant peaks are observed following irradiation and annealing.

The corresponding depth resolved PL spectra are shown in Fig.6.13. The PL spectra were acquired from depths up to 30 μm into the diamond since

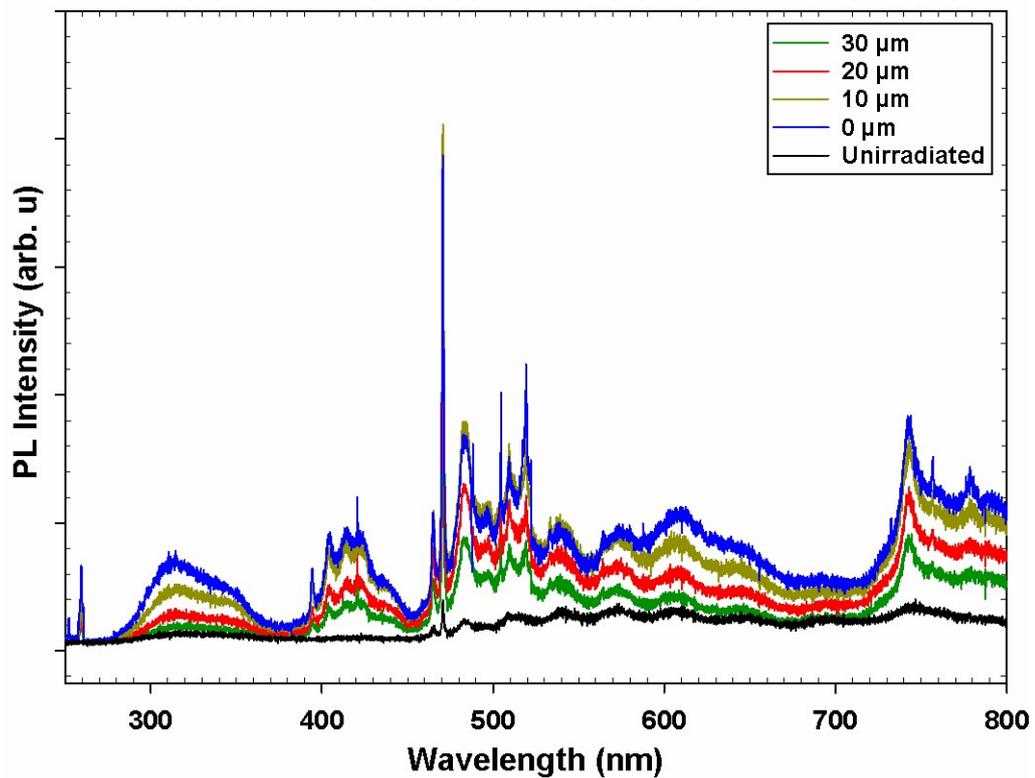


Figure 6.13: *Depth resolved photoluminescence spectroscopy of diamond sample A acquired at room temperature following irradiation stage A: I4.*

the range of 2.2 MeV protons is $\approx 29 \mu\text{m}$ in diamond. The pristine diamond PL spectrum shows no significant PL with the exception of minor TR12 and GR1 bands at relatively low intensity. The TR12 band has a zero phonon line (ZPL) at 471 nm and is the first single photon source shown to occur intrinsically in diamond with the rest all being impurity related [223]. The TR12 centre is formed due to the presence of the carbon split interstitial in diamond and exhibits a fluorescence lifetime of 3.6 ns [224] (a prerequisite of high efficiency single-photon sources). The GR1 band exhibits a ZPL at 742 nm and is related to the presence of the single vacancy in the neutral charge state (V^0) in diamond and hence resulting in non-paramagnetic behaviour.

The main effects of proton irradiation observed in the diamond PL spectra are therefore; significant enhancement of intensity in the TR12 and GR1 bands,

formation of the ND1 and 3H centers, as well as the broad luminescence band in the spectral range 270-370 nm. The ND1 centre is associated with formation of the negatively charged single vacancy (V^{-1}) and exhibits a ZPL at 394 nm with vibronic sidebands in the spectral range 400-450 nm. Studies have shown that the ND1 center exhibits paramagnetic behaviour [225]. The 3H center emerges due to the formation of vacancy-interstitial clusters and exhibits a ZPL at 504 nm. The broad luminescence around 270-360 nm lie in the ultra-violet continuum spectral range [226].

6.2.3 Micro-irradiation Investigations

Fig.6.14 shows optical images of the *micro*-irradiated type-IIa diamond samples. The darker localized regions in the images is due to proton radiation damage in diamond where the ion fluence was varied for each region (A-E) as per Table 5.4. All irradiated regions in Fig.6.14 were analysed using TM-AFM, MFM and EFM. It was found that although a response (in terms of phase shift) was measured for all irradiated regions, the signal strength was inversely proportional to the ion fluence with which the region was bombarded as well as the irradiated surface area (the average inter-vacancy spacing increases with increasing irradiation area). In addition, regions with smaller irradiated areas provided for more effective imaging due to the scanning time factor as measurements were acquired under ambient conditions. Therefore, for brevity as well as reasons provided above, we present and interpret results for Region-A of Sample-1 and Region E of Sample 2.

Figs.6.15 and 6.16 shows examples of TM-AFM topography images of region-A of Sample-1 and region E of Sample 2 respectively, together with the corresponding line profiles extracted across the regions indicated by the dashed lines. The radiation induced upswelling for both samples as seen from the line

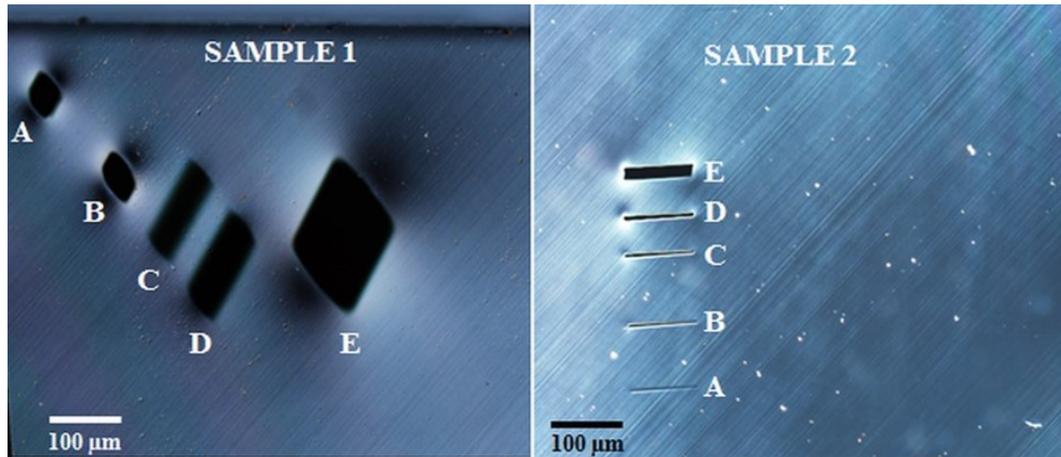


Figure 6.14: *Optical images of micro-irradiations on type IIa diamond (100) surfaces by 2.2 MeV Proton micro-beams.*

profiles is in the range 50-100 nm above the normal diamond surface. For all regions investigated, the radiation induced surface up-swelling observed using TM-AFM is consistent with the *micro*-irradiated surface area and is generally proportional to the ion fluence. Surface roughness measurements (rms) for both samples yielded $R_q \approx 1\text{-}5$ nm (after irradiation) as deduced from TM-AFM analysis. The acquired images are produced from a scan of the irradiated surface in the van der Waals force field ≈ 1 nm above the surface.

Maximum radiation induced damage in the diamond occurs near the end of range (EOR) of the protons ($\approx 28 \mu\text{m}$) where the nuclear stopping force dominates the electronic stopping force [227] producing on average ≈ 11 vacancies/ion according to SRIM calculations. A relatively undamaged confining cap therefore exists along the ion path between the surface and EOR damaged region. This results in the formation of a microscale region under high pressure with low probability of diamond-to-graphite structural relaxation in the bulk [228].

Fig.6.17 and 6.18 shows examples of MFM Phase shift images of region-A of Sample-1 and region-E of Sample 2 acquired from a lift scan height of 50

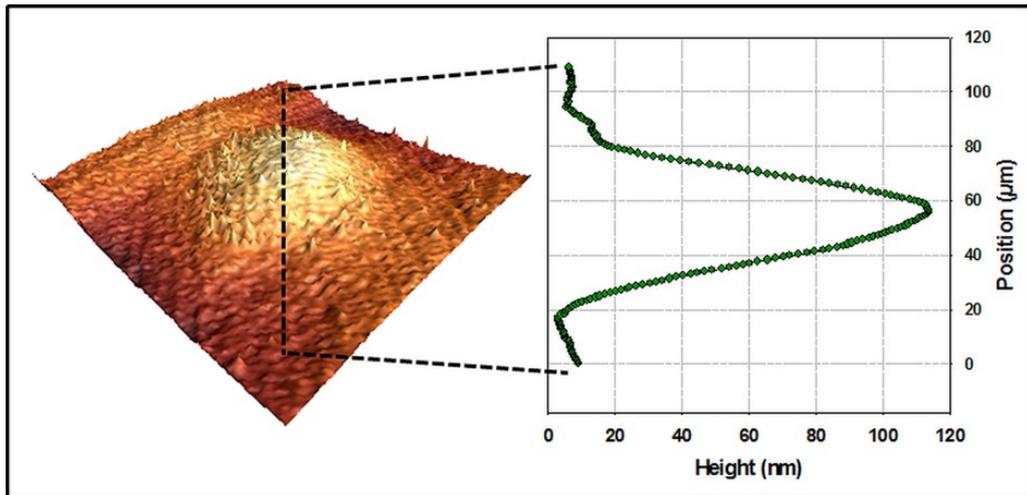


Figure 6.15: Example of a Tapping Mode AFM topography image acquired over region-A of Sample-1 together with a line profile extracted across a region represented by the dashed lines.

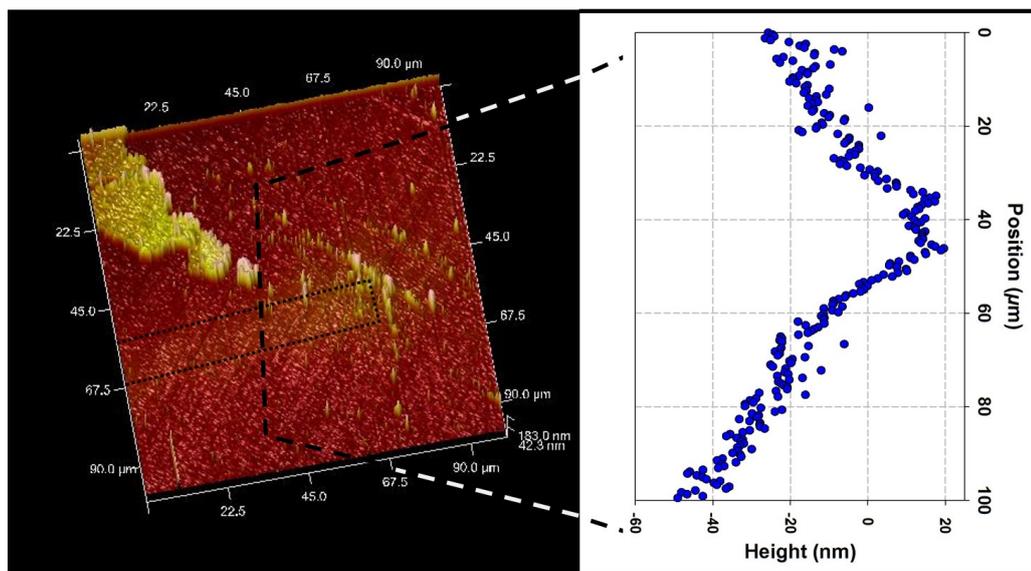


Figure 6.16: Example of a Tapping Mode AFM topography image acquired over region-E of Sample-2 together with a line profile extracted across a region represented by the dashed lines. The dotted lines represent the irradiated region.

nm above the *surface* as well as line profiles extracted across the regions represented by the dashed lines in the MFM images. Phase shift signals measured

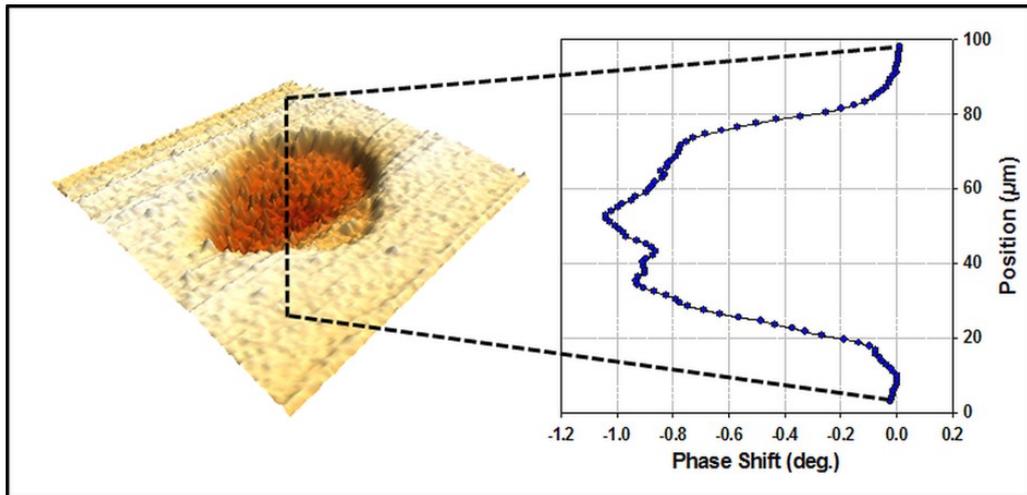


Figure 6.17: Example of a MFM Phase image (deg.) of region-A sample-1 acquired 50 nm above the diamond (100) surface together with the corresponding line profile (deg.) extracted from a region represented by the dashed lines.

from the two samples show differences in the magnetic response of the probe over the irradiated regions. In Fig. 6.17, the probe exhibits attraction to the irradiated region with a corresponding phase shift up to ≈ 1 deg. However in the case of Fig 6.18, the probe is weakly repelled from the irradiated region with a corresponding phase shift up to ≈ 0.1 deg.

Phase shift signals recorded from region-A of sample-1 shown in Fig.6.17 exhibited the strongest signal strength of all the investigated micro-irradiations and represent the micro-scale region with the highest fluence applied in the present study corresponding to $\approx 1.4 \times 10^{18}$ H⁺/cm² (see Table 5.4 for the irradiation parameters). For this reason, region-A of sample-1 was further investigated using lift scan height variation, probe polarization and EFM.

Assuming a conservative experimental error of ≈ 0.01 deg. in the phase shift signal and given that the cantilever spring constant k of the magnetic probe is ≈ 4.3 Nm⁻¹ and the quality factor $Q \approx 310$, the magnetic field gradient $\frac{\partial F}{\partial z}$ measured in region-A of Sample-1 shown in Fig.6.17 is ≈ 1.4 pN/nm. MFM

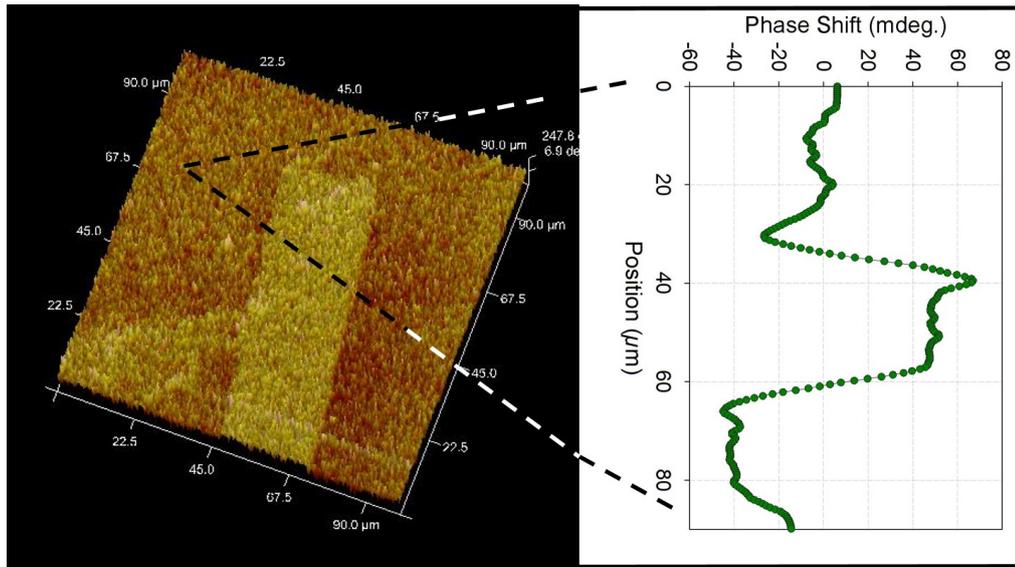


Figure 6.18: Example of a MFM Phase image (deg.) of region-E sample-2 acquired 50 nm above the diamond (100) surface together with the corresponding line profile (deg.) extracted from a region represented by the dashed lines.

investigations of all micro-scale irradiated regions show that the ion fluence plays an important role in the observed magnetic response. Fluences below $8.4 \times 10^{17} \text{H}^+/\text{cm}^2$ displayed a very weak magnetic response in the phase signal. This suggests that the observed magnetic response may be closely related to the spacing between point defects such as single vacancies created in the irradiated region which is a function of the ion fluence.

Fig.6.19 shows line profiles representing the magnetic response of region-A of Sample-1 as function of the lift scan height (nm) with the magnetic probe magnetized in the '+1' direction. The strength of the measured field is inversely proportional to the lift scan height. The magnetic signal measured over the micro-irradiated region is consistent and stable even up to 200 nm above the surface. In addition, this measurements also indicate that the measured field is a long range field as van der Waals forces are negligible above 50 nm from the surface. As region-A Sample-1 displays the most intense phase shift contrast in all the micro-irradiations, this region was further investigated using

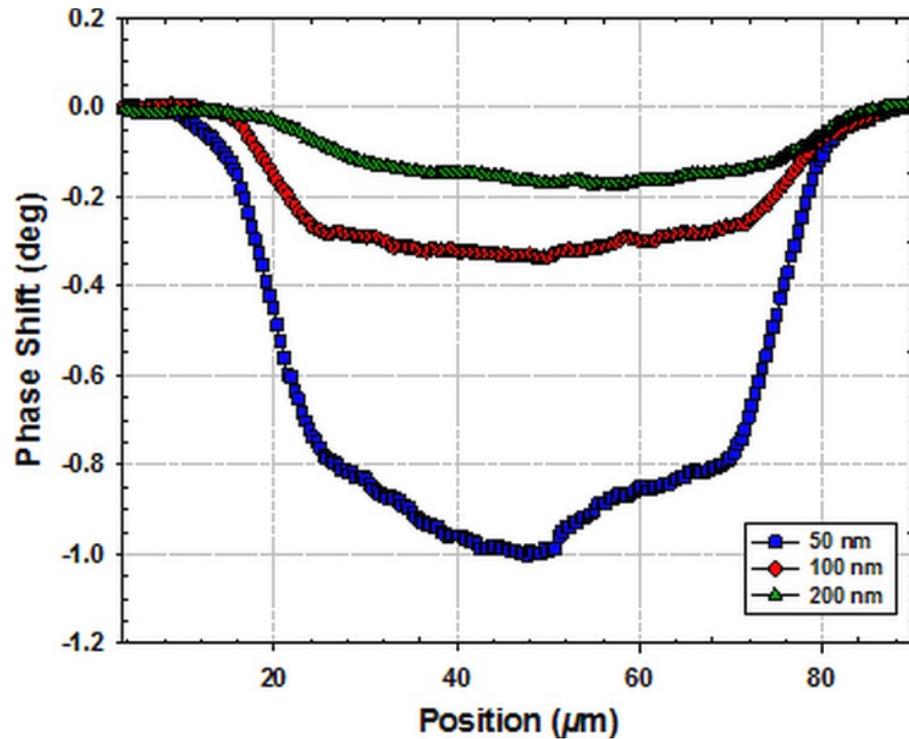


Figure 6.19: *Phase shift (deg.) versus Position (μm) of the magnetic probe over region-A Sample-1 at several lift scan heights (nm) with the probe polarized in the '+1' polarization direction.*

non-magnetized probes '0', as well as probes magnetized in the '+1' and '-1' magnetization directions to compare the field strength and orientation under different polarizations.

Fig.6.20 shows phase shift (deg.) profiles of region-A of Sample-1 acquired at a lift scan height of 50 nm using different magnetization directions, namely '+1', '-1' and non-magnetized '0' (i.e. as fabricated). As in Figs.6.17 and 6.19, negative phase shifts were again observed in the micro-irradiated region for all the probe magnetization directions (Fig.6.20), indicative of an attraction force between probe and sample.

During MFM imaging of magnetic structures, multiple forces interact with the MFM probe while scanning across the sample typically at lift scan heights \sim 1-100 nm. Therefore the signal measured by the MFM probe is often convo-

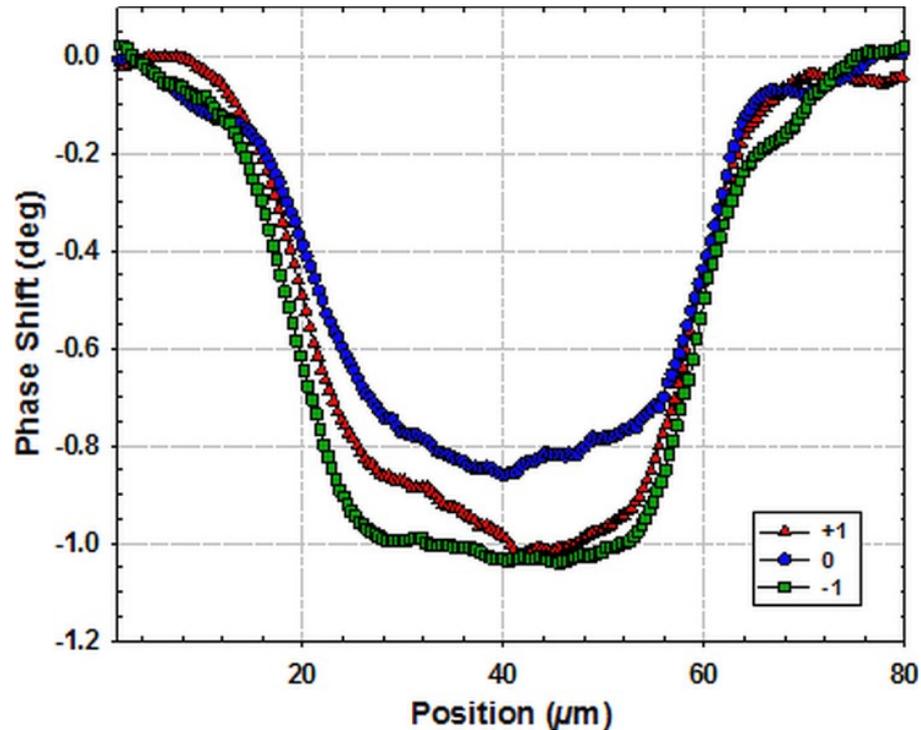


Figure 6.20: Phase shift (deg.) versus Position (μm) of the magnetic probe over region-A of sample-1 under different probe magnetization directions.

luted and the total force acting on the probe is typically $F_{tot} = F_{vdW} + F_{mag} + F_{elec}$. Probes utilized for MFM imaging typically consist of a magnetic coating such as Co/Cr which is also exhibits metallic properties. For this reason, the probe is sensitive to both magnetic and electrostatic forces, although in practice different probes are used for EFM imaging. For this reason, irradiated samples were further investigated using EFM techniques described earlier to provide insight for a reasonable interpretation of the results.

EFM imaging was carried out using conductive, non-magnetic PtIr coated type SCM-PIT probes from Bruker Scientific. For comparison, further EFM imaging was carried out using conductive, magnetic Co/Cr coated type MESP-HM probes which were previously used for MFM imaging. Electrical bias in the range 1-10V was applied across the probe for imaging. Again for brevity we present data acquired from region-A of Sample-1 where the highest proton

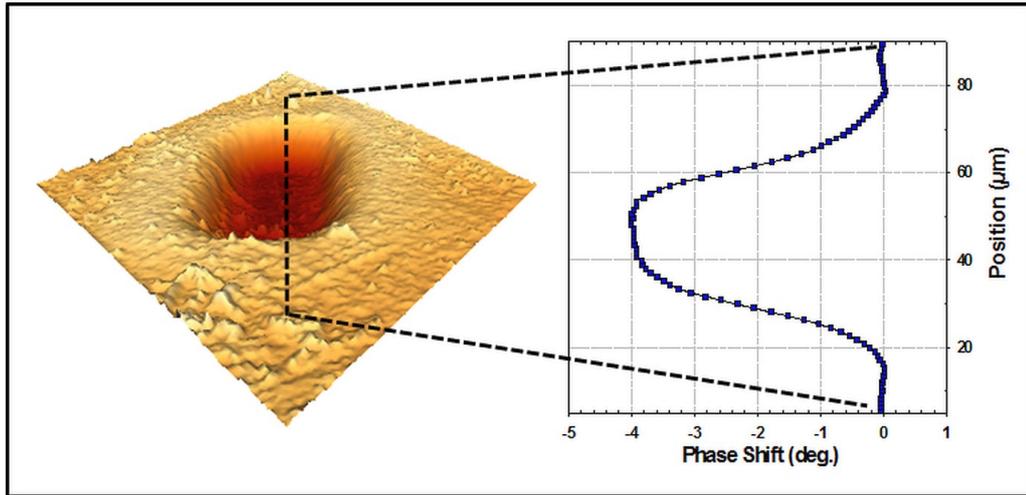


Figure 6.21: Example of an EFM image acquired over region-A of Sample-1 using a SCM-PIT type probe electrically biased at 4V together with the corresponding line profile (deg.) extracted across the region represented by the dashed lines.

fluence was applied and highest MFM signal measured.

Fig.6.21 shows an example of an EFM image acquired over the irradiated region-A of Sample-1 using a commercially available SCM-PIT type probe at an applied electrical bias of 4V and a lift scan height of 50 nm. The EFM image shows a negative phase shift associated with attractive forces in the micro-irradiated region as observed in the MFM image.

The van der Waals force (F_{vdW}) and force gradient between a spherical tip and semi-finite flat sample can be written as [229]:

$$F_{vdW} \approx A_H R / 6z^2; \frac{\partial F_{vdW}}{\partial z} \approx -A_H R / 12z^3. \quad (6.5)$$

where R is the effective radius of the tip, z is the tip-sample separation and A_H is the Hamaker constant (typically $\sim 10^{-19}$ J). For a sharp tip of radius ≈ 10 nm and a tip-sample separation of ≈ 50 nm, the van der Waals force gradient is therefore $\partial F_{vdW} / \partial z \sim 1 \times 10^{-6}$ N/m.

The electrostatic force and force gradient between a metallic probe and a sample can be written as:

$$F_{elec} = \pi\epsilon_0 U^2 R/z; \quad \frac{\partial F_{elec}}{\partial z} = -\pi\epsilon_0 U^2 R/z^2; \quad (6.6)$$

where U, R and ϵ are the bias voltage between tip and sample, the effective tip radius and the permittivity of free space respectively, z is the tip-sample separation. Therefore for a voltage of 1-10 V, applied across a probe with tip radius ≈ 10 nm scanning at 50 nm above a given surface, the electrostatic force gradient, $\partial F_{elec}/\partial z$ falls in the range $\approx 1 \times 10^{-4}$ to 1×10^{-2} N/m.

Quantitative evaluation of the magnetic force gradient between the magnetic tip and sample requires accurate knowledge of geometry and distribution of magnetic properties of the tip and sample which are usually not accurately known. However it has been shown that the force gradient above the center of a transition of a longitudinal recording medium with a long dipole tip can be written as [230]:

$$F'_{mag} \sim \frac{1}{(a+z)^2} \quad (6.7)$$

where z is the tip-sample separation and a is the transition width, on the order of 100 nm. For a tip-sample separation on the order of 100 nm, the magnetic force gradient decays slower than the electrostatic and van der Waals force gradients. Due to the often unknown tip moment distribution and different nature of the sample domain walls, there is no universal law relating the magnetic force (force gradient) to the tip-sample separation. Therefore, for a sharp tip subject to a low bias voltage U , the magnitude of the magnetic force gradient measured between a tip and sample can be significantly larger than the van der Waals and electrostatic force gradients even at small tip-sample separations (20 nm) [231].

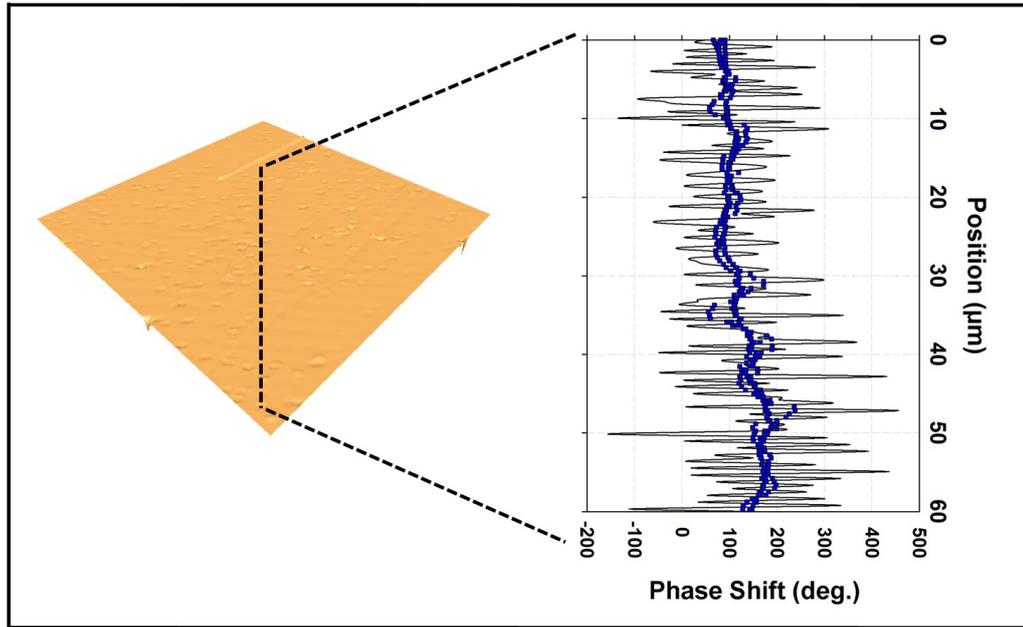


Figure 6.22: Example of an EFM image acquired over region-A of Sample-1 using a SCM-PIT type probe under zero electrical bias (0V) together with the corresponding line profile (deg.) extracted across the region indicated by the dashed lines.

Fig 6.22 shows an EFM image acquired using a PtIr coated SCM-Pit probe at a lift scan height of 50 nm, together with the corresponding line profile extracted across the region represented by the dashed lines. The image shows that electric force gradient measured at a lift scan height of 50 nm using a non-magnetic, metallic probe is negligible as no image contrast corresponding to attraction or repulsion of the EFM probe is observed. This observation confirms the approximations indicated above, i.e. at a lift scan height of 50 nm, both the van der Waals and electrostatic force gradients are significantly weaker than the magnetic force gradient. The blue curves in Fig. 6.22 are two 2D first and second order polynomial filters applied to the raw data profile for qualitative presentation.

To investigate the voltage dependence of the metallic, magnetic type MESP-HM and metallic, non-magnetic SCM-Pit probes, we systematically applied a bias voltage from 0 V up to 10 V and measured the EFM response for compari-

son. The results thereof are presented in Fig 6.23. According to Cherniavskaya et al. [232], the electrostatic force acting between the probe and the sample can be written as:

$$F(z) = \frac{1}{2} \frac{(dC_{s-t})}{dz} V_t^2 + E_S Q_t \quad (6.8)$$

where C_{s-t} , V_t , E_S and Q_t refer to the tip-sample capacitance, the voltage applied to the tip, the electric field at the tip location that is only created by the charges and/or multipoles in the sample surface and the effective charge on the tip (where; $Q_t = C_{s-t}V_t + Q_{im}$ where Q_{im} is the image charge in the tip induced by the static charge distribution on the sample surface) respectively. Therefore the electrostatic contribution during EFM measurement is then given by:

$$\Delta\phi \approx -\frac{Q}{k} \left[\frac{\partial^2 C_{s-t}}{\partial z^2} \frac{V_t^2}{2} + \frac{\partial}{\partial z} E_S C_{s-t} V_t + \frac{\partial}{\partial z} E_S Q_{im} \right]. \quad (6.9)$$

The voltage dependence of the probe response for both the SCM-Pit and MESP-HM probes reflected in Fig.6.23 confirm the quadratic dependence of the EFM phase shift on the bias voltage in Eq. 6.9. The quadratic functions were fitted to the data using the least squares method giving $R^2 \approx 0.99$ for both probe types.

It is expected that at every data acquisition point along a scan, electric field between the surface and the probe measured at the tip, E_S as well as the image charge Q_{im} are approximately constant in the surface normal direction given the dimensions of the probe tip ($\approx 2 - 10$ nm) relative to the micro-irradiated area which has low surface roughness ($R_q \approx 1-5$ nm). Therefore when $V=0$, $\partial(E_S Q_{im})/\partial z \approx 0$ which results in zero phase shift, $\Delta\phi \approx 0$ for the EFM signal, as per Eq:6.9. The EFM data acquired using SCM-PIT probes at zero electrical bias demonstrate that the image charge as well as tip electric field induced by the charges and/or multipoles in the diamond sample surface are

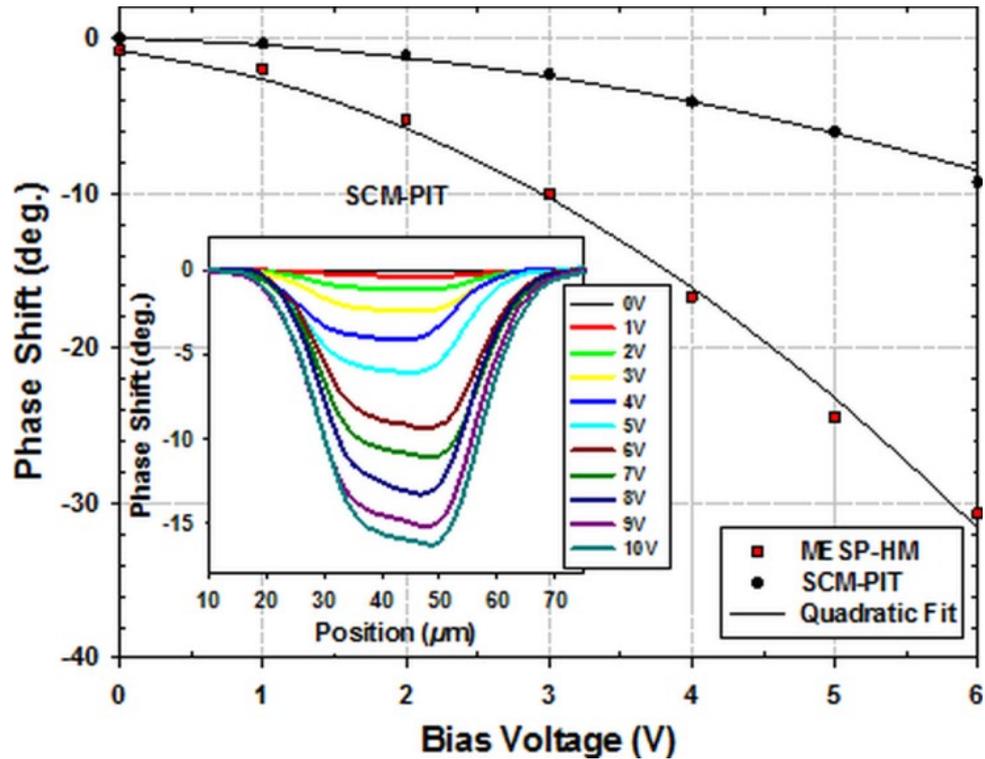


Figure 6.23: Electrostatic response measured as a phase shift (deg.) from the piezo drive at 50 nm above region-A of Sample 1 using MESP-HM (square symbols) and SCM-PIT (circular symbols) probes types as a function of the applied electrical bias voltage (V). The insert shows an example of EFM profiles acquired using SCM-PIT probes illustrating the deviation from normal quadratic behaviour at higher bias voltages.

not sufficient to generate measurable/distinct electrostatic field gradients at a lift scan height of 50 nm (and above 50 nm given that field is inversely proportional to the lift scan height). This analysis is further confirmed by the acquired EFM data presented in Figs.6.22 and 6.23.

Therefore, based on the above analysis, we can deduce that the phase shift signal measured by the MESP-HM MFM probe at 50 nm above the surface (and beyond), is primarily due to a magnetic interaction between the magnetic probe and magnetic structures in the diamond samples. In addition, the MFM image acquired at a lift scan height of 50 nm over region E of Sample 2 (Fig.

6.18) shows positive force gradients associated with repulsion of the probe from the irradiated region. Given that electric force gradients are characterized by attraction to the surface as indicated in Fig. 6.23, at a lift scan height of at least 50 nm, the force gradients measured by the MFM probe are due to the magnetic behaviour of the irradiated regions.

It is evident from the MFM images that the non-irradiated region in the diamond samples exhibit negligible magnetic response, i.e. $\Delta\phi \approx 0$ whereas a significant phase shift, $\Delta\phi \approx 1$ is observed in the irradiated region(s) even at 50 nm above the surface at room temperature. Therefore, a non-intrinsic magnetic response is observed at room temperature in diamond using the MFM technique following energetic proton irradiation. The scale of the observed phase shift signal is primarily dependent on the magnetization magnitude and direction of the MFM probe as shown in Fig.6.20 and is also comparable with phase shift magnitudes observed in previous studies of proton irradiation in other carbon materials [10, 11, 17].

Chapter 7

Conclusions and Outlook

Empirical investigation of the interaction between Xenon (Xe^{20+} to Xe^{31+}) and Bismuth (Bi^{50+} to Bi^{62+}) SHCIs with type Ib diamond (111) surfaces using Tapping Mode AFM analysis shows the formation of nano-craters with averaged diameters in the range ≈ 12 -27 nm. A direct proportionality between nano-crater diameter and SHCI potential energy (charge state) is observed. Linear trends in nano-crater diameter as a function of SHCI potential energy suggest that kinetic energy induced surface nanoscale modifications are feasible in type Ib diamond (111) even at zero potential energy in the explored energy range, provided the SHCI kinetic energy is sufficient and neglecting possible threshold effects.

Although the formation of nanodefects in diamond is primarily dependent on the SHCI potential energy, higher kinetic energy of the SHCI appears to enhance (or dilate) the diameter of induced nano-craters in type Ib diamond. Synergistic interplay between potential and kinetic energy during SHCI momentum transfer appears to play a significant role in nano-crater formation in type Ib diamond (111). Thorough empirical investigation of potential energy effects in type Ib diamond (and other materials) may therefore require SHCI deceleration towards very low kinetic energies.

Future studies could be focused on using lower charge states and kinetic energy for Xenon, Bismuth as well as other SHCIs species to conclusively reveal the morphology of SHCI induced nano-craters and also the existence (or absence) of threshold effects in diamond and other carbon materials (e.g. graphene). This may also allow for investigation of the effect of synergistic interplay between kinetic and potential energy in defect formation at different energy ranges. The applicability of the proposed HCI interaction mechanisms including Coulomb Explosion Model, Thermal Spike Models and Desorption Mediated Model, will also be investigated for carbon materials, particularly diamond, HOPG and graphene.

In the thermal spike regime, irradiation of the diamond surface with HCIs results in an intense excitation of the electronic subsystem of the surface. Energy transferred from the electronic to the lattice subsystem of the surface via electron-phonon coupling leads to localized melting followed by rapid cooling in $\sim fs$ timescales. Rapid cooling of the nanodefekt may lead to the formation of sp^2 and sp^3 carbon phases in the nanodefekts. Studies have shown that sp^2 carbon exhibits magnetic order in various configurations including edge magnetism. The possible spontaneous ordering of magnetic moments under quantum confinement conditions in the restructured sp^2 or sp^3 carbon (or their combinations) in the SHCI induced nanodefekts and at the edges of the nanodefekts will be investigated in the future.

Proton macro irradiation of type-IIa diamond, using selected parameters, results in the evolution of magnetic and optical properties. Room temperature measurements of the magnetic moment of pristine and proton macro-irradiated diamond as function of applied field exhibits intrinsic superparamagnetism which saturates to $\approx 1-2 \mu\text{emu}$ at relatively low applied field ≈ 30 kOe. The observed superparamagnetism is possibly related to the presence of trace elements introduced during the synthesis process of diamond. Modification in

the optical properties of diamond is observed at room temperature following proton macro irradiation through enhancement of the TR12 and GR1 bands, formation of the ND1 and 3H centers, as well as emergence of broad luminescence band in the ultraviolet continuum.

Low temperature SQUID measurements (4.2 K) confirm the formation of Curie -type paramagnetism, where the paramagnetic factor increases in proportion to the proton fluence. The Stopping and Range of Ions in Matter (SRIM) Monte Carlo simulations together with SQUID observations show a strong correlation between vacancy production, proton fluence and the paramagnetic factor. At an average surface vacancy spacing of $\approx 1-1.6$ nm and bulk (peak) vacancy spacing of $\approx 0.3-0.5$ nm we find that Curie paramagnetism is induced by formation of ND1 centres with an effective magnetic moment $\mu_{eff} \sim (0.1 - 0.2) \mu_B$.

Temperature dependent magnetic moment measurements show the formation Curie-type paramagnetism following proton macro-irradiation at all investigated energies and fluences. However, annealing the macro-irradiated type-IIa diamond at 800 °C in an argon atmosphere results in the reduction of the paramagnetic factor due to partial restoration of the diamond sp^3 tetrahedral configuration as a result of vacancy-interstitial recombination. In addition, the annealed irradiated diamond exhibits temperature independent magnetic behaviour with a magnetic moment $\approx 6-7 \mu_{emu}$ superimposed with Curie paramagnetism at 2kOe. Similar temperature independent magnetic behaviour observed in other studies of proton irradiated carbon has been attributed to the radiation induced ferromagnetism.

SPM analysis of proton micro-irradiated diamond shows the formation of morphological modifications consistent with the irradiation parameters, e.g. the beam size and fluence. Surface upswelling up to ≈ 150 nm induced by radiation damage is observed in the irradiated regions. In addition, MFM analysis

shows the presence of force gradient signals originating from the irradiated domains with a phase shift ≈ 1 deg. which are measurable even at ≈ 200 nm above the irradiated surface. Using probe polarization dependent MFM measurements we note that the intensity of the measured force gradient signal is dependent on the probe polarization direction. By exploiting the capabilities of MFM and EFM, we have demonstrated that the force gradient measured in the micro-irradiated regions originates from the magnetic behaviour of the proton micro-irradiated domains rather than from surface electrostatic forces.

Due to among other reasons, the different measurement conditions used as well as the respective sources of error in each measurement approach, direct comparison between results of proton micro-irradiated diamond from SPM analysis with proton macro-irradiated diamond from SQUID analysis is not trivial but should be carried out in a very controlled setup for improved results. Nonetheless, the present study has shown that proton irradiation of diamond induces two main magnetic components, i.e. Curie-type paramagnetism and temperature independent magnetism (observable only after annealing) which is a possible indication of a weak ferromagnetic state in the irradiated and annealed diamond. This however, requires further detailed investigations for confirmation.

Future investigations using more detailed annealing cycles following both *macro* and *micro* irradiation could elucidate the evolution of the observed temperature independent magnetic signal. In conjunction with empirical studies, concerted modelling investigations could lead to clarification of the observed magnetic effects induced by irradiation in diamond and possibly a method of tailoring these effects for advanced applications as earlier discussed. However due to the sensitivity of such studies, type-IIa diamonds with less trace elements should be used. To facilitate effective SPM characterization of micro/nano-irradiated domain in diamond, a conductive, non-magnetic thin

film could be deposited onto the diamond surface to allow residual surface charge to be drained/grounded during MFM characterization thus reducing the possibility of signal convolution with electric force gradients. Temperature dependent MFM measurements could also be used to draw conservative comparisons with measurements from the SQUID.

Appendix A

Published Manuscripts

The work discussed in this thesis is based on the following published manuscripts:

- Makgato, T., Sideras-Haddad, E., Shrivastava, S., Schenkel, T., Ritter, R., Kowarik, G., Aumayr, F., Crespo López-Urrutia, J.R., Bernitt, S., Beilmann, C., Ginzler, R., *Nuclear Instruments and Methods in Physics Research Section B*, 314 (2013), pp.135 - 139.
- Makgato, T.N., Sideras-Haddad, E., Ramos, M.A., García-Hernández, M., Climent-Font, A., Zucchiatti, A., Muñoz-Martin, A., Shrivastava, S., Erasmus, R., *Journal of Magnetism and Magnetic Materials*, 413 (2016), pp. 76-80.
- Daya, N., Sideras-Haddad, E., Makgato, T.N., García-Hernández, M., Climent-Font, A., Zucchiatti, A., Ramos, M.A., *Diamond and Related Materials*, 64 (2016), pp. 197-201.

References

- [1] Awschalom, D. D., Epstein, R. and Hanson, R., *Scientific American* 297(4) 84 (2007).
- [2] Prins, J. F., *Photovoltaic Cell of Semi-Conducting Diamond*, US 4571447, (1986).
- [3] Hattas, M., Schenkel, T., Hamza, A.V., Barnes, A.V., Newman, M. W., McDonald, J. W., Niedermayer, T. R., Machiciane, G. A., Schneider, D. H., *Physical Review Letters*, Vol 83, 21, (1999) 4273.
- [4] Aumayr, F., Facsko, S., El-Said, A. S., Trautmann, C., and Schleberger, M., *Journal of Physics: Condensed Matter*, 23 (2011) 393001.
- [5] Hamza, A. V., Newman, M. W., Thielen, P.A., Lee, H.W.H., Schenkel, T., McDonald, J. W. and Schneider, D. H., *Applied Physics Letters*, 79 (2001) 18.
- [6] Gillaspay, J.D., *Journal of Physics. B: Atomic, Molecular and Optical Physics*, 34 (2001) R93-R130.
- [7] Aumayr, F., and Winter, H., *e-Journal for Surface Science and Nanotechnology*, Vol 1 (2003) 171-174.
- [8] Turek, P., *Chemical Physics Letters*, 186 (1991) 401.
- [9] Allemand, P.M., Khemani, K.C., Koch, A., Wudl. F., Holczer, K., Donovan, S., Grüner, G., Thompson, J. D., *Science*, 253 (1991) 301.

- [10] Esquinazi, P., Spemann, D., Höhne, R., Setzer, A., Han, K-H. and Butz, T., *Physical Review Letters*, 91 (2003) 227201.
- [11] Esquinazi, P., Höhne, R., Han, K-H., Setzer, A., Spemann, D. and Butz, T., *Carbon*, 42 (2004), pp. 1213-1218.
- [12] Barzola-Quiquia, J., Esquinazi, P., Rothermel, M., Spemann, D. and Butz, T., *Journal of Nuclear Materials*, 389 (2009), pp.336-340.
- [13] Spemann, D., Schindler, K., Esquinazi, P., Diaconu, M., Schmidt, H., Höhne, R., Setzer, A and Butz, T., *Nuclear Instruments and Methods in Physics Research B*, 250 (2006), pp. 303-308.
- [14] Park, N., Yoon, M., Berber, S., Ihm, J., Osawa, E. and Tománek, D., *Physical Review Letters*, 91 (2003) 23.
- [15] Xia, H., Li, W., Song, Y., Yang, X., Liu, X., Zhao, M., Xia, Y., Song, C., Wang, T-W., Zhu, D., Gong, J. and Zhu, Z., *Advanced Materials*, 20 (2008), pp.4679-4683.
- [16] Kusakabe, K. and Maruyama, M. *Physical Review B*, 67 (2003) 092406.
- [17] Han, K-H., Spemann, D., Esquinazi, P., Höhne, R., Riede, V. and Butz, T., *Advanced Materials*, 15 (2003) 20, 1719.
- [18] Balasubramanian, G., Neumann, P., Twitchen, D., Markham, M., Kolesov, R., Mizuochi, N., Isoya, J., Isoya, J., Achard, J., Beck, J., Tissler, J., Jacques, V., Hemmer, P. R., Jelezko, F. and Wrachtrup, J., *Nature Materials*, 8 (2009) pp. 383-387.
- [19] Dutt, M. V., Childress, L., Jiang, L., Togan, E., Maze, J., Jelezko, F., Zibrov, A. S., Hemmer, P. R., and Lukin, M. D., *Science*, 316 (2007) 1312-1316.
- [20] Hanson, R., Gywat, O. and Awschalom, D. D., *Physical Review B* 74 (2006) 161203R.

- [21] Fuchs, G. D., Burkard, G., Klimov, P. V. and Awschalom, D. D., *Nature Physics*, 7 (2011) 789-793.
- [22] Kozlov, V. A. and Kozlovski, V. V., *Semiconductors*, 35, 4 (2001), pp. 735-761.
- [23] Larson, L. A., Williams, J. M. and Current, M. I., *Reviews of Accelerator Science and Technology*, 4, 01 (2011) DOI: 10.1142/S1793626811000616.
- [24] Ziegler, J. F., Ziegler, M. D. and Biersack, J. P., *Stopping and Range of Ions in Matter*, 2011.
- [25] Nair, R. R., Sepioni, M., Tsai, I-Ling, Lehtinen, O., Keinonen, J., Krasheninnikov, A. V., Thomson, T., Geim, A. K. and Grigorieva, I. V., *Nature Physics*, 8 (2012) pp. 199-202.
- [26] Barzola-Quiquia, J., Esquinazi, P., Rothermel, M., Spemann, D., Setzer, A. and Butz, T., *Nuclear Instruments and Methods in Physics Research B*, 256 (2007) pp. 412-418.
- [27] Kozlov, V. A. and Kozlovski, V. V., *Physical Review Letters*, 101 (2008) 037203.
- [28] Zhang, Y., Talapatra, S., Kar, S., Vajtai, R., Nayak, S. K. and Ajayan, P. M., *Physical Review Letters*, 99 (2007) 107201.
- [29] Ohldag, H., Tylliszczak, T., Höhne, R., Spemann, D., Esquinazi, P., Ungureanu, M. and Butz, T., *Physical Review Letters*, 98 (2007) 187204.
- [30] Sepioni, M., Nair, R. R., Tsai, I-Ling, Geim, A. K. and Grigorieva, I. V., *European Physics Letters*, 97 (2012) 47001.
- [31] Ramos, M. A., Barzola-Quiquia, J., Esquinazi, P., Muñoz-Martin, A., Climent-Font, A., Garcia-Hernández, M., *Physical Review B*, 81 (2010) 214404.

- [32] Lee, H., Miyamoto, Y. and Yu, J., *Physical Review. B*, 79 (2009) 121404(R).
- [33] Yazyev, O. V. and Katsnelson, *Physical Review. Letters*, 100 (2008) 047209.
- [34] Enoki, T., Fujii, S. and Takai, K., *Carbon*, 50 (2012), pp. 3141-3145.
- [35] Yazyev, O. V., *Physical Review Letters*, 101 (2008) 037203.
- [36] Faccio, R., Pardo, H., Denis, P. A., Yoshikawa Oeiras, R., Araújo-Moreira, F. M., Veríssimo-Alves, M. and Mombrú, A. W., *Physical Review B*, 77 (2008) 035416.
- [37] Lehtinen, P. O., Foster, A. S., Ma, Y., Krasheninnikov, A. V. and Nieminen, R. M., *Physical Review Letters*, 93 (2004) 18.
- [38] Talapatra, S., Ganesan, P. G., Kim, T., Vajtai, R., Huang, M., Shima, M., Ramanath, G., Srivastava, D., Deevi, S. C. and Aiavan, P. M., *Physical Review Letters*, 95 (2005) 097201.
- [39] Meredith, M., *Diamonds, Gold and War: The British, the Boers and the Making of South Africa*, New York: Public affairs, ISBN 1-58648-473-7, (2007), pp.16.
- [40] Berman, R., ed, *The Physical Principles of Diamond*, Oxford University Press, London, (1965)
- [41] Kittel, C., *Introduction to Solid State Physics*, Seventh edition, John Wiley and Sons Inc., New York, (2006), pp. 15-26.
- [42] Pierson, H. O., ed, *Handbook of Carbon, graphite, diamond and fullerenes: Properties, Processing and Applications*, New Jersey: Noyes Publications, 1993, pp. 11-39.
- [43] Mainwood, A., *Physical Review B (USA)*, vol. 49, (1994), pp. 7934-40.

- [44] Davies, C., Nazaré, M. H. and Hamer, M. F., *Proceeding of the Royal Society of London A (UK)*, vol.351 (1976) pp.245.
- [45] Nazaré, M. H. and Neves, A. J., eds: *Properties, Growth and Applications of Diamond*, Inspec: London, (2001), pp.21-141.
- [46] Clark, C. D., Dean, P. J. and Harris, P. V., *Proceedings of the Royal Society of London Series A* 277 (1964) 312.
- [47] Collins, A. T., *Journal of Physics C*, 20, (1987) 2027.
- [48] Clark, C. D., Ditchburn, R. W. and Dyer, H. B., *Proceedings of the Royal Society of London A*, 235 (1956) 305.
- [49] Clark, C. D., Ditchburn, R. W. and Dyer, H. B., *Proceedings of the Royal Society of London A*, 237 (1956) 75.
- [50] Farrer, R. G. and Vermeulen, L. A., *Journal of Physics C*, 5 (1972) 2762.
- [51] Dyer, H. B. and du Preez, L., *Journal of Chemical Physics*, 42 (1965) 1898.
- [52] Farrer, R. G., *Solid State Communications*, 7, (1969) 685.
- [53] Clark, C. D. and Palmer, D. W., *Proceedings of the 4th Symposium on Reactivity of Solids*, Elsevier: Amsterdam, 1960, pp. 435.
- [54] Palmer, D. W., PhD Thesis, Reading University, 1962.
- [55] Clark, C. D. and Palmer, D. W., Diamond Conference, 1964, unpublished.
- [56] Davies, G., *Journal of Physics C*, 5 (1972) 2534; Clark, C. D. and Davey, S. T., *ibid*, 17 L399, (1984).
- [57] Jones, R., Goss, J. P., Briddon, P. R. and Öberg, S., *Physical Review B*, vol.56 (1997) 4.
- [58] O'Brief, J. L., Furusawa, A. and Vuckovic, J., *Nature Photonics*, (2009), 3687-95.

- [59] Neumann, P., Beck, J., Steiner, M., Rempp, F., Fedder, H., Hemmer, P., R., Wrachtrup, J. and Jelezko, F., *Science*, 329 (2010), pp. 542-4.
- [60] Jelezko, F., Gaebel, T., Popa, I., Gruber, A. and Wrachtrup, J., *Physical Review Letters*, 92, 7 (2004).
- [61] Reddy, N. B. S., Manson, N. B. and Krausz, E. R., *Journal of Luminescence*, 38, 46, (1987)
- [62] Harrison, J., Sellers, M. J. and Manson, N. B., *Journal of Luminescence*, 107 (2004), 245.
- [63] Loubser, J. H. N. and van Wyk, J. A., *Reports on Progress in Physics*, 41 (1978), 1201.
- [64] Jelezko, F., Popa, I., Gruber, A., Tietz, C., Wrachtrup, J., Nizovtsev, A. and Kilin, S., *Applied Physics Letters*, 81 (2002) 2160.
- [65] Buckley, B. B., Fuchs, G. D., Bassett, L. C. and Awschalom, D. D., *Science*, 330, 1212 (2010)
- [66] Hanson, R., Dobrovitski, V. V., Feiguin, A. E., Gywat, O. and Awschalom, D. D., *Science*, 320, 352 (2008)
- [67] Celii, F. G., Butler, J. E., *Annual Review of Physical Chemistry*, 42 (1991), pp. 643-684.
- [68] Sellschop, J. F. P., ed: Field, J. E., *Properties of Natural and Synthetic Diamond*, Academic Press. London, (1992), pp. 81-179.
- [69] Connel, S. H., Sellschop, J. P. F., Butler, J. E., Maclear, R. D., Doyle, B. P. and Machi, I. Z., *Diamond and Related Materials*, 7, (1998), pp. 1714-1718.
- [70] McNamara, K. M., in *Hydrogen in Semiconductors II*, ed: Nickel, N. H., *Semiconductors and Semimetals*, vol. 61, Academic Press, San Diego, (1999), pp. 283-310.

- [71] Collins, A. T., *Ceramics International*, 22, 321 (1996).
- [72] Machi, I. Z., *PhD Thesis*, University of the Witwatersrand, Johannesburg, pp. 5-13.
- [73] Lichti, R. L. in *Hydrogen in semiconductors II*, ed. Nickel, N. H., *Semiconductors and Semimetals*, Vol. 61, Academic Press, San Diego, (1999), pp. 311-372.
- [74] Claxton, T. A., Evans, A. and Symons, M. C. R., *Journal of the Chemical Society, Faraday Transactions*, 2, 82(11), (1986), pp. 2031-2037.
- [75] Estle, T. L., Estreicher, S. and Marynick, D. S., *Physical Review Letters*, 58(15), (1987), pp. 1547-1550.
- [76] Briddon, P. R., Jones, R. and Lister, G. M. S., *Journal of Physics C*, 21, (1988), pp. L1027-L1031.
- [77] Saada, D. J., Adler, J. and Kalish, R., *Physical Review B*, 61(16), (2000), pp. 10711-10715.
- [78] Holzschuh, E., Kündig, W., Meier, P. F., Patterson, B. D., Sellschop, J. P. F., Stemmet, M. C. and Appel, H., *Physical Review A*, 25(3), (1982), pp. 1272-1286.
- [79] Goss, J. P., Jones, R., Heggie, M. I., Ewels, C. P., Briddon, P. R. and Öberg, S., *Physical Review B*, 65, (2002), pp. 115207-1 - 115207-13.
- [80] Mehandru, S. P., Anderson, A. B. and Angus, J. C., *Journal of Materials Research*, 7 (1992), 689.
- [81] Mainwood, A. and Stoneham, A. M., *Journal of Physics C*, 17 (1984), 2513.
- [82] Connel, S. H., Sideras-Haddad, E., Smallman, C. G., Sellschop, J. P. F., Machi, I. Z. and Bharuth-Ram, K., *Nuclear Instruments and Methods in Physics Research B*, 118 (1996), 332.

- [83] Machi, I. Z., Schaaff, P., Connel, S. H., Doyle, B. P., Maclear, R. D., Formenti, P., Bharuth-Ram, K. and Sellschop, J. F. P., *Nuclear Instruments and Methods in Physics Research B*, 127/128 (1997), 212.
- [84] Smallman, C. G., Connel, S. H., Madiba, C. C. P. and Sellschop, J. P. F., *Nuclear Instruments and Methods in Physics Research B*, 118 (1996), 688.
- [85] Madhuku, M., *PhD Thesis*, University of the Witwatersrand, Johannesburg, (2007), pp. 22-27.
- [86] Liang, Z. N., Haas, C. and Niesen, L., *Physical Review Letters*, 72 (1994), 12, pp.1846-1849.
- [87] Miyakazi, T., Okushi, H. and Uda, T., *Physical Review Letters*, 88 (2002) 6.
- [88] Goss, J. P., *Journal of Physics. Condensed Matter*, 15 (2003), pp.R551-R580.
- [89] Mehandru, S. P. and Anderson, A. B., *Journal of Materials Research*, 9 (1994), pp. 383-395.
- [90] Nishimatsu, T., Katayama-Yoshida, H. and Orita, N., *Japan Journal of Applied Physics*, 41 (2002), pp. 1952-1962.
- [91] Nishimatsu, T., Katayama-Yoshida, H. and Orita, N., *Physica B*, 302-303, (2001), pp. 149-154.
- [92] Anderson, A. B. and Mehandru, S. P., *Physical Review B*, 48 (1993), pp. 4423-4427.
- [93] Kajihara, S. A. and Bernholc, J., *Physical Review Letters*, 66 (1991), pp. 2010-2013.
- [94] Schauer, S. N., Flemish, J. R., Wittstruck, R., Landstrass, M. I. and Plano, M. A., *Applied Physics Letters*, 64 (1994), 1094.

- [95] Koizumi, S., Teraji, T. and Kanda, H., *Diamond and Related Materials*, 9 (2000), 935.
- [96] Yamanaka, S., Watanabe, H., Masai, S., Takeuchi, D., Okushi, H. and Kajimura, K., *Japanese Journal of Applied Physics*, 37, (1998), L1129-L1131.
- [97] Schenkel, T., Hamza, A. V., Barnes, A. V. and Schneider, D. H., *Progress in Surface Science*, Vol. 61 (1999), pp. 21-84.
- [98] Carlson, T. A., Nestor C. W., Wasserman, N. JR. and McDowell, J. D., *Atomic Data*, 2 (1970), pp. 63-99.
- [99] <http://www.dreebit.com/en/ion-beam-technology/scientific-service/ionisation-energies.html>; Cowan, R. D., *The Theory of Atomic Structure and Spectra*, University of California Press, Berkeley, (1981), p. 12.
- [100] Burgdörfer, J. and Meyer, F., *Physical Review A*, Vol 47, 1 (1993), p. R20
- [101] Burgdörfer, J., Lerner, P. and Meyer, F., *Physical Review A*, Vol. 44, (1991), p. 5674
- [102] Briand, J. P., de Billy, L., Charlers, P., Essabaa, S., Briand, P., Geller, R., Desclaux, J. P., Bliman, S. and Ristori, C., *Physical Reivew Letters*, Vol. 65, 2 (1990), pp. 159-162
- [103] Aumayr, F. and Winter, H., *Philosophical Transactions of the Royal Society of London A*, 362, 77, 2004
- [104] Winter, H. and Aumayr, F., *Journal of Physics B: Atomic, Molecular and Optical Physics*, 32 (1999), R39-R65.
- [105] Schippers, S., Hustedt, S., Heiland, W., Köhrbrück, R., Bleck-Neuhaus, J., Kemmler, J., Lecler, D. and Stolterfoht, N., *Nuclear Instruments and*

- Methods in Physics Research B*, 78 (1993), pp. 106-112.
- [106] Arnau, A., Zeiljmans van Emmichoven, P. A., Juaristi, J. I. and Zaremba, E., *Nuclear Instruments and Methods in Physics Research B*, 100 (1995), pp. 279-283.
- [107] Arnau, A., Aumayr, F., Echenique, P.M., Grether, M., Heiland, W., Limburg, J., Morgenstern, R., Roncin, P., Schippers, S., Schuch, R., Stolterfoht, N., Varga, P., Zouros, T.J.M. and Winter, H.P., *Surface Science Reports*, 27, (1997), pp. 113-239.
- [108] Aumayr, F., Winter, H. P., Limburg, J., Hoekstra, R. and Morgenstern, R., *Physical Review Letters*, 79 (1997), pp. 2590-600
- [109] Briand, J. P., Thuriez, S., Giardino, G., Borsoni, G., Froment, M., Ed-drief, M and Sebenne, C., *Physical Review Letters*, 79 (1997), pp. 2591-1
- [110] Sideras-Haddad, E., Schenkel, T., Rebuli, D. B., Persaud, A., Shrivastava, S., Schneider, D. H. and Mwakakunga, B., *Nuclear Instruments and Methods in Physics Research B*, 256 (2007), pp. 464-467.
- [111] Sideras-Haddad, E., Schenkel, T., Shrivastava, S., Makgato, T., Batra, A., Weis, C. D., Persaud, A., Erasmus, R. and Mwakakunga, B., *Nuclear Instruments and Methods in Physics Research B*, 267 (2009), pp. 2774-2777.
- [112] Parilis, E., A mechanism for sputtering of non-metals by slow multiply charged ions. In *Proceedings of the International Conference on Phenomena in Ionized Gases*, Bucharest: Editura Academia Republicii Socialiste Romania, (1969), pp. 324-327.
- [113] Bitenskii, I. S., Murakhmetov, M. N. and Parilis, E. S., *Soviet Physics, Technical Physics*, 24 (1979), pp. 618-621.

- [114] Bitenskiĭ, I. S. and Parilis, E. S., *Journal of Physics, Paris*, C2 (1989), pp. 227-230.
- [115] Cheng, H. P. and Gillaspay, J. D., *Physical Review B*, 55 (1997), pp. 2628-2636.
- [116] Wang, T. S., Yang, G. X., Liu, S. J., Xu, H., Han, Y. C., Xiang, Y., Chen, L. and Yang, X. Y., *Nuclear Methods and Instruments in Physics Research B*, 267 (2009), pp. 2605-2607.
- [117] Seitz, F., Köhler, J. S., *Solid State Physics*, 2 (1956) 305.
- [118] Kaganov, M. I., Lifshitz, I. M., Tanatarov, I. V., *Soviet Physics. JETP*, 4 (1957), pp. 173.
- [119] Toulemonde, M., Constantini, J., Dufour, C., Meftah, A., Paumier, E. and Studer, F., *Nuclear Instruments and Methods in Physics Research B*, 116 (1996), pp. 37.
- [120] El-Said, A.S., Meissl, W., Simon, M.C., Crespo López-Urrutia, J.R., Lemell, C., Burgdörfer, J., Gebeshuber, I.C., Winter, HP., Ullrich, J., Trautmann, C., Toulemonde, M. and Aumayr, F., *Nuclear Instruments and Methods in Physics Research B*, 258 (2007), pp. 167-171.
- [121] Daraszewics, S. L. and Duffy, D. M., *Nuclear Instruments and Methods in Physics Research B*, 269 (2011), pp. 1646-1649.
- [122] Szenes, G., *Material Science Forum*, 97-99 (1992), 647.
- [123] Szenes, G., *Physical Review B*, Vol. 51, 13, 1995.
- [124] Karlušić, M. and Jakšić, *Nuclear Instruments and Methods in Physics Research B*, 280 (2011), pp. 103-110.
- [125] Neidhart, T., Pichler, F., Aumayr, F., Winter, H. P., Schmid, M. and Varga, P., *Nuclear Instruments and Methods in Physics Research B*, 98 (1995), pp. 465-468

- [126] Sporn, M., Libiseller, G., Neidhart, T., Schmid, M., Aumayr, F., Winter, H. P., Varga, P., Grether, M. and Stolterfoht, N., *Physical Review Letters*, 79 (1997), pp. 945-948.
- [127] Aumayr, F., Burgdörfer, J., Varga, P. and Winter, H. P., *Communications of Atomic and Molecular Physics*, 34 (1999), pp. 201-209.
- [128] Hayderer, G., Schmid, M., Varga, P., Winter, H., Aumayr, F., Wirtz, L., Lemell, C., Burgdörfer, J., Hägg, L. and Reinhold, C. O., *Physical Review Letters*, 83, 1999, pp. 3948-3951.
- [129] Heller, R., Facsko, S., Wilhelm, R. A. and Möller, W., *Physical Review Letters*, 101, 096102, 2008.
- [130] Mochiji, K., Itabashi, N., Yamamoto, S., Schimizu, S., Ohtani, S., Kato, Y., Tanuma, H., Okuno, K. and Kobayashi, N., *Surface Science*, 358 (1996), pp. 673-677.
- [131] Parilis, E., Coulomb Explosion by Highly Charged Ions, in *Trapping Highly Charged Ions: Fundamentals and Applications*, Ed. Gillaspay, J., Nova Science Publishers, New York, 2001, pp. 411-436
- [132] Arifov, U. A., Kishinevsky, L. M., Mukhamadiev, E. S. and Parilis, E. S., *Journal of Technical Physics*, 43, 181, (1973).
- [133] Dufour, Ch., Audouard, A., Beneu, F., Dural, J., Girard, P., Hairie, A., Levalois, M., Paumier, E. and Toulemonde, M., *Journal of Physics: Condensed Matter*, 5 (1993), 4573.
- [134] Wang, Z. G., Dufour, Paumier, E., Toulemonde, M. *Journal of Physics: Condensed Matter*, 6 (1994) 6733.
- [135] Toulemonde, M., Dufour, Ch., Meftah, A. and Paumier, E., *Nuclear Instruments and Methods in Physics Research B*, 166-167 (2000) 903.

- [136] Toulemonde, M., Dufour, Ch., Wang, Z. G., Paumier, E., *Nuclear Instruments and Methods in Physics Research B*, 112 (1996) 26
- [137] Dufour, Ch., Beuneu, F., Paumier, E. and Toulemonde, M., *Europhysics Letters*, 45 (1999) 585.
- [138] Toulemonde, M., Dufour, Ch., Meftah, A. and Paumier, E., *Nuclear Instruments and Methods in Physics Research B*, 166-167 (2000) pp. 903-912.
- [139] Katz, R. and Kobetich, E. J. *Physical Review*, 170, 397, 1968; *Physical Review*, 186, 344, 1969.
- [140] Gervais, B., *Thèse Université de Caen*, 1993
- [141] Waligorski, M. P. R., Hamm, R. N. and Katz, R., *Nuclear Tracks and Radiation Measurements*, 11, 309, 1986.
- [142] van Driel, H. M., *Physical Review B*, 35 (1987) 8166
- [143] Mao, S., Mao, X., Greif, R., Russo, R. *Applied Surface Science*, 127 (1998), 206.
- [144] Szenes, G., *Physical Review B*, 60 (1999) 3140.
- [145] Szenes, G., *Physical Review B*, 61 (2000) 14267.
- [146] Szenes, G., Horváth, Z. E., Pécz, B., Pászti, F., Tóth, L., *Physical Review B*, 65 (2002) 045206
- [147] Szenes, G., *Journal of Nuclear Materials*, 336 (2005) 81.
- [148] Szenes, G., *Nuclear Instruments and Methods in Physics Research B*, 269 (2011) 174.
- [149] Ronchi, C., *Journal of Applied Physics*, 44 (1973) 3575
- [150] Neidhart, T., Pichler, F., Aumayr, F., Winter, H. P., Schmid, M. and Varga, P., *Physical Review Letters*, 74 (1995) pp. 5280-5283.

- [151] Green, T. A., Loubriel, G. M., Richards, P. M., Tolk, N. H. and Haglund, R. F., *Physical Review B*, 35 (1987) pp. 781-787.
- [152] Seifert, N., Liu, D., Barnes, A., Albridge, R., Yan, Q., Tolk, N., Husinsky, W. and Betz, G., *Physical Review B*, 47 (1993) 7653.
- [153] Szymonski, M., *Vidensk. Selsk.*, 43 (1993), pp. 495-526.
- [154] Puchin, V., Shluger, A., Nakai, Y. and Itoh, N., *Physical Review B*, 49 (1994) 11364.
- [155] Timm, C., *Theory of Magnetism*, Technische Universität Dresden, Institute for Theoretical Physics, International Max Planck Research School for Dynamical Processes in Atoms, Molecules and Solids, 2015.
- [156] Nolting, W. and Ramakanth, A., *Quantum Theory of Magnetism*, Springer-Verlag: Berlin Heidelberg, (2009), pp. 175-232.
- [157] Getzlaff, M., *Fundamentals of Magnetism*, Springer-Verlag, Berlin Heidelberg, (2008), pp. 3-43.
- [158] Kittel, C., *Introduction to Solid State Physics*, Seventh Edition, John Wiley and Sons Inc., Singapore, (2006), pp. 415-441.
- [159] Turek, P., Nozawa, K., Shiomi, D., Awaga, K., Inabe, T., Maruyama, Y. and Kinoshita, M., *Chemical Physics Letters*, 180 (1991) 327.
- [160] Tamura, M., Nakazawa, Y., Shiomi, D., Nozawa, K., Hosokoshi, Y., Ishikawa, M., Takahashi, M., Kinoshita, M., *Chemical Physics Letters*, 186 (1991) 401
- [161] Makarova, T., Sundqvist, B., Höhne, R., Esquinazi, P., Kopelevich, Y., Scharff, P., Davydov, V. A., Kashevarova, L. S., Rakhmanina, A. V. *Nature (London)* 413 (2001) 716
- [162] Wood, R. A., Lewis, M. H., Lees, M. R., Bennington, S. M., Cain, M. G. and Kitamura, N. *Journal of Physics: Condensed Matter* 14 (2002) L385

- [163] Perdew, J. P., Burke, K. and Wang, Y., *Physical Review B*, 54, 16533 (1996).
- [164] Ma, Y., Lehtinen, P. O., Foster, A. S. and Nieminen, R. M., *New Journal of Physics*, 6, 68 (2004).
- [165] Lehtinen, P. O., Foster, A. S., Ayuela, A., Krasheninikov, A., Nordlund, K. and Nieminen, R. M., *Physical Review Letter*, 91, 017202 (2003).
- [166] Thrower, P. A. and Mayer, R. M., *Phys. Status Solidi (a)*, 47, 11 (1978).
- [167] Esquinazi, P., Höhne, R., Han, K-H., Setzer, A., Spemann, D. and Butz, T., *Carbon* 42 (2004), pp. 1213-1218.
- [168] Yang, X., Xia, H., Qin, X., Li, W., Dai, Y., Liu, X., Zhao, M., Xia, Y., Yan, S. and Wang, B., *Carbon*, 47, 1399 (2009).
- [169] Pisani, L., Montanari, B. and Harrison, N. M., *New Journal of Physics*, 10 (2008) 033002
- [170] Duplock, E. J., Scheffler, M. and Lindan, P. J. D., *Physical Review Letters*, 92, 22 (2004).
- [171] Dubman, M., Shiroka, T., Luetkens, H., Rothermel, M., Litterst, F. J., Morenzoni, E., Suter, A., Spemann, D., Esquinazi, P., Setzer, A. and Butz, T., *Journal of Magnetism and Magnetic Materials*, 322 (2010), pp. 1228-1231.
- [172] Lee, H., Son, Y.-W., Park, N., Han, S. and Yu, J., *Physical Review B*, 72 (2005), 174431.
- [173] Venkatesan, M., Dunne, P., Chen, Y., Zhang, H. Z. and Coey, J. M. D., *Carbon*, 56 (2013), pp. 279-287.
- [174] Hong, J., Bekyarova, E., de Heer, W. A., Haddon, R. C. and Khizroev, S., *ACS Nano*, 10.1021/nn403939r (2013).

- [175] Tarvainen, O., *Studies of Electron Cyclotron Resonance Ion Source Plasma Physics*, Department of Physics University of Jyväskylä, (2005), pp. 7-10.
- [176] Schmidt, B., Wetzig, K., *Ion Beams in Materials Processing and Analysis*, Springer Science and Business Media, (2012), pp. 44-63.
- [177] Child, C.D., *Phys. Rev.*, 32, (1911), 492-511.
- [178] Langmuir, I., *Phys. Rev.*, 2, (1913), 450-486.
- [179] Greinacher, H., *Phys.*, 4, (1921), 195.
- [180] www.nobelprize.org
- [181] Van der Graaff, R. J., Compton, K. T., Van Atta, L. C., *Phys. Rev.*, 43 (3), 1933,149-157.
- [182] Hinterberger, F., *Electrostatic Accelerators*, Helmholtz-Institute für Strahlen-und Kernphysik, University of Bonn Germany, DOI: 10.5170/CERN-2006-012.95, 2006.
- [183] International Atomic Energy Agency, *Instrumentation for PIXE and RBS*, IAEA-TECDOC-1190, Vienna, Austria, 2000,149-157.
- [184] Rubin, S., Passel, T. O. and Bailey, E., *Analytical. Chem.*, 29, (1957), 736.
- [185] Mayer, M., Workshop on Nuclear Data for Science and Technology: Materials Analysis, *Rutherford Backscattering Spectrometry*, Max-Planck-Institut für Plasmaphysik, EUROATOM Association, Carching, Germany (2003).
- [186] Kebe, Th. and Carl, A. *Journal of Applied Physics*, 95(2004)3.

- [187] Ménlin, T., Zdrojek, M. and Brunel, D., *Scanning Probe Microscopy in Nanoscience and Nanotechnology*, Springer-Verlag, Berlin Heidelberg (2010), pp. 89-128.
- [188] Long, D. A., *The Raman effect: A Unified Treatment of the Theory of Raman Scattering by Molecules*, John Wiley & Sons Ltd, (2002), ISBNs: 0-470-8457607.
- [189] Mohammed, A., *Theoretical Studies of Raman Scattering*, Department of Theoretical Chemistry, School of Biotechnology, Royal Institute of Technology, Stockholm, (2011).
- [190] Collins, A. T., *Diamond and Related Materials, I*, (1992), 457-469.
- [191] Gilchrist, J., *Spectroscopy The Tools of the Trade, Photonics Design and Applications Handbook*, (2000) pp H-81;
- [192] Josephson, B. D., *Physics Letters*, 1, (1962), pp. 252-253.
- [193] Feynman, R. P., Leighton, R. B., Sands, M., *The Feynman Lectures on Physics* (Addison-Wesley, Reading MA, 1965).
- [194] Van Duzer, T., Turner, C. W., *Principles of Superconductive Devices and Circuits*, 2nd Ed,(Prentice Hall PTR, Upper Saddle River NJ, 1999).
- [195] Kleiner, R., Koelle, D., Ludwig, F., Clarke, J., *Proceedings of the IEEE*, 92 (2004)10.
- [196] Wikswo, J. P., *Applications of Superconductivity*, 365, (2000), pp. 139-228.
- [197] Nation, P. D., Blencowe, M. P., Rimberg, A. J., Buks, E., *Physical Review Letters*, 103, (2009), 087004.
- [198] Wilson, C. M., Johansson, G., Pourkabirian, A., Simoen, M., Johansson, J. R., Duty, T., Nori, F., Delsing, P., *Nature*, 479 (2011) 376.

- [199] Veldhorst, M., Molenaar, C. G., Wang, X. L., Hilgenkamp, H., Brinkman, A., *Applied Physics Letters*, 100 (2012) 072602.
- [200] Weinstock, H., and Ralston, R. W., Eds., *The New Superconducting Electronics*, NATO ASI series, Dordrecht, The Netherlands: Kluwer, 1993.
- [201] Weinstock, H., Ed., *SQUID Sensors: Fundamentals, Fabrication and Applications*, Dordrecht, The Netherlands: Kluwer, 1996.
- [202] Clarke, J. and Braginski, A. I., Eds., *SQUID Handbook*, Wiley-VCH, Berlin, Germany, 2004.
- [203] Makgato, T., Sideras-Haddad, E., Shrivastava, S., Schenkel, T., Ritter, R., Kowarik, G., Aumayr, F., Crespo López-Urrutia, J.R., Bernitt, S., Beilmann, C., Ginzler, R., *Nuclear Instruments and Methods in Physics Research Section B*, 314 (2013), pp.135 - 139.
- [204] Makgato, T.N., Sideras-Haddad, E., Ramos, M.A., García-Hernández, M., Climent-Font, A., Zucchiatti, A., Muñoz-Martin, A., Shrivastava, S., Erasmus, R., *Journal of Magnetism and Magnetic Materials*, 413 (2016), pp. 76-80.
- [205] Daya, N., Sideras-Haddad, E., Makgato, T.N., García-Hernández, M., Climent-Font, A., Zucchiatti, A., Ramos, M.A., *Diamond and Related Materials*, 64 (2016), pp. 197-201.
- [206] González Martínez, A. J., Crespo López-Urrutia, J. R., Fischer, D., Soria Orts, R., and Ullrich, J., *Journal of Physics: Conference Series* 72 (2007) 012001.
- [207] Crespo López-Urrutia, J. R., Bapat, B., Draganić, I., Feuerstein, B., Fischer, D., L'orch, H., Moshhammer, R., Ullrich, J., Dubois, R. D., and Zou, R. D., *Hyperfine Interactions*, 146/147 (2003) 109-113.

- [208] Lehérissier, P., Barué, C., Canet, C., Dubois, M., Dupuis, M., Flambard, J. L., Gaubert, G., Jardin, P., Lecesne, N., Lemagnen, F., Leroy, R., Pacquet, J. Y., and Pellemoine-Landré, F., *Review of Scientific Instruments*, Vol 75, 5, (2004)
- [209] Johnson, R. E. and Sundqvist, Bo U. R. *Physics Today*, March 1992.
- [210] Yamamura, Y., Nakagawa, S.T. and Tawara, H. *Nuclear Instruments and Methods in Physics Research B*, 98 (1995), pp. 400-406.
- [211] Ziegler, J. F., *The Stopping and Range of Ions in Matter*, Pergamon Press, New York, 1977.
- [212] Schenkel, T., Barnes, A. V., Hamza, A. V., Schneider, D. H., Banks, J. C. and Doyle, B. L. *Physical Review Letters*, 80 (1998)19.
- [213] El-Said, A. S., Meissl, W., Simon, M. C., Crespo López-Urrutia, J. R., Lemell, C., Burgd'orfer, J., Gebeshuber, I. C., Winter, H. P., Ullrich, J., Trautmann, C., Toulemonde, M. and Aumayr, F. *Nuclear Instruments and Methods in Physics Research B*, 258 (2007), pp.167-171.
- [214] Kim, J. C., Cahill, D. G., and Averback, R. S. *Surface Science*, 574 (2005), pp. 175-180.
- [215] Gnaser, H. *Pure and Applied Chemistry*, Vol 83, No. 11, (2011) 2003-2025.
- [216] Nordlund, K., Keinonen, J. and Mattila, T. *Physical Review Letters*, 77 (2004) 4.
- [217] Barzola-Quiquia, J., Esquinazi, P., Rothermel, M., Spemann, D., Setzer, A. and Butt, T. *Nuclear Instruments and Methods in Physics Research B*, 256 (2007) pp. 412-418.
- [218] Koike, J. D., Parkin, M. and Mitchell, T. E. *Applied Physics Letters* 60 (1992) 12.

- [219] Gruen, D. M., Shenderova, O. A., Alexander, Ya, V., *Synthesis, Properties and Applications of Ultrananocrystalline Diamond*, NATO Science Series, 2005, p.142.
- [220] Heremans, J., Olk, C. H. and Morelli, D. T., *Physical Review B*, 49 (1994) 15122.
- [221] Kittel, C., *Introduction to Solid State Physics*, 7th Edition, John Wiley & Sons, New York,(2006), p. 416-422.
- [222] Gacic, M., Jakob, G., Herbort, C. and Adrian, H., *Physical Review B*, 75 (2007), 205206.
- [223] Naydenov, B., Kolesov, R., Batalov, A., Meijer, J., Pezzagna, S., Rogalla, D., Jelezko, F. and Wrachtrup, J., *Applied Physics Letters*, 95 (2009) 181109.
- [224] Pezzagna, S., Rogalla, D., Wildanger, D., Meijer, J. and Zaitsev, D., *New Journal of Physics*, 13 (2011) 035024.
- [225] Davies, G., Lawson, S. C., Collins, A. T., Mainwood, A. and Sharp, S. J., *Physical Review B*, vol. 46, 20, 1992.
- [226] Collins, A. T., *New Diamond and Frontier Carbon Technology*, 17 (2007) 2.
- [227] Buchal, Ch., *Nuclear Instruments and Methods in Physics Research B*, 96 (1995), pp. 370-373.
- [228] Praver, S., Orwa, J. O., Nugent, K. W. and Jamieson, D. N., *Physical Review B* 62 (2000) 9.
- [229] Israelachvili, J., *Intermolecular Surface Force*, Academic Press, (1992).
- [230] Babcock, K. L., Elings, V. B., Shi, J., Awschalom, D. D. and Dugas, M., *Applied Physics Letters*, 69 (1996) pp.705-707.

- [231] Zhu, X., *Magnetic Force Microscopy Studies on Submicron and Nanoscale Magnet Arrays*, Centre for the Physics of Materials, Department of Physics, McGill University, 2002.
- [232] Cherniavskaya, O., Chen, L. W., Weng, V., Yuditsky, L. and Brus, L. E., *Journal Physical Chemistry B* 107 (2003) 1525.